Pharmaceutical Thin Film Formulations with Controlled Crystal Polymorphism, Morphology, and Size

---

A Dissertation

Presented to

The faculty of the School of Engineering and Applied Science

University of Virginia

In partial fulfillment
of the requirements for the degree

Doctor of Philosophy

by

Stephanie Guthrie

December 2020

APPROVAL SHEET

This

Dissertation

Is submitted in partial fulfillment of the requirements

for the degree of

Doctor of Philosophy

Author: Stephanie M. Guthrie

This Dissertation has been read and approved by the examining committee:

Advisor:	Gaurav Giri
Committee Member:	Joshua Choi
Committee Member:	Jerrold Floro
Committee Member:	David Green
Committee Member:	Rachel Letteri

Accepted for the School of Engineering and Applied Science:

Craig H. Benson, School of Engineering and Applied Science

December 2020

Abstract

Crystallization and formulation are critical steps for the creation of new therapeutics. Most drug products are formulated as solid tablets and capsules containing thousands of solid drug crystals. However, an increasing number of candidate drug molecules are not suitable for development in traditional tablet formulations due to poor physicochemical properties (e.g. solubility, dissolution rate, melting point) associated with the crystal forms. Solid form screening is performed to characterize crystal attributes (including polymorph, size and shape) and select the desired form for further development. Screening is one of many processes that contribute to long lead times and the significant development costs in the pharmaceutical industry. This motivates the development of new screening technologies that can improve understanding of pharmaceutical solid states. This dissertation discusses the development of a meniscus guided coating technology for the application of solid form screening and selection in pharmaceutical molecules. New formulation approaches are presented, including thin films, novel drug carriers and 3D printed drug loaded gel tablets.

In Chapter 2, crystalline thin films of glycine and acetaminophen were fabricated using evaporative meniscus guided coating. Films were characterized using polarized optical microscopy and X-ray diffraction to determine morphology and crystal structure. Simple process parameters, such as coating temperature and coating speed are shown to select different crystal morphologies and polymorphs while controlling film thickness. In Chapter 3, In situ grazing incidence X-ray diffraction was used to characterize glycine crystallization during the coating process. Through gaining spatial and temporal resolution of crystallization, I develop and propose a hypothesis for the crystallization of multiple crystal orientations during the coating process. In Chapter 4, a novel meniscus guided coating regime is accessed by utilizing substrate temperatures that exceed the boiling point of the solvent during flow coating. This is shown to

isolate microcrystals, a highly desirable crystal size and shape for the pharmaceutical industry. Chapters 2-4 present a new technique for pharmaceutical solid form screening and selection.

Formulation typically encompasses incorporation of the active pharmaceutical compound with coatings and additives (e.g. polymer binders and excipients) to control drug release. Traditionally, a solid tablet is the preferred formulation. However, alternative strategies are being explored to control drug release timescales, and create customized doses for personalized healthcare. We explore metal organic frameworks (MOFs) as potential drug carriers in Chapter 5 and 3D printing for personalized dosing in Chapter 6.

MOFs are a porous material with demonstrated utility for storage of small molecules and proteins, thus motivating their use as drug carriers. The mechanism of transport within a MOF is complex and poorly understood, a critical property that must be characterized if MOFs are to be used for drug delivery. Chapter 5 of this dissertation presents a nanofluidic platform for crystallization of high-quality MOF crystals and subsequent loading with fluorescent small molecules. The device can be used to characterize diffusion of small molecules in the framework by tracking the fluorescence intensity.

Additive manufacturing, such as 3D printing, has great potential to create custom drug formulations. In chapter 6, we develop a polymer/drug gel that can be extruded from a syringe to create 3D printed tablets. Tablet size was changed by printing multiple layers sequentially. Crystal structure and bonding in the polymer matrix were characterized using X-ray diffraction and infrared spectroscopy. Tablet dissolution was assessed using ultraviolet-visible spectroscopy. This dissertation presents strides towards improving pharmaceutical development technologies, from solid form screening and selection to formulation design.

Acknowledgements

This dissertation represents much more than an independent scientific contribution to chemical engineering. It also represents the multiple support structures that have empowered this achievement.

First, to my advisor, Professor Gaurav (Gino) Giri. Thank you for pursuing a new research direction in pharmaceuticals with me. You have shown me unwavering confidence and positivity, even when we encountered numerous challenges. This taught me to have flexibility and adaptability and to realign expectations of myself and others. Thank you for the opportunities to grow as a scientist, engineer, and thoughtful human.

Thank you to my committee members, Professor Josh Choi, Professor Jerry Floro, Professor David Green, Professor Rachel Letteri, for your contributions to my development. Each of you has had an impact on my scientific growth, and I am grateful that I was able to learn from you and your different perspectives

Thank you to collaborators on several different projects. Beamline scientist Detlef Smilgies for collaborating on synchrotron projects and maintaining the D-1 beamline. Professor Nathan Swami, Armita Salahi, Dr. Walter Varhue for help with developing nanofluidic devices. Professor Baoxing Xu, Dr. Yuan Gau for collaborating on computational work.

A special thanks to Professor George Prpich for guiding me in pedagogy and showing me how to mentor students with diverse needs.

The Giri Lab has grown and changed, but each person has had an impact on my scientific development: Dr. Arian Ghorbanpour, Luke Huelsenbeck, Ashley Conley, Steve Jung, Natalie Smith, Prince Verma and undergraduate researchers Lizzy Tonneslan, Priya Shankar, Lauren Hornsby, Jeongwon (John) Choi, Craig Doody, Clayton Burruss, Hamsini Muralikrishnan. Each of you brought a unique perspective and personality that made our lab a very special home. The lab could not run without our teamwork.

Also thank you to Choi lab members Dr. Ben Foley, Dr. Alex Chen, Dr. Xiaoyu Deng for sharing synchrotron time, discussing data analysis, and being my second lab home when the Giri lab was young and small.

Beyond my academic support, my friends have been a source of sanity during the most challenging times. Natalie, Madison, Nate, Melissa, Jenna, Tracy, Natalia, Evan, James T., Nick. Special thanks to Erica for bringing me coffee and always lending a listening ear.

I want to thank my family members, who have shaped me into the person I am today. My parents, Warren and Laurie, have taught me to always question the world around me and encouraged me to seek answers. My siblings, Matthew, Melissa, Wesley, Casey and Tessa have brought so much joy to my life – there is never a dull moment when we are together.

James Kammert, thank you for your support and patience as I have navigated uncertainty throughout this journey. Your kindness has meant the world to me. Most of all, you have helped me to create new goals for a bright future.

Table of Contents

List of Figures

List of Tables

Chapter 1. Introduction

The development of pharmaceutical drugs is a multi-billion dollar industry; a 2020 study estimates that the average cost of developing a new drug is 1.3 billion dollars.[1] During drug discovery and early development, several years are required to assess thousands of candidate drug molecules for potential to be a new therapeutic (**Figure 1.1,** from ©2013 Dunne et al.;

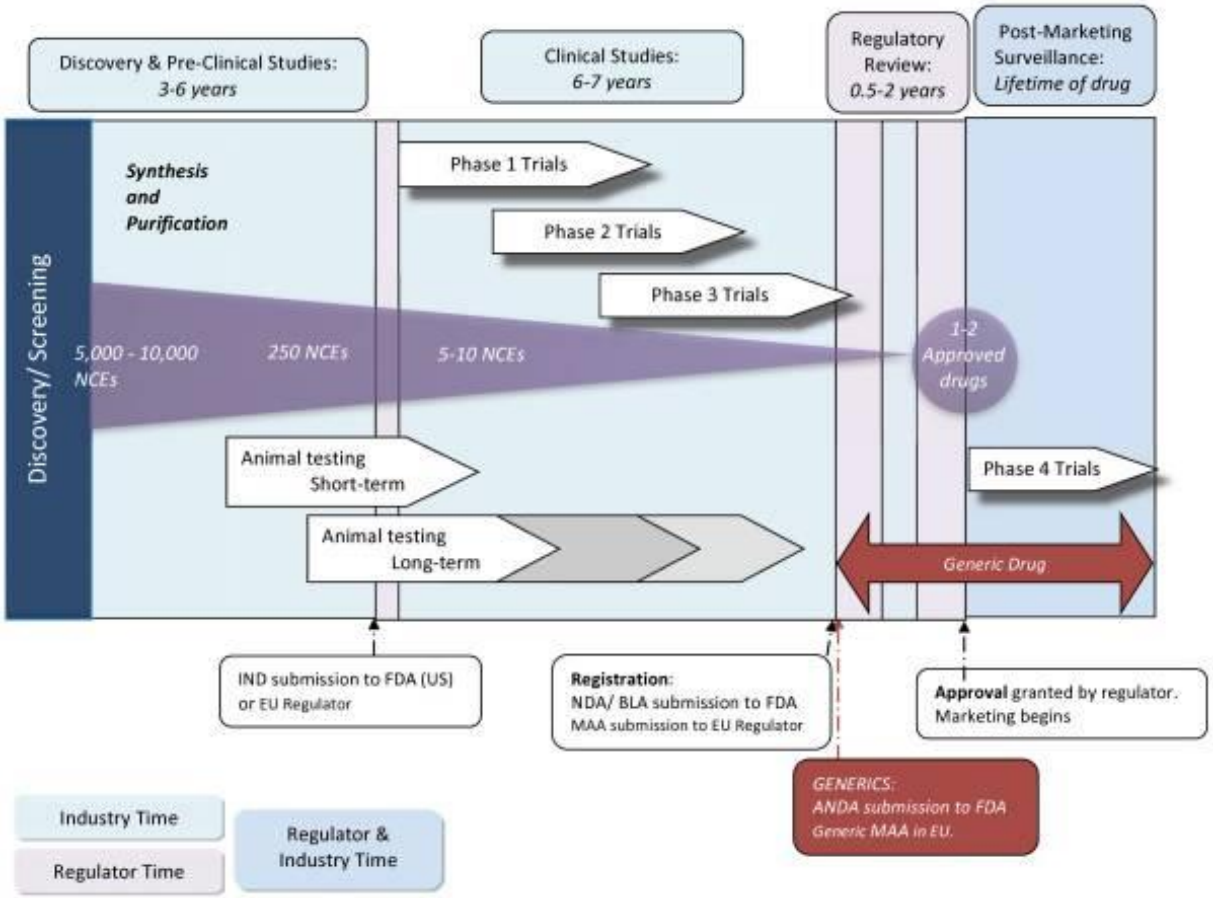

Figure 1.1 During drug development, thousands of candidate drug molecules are screened to identify molecules with the correct biological response and desired physicochemical properties, such as solubility and stability. Crystallization is a critical component of the discovery/screening process to purify new molecules and identify solid forms with desirable physicochemical properties. (Figure from ©2013 Dunne et al.; licensee BioMed Central Ltd.).

licensee BioMed Central Ltd[2]). Each drug candidate or active pharmaceutical ingredient (API) is critically examined through screening processes, guided by regulatory agencies such as the United States Food and Drug Administration (FDA).[3,4] In addition to assessing biological efficacy

of drug candidates, the physicochemical properties are assessed. Physicochemical properties are directly related to the solid form of a substance, and can affect the suitability of a drug for further development.[5] Therefore, screening for different crystal forms (polymorphs) of each substance is carried out to identify the desired form for development, with the optimized stability, solubility and rate of dissolution. Crystallization is also incorporated in drug development and drug discovery to achieve purification and solid form selection.[6]

Crystallization is used to purify products following synthesis of new candidate drug molecules.[7] Crystallization achieves this through selectively isolating the desired product in a solid form while impurities and side products remain in solution. The purified crystal product can be separated from the dissolved impurities using filtration.

Physicochemical properties, such as melting point and solubility, are closely related to the crystal structure of a material, and can impact the ability to manufacture a stable drug product.[5,8] More than 80% of drugs are prepared as solid oral doses such as tablets and capsules.[9] Solid drug forms are easy to handle, store, and use correctly, and are therefore the most desirable formulation. In a tablet, solid drug crystals must dissolve in the body before becoming bioavailable. With solid phases being ubiquitous in final drug formulations, significant resources are dedicated to characterizing and controlling solid-states, to ensure quality of drug product.[10] Briefly, the following are important steps during pharmaceutical development:

1. Characterization of pharmaceutical solid states (amorphous forms and polymorphs)[11]
2. Production of crystals with desired properties (like size and shape)[12]
3. Designing a formulation strategy[5]
4. Scaling up the manufacturing process[13]

Creating an effective drug product, such as a tablet, requires the ability to crystallize the desired solid forms and stabilize them prior to delivery. Failure to do so can lead to variability in drug performance.

The importance of thorough solid-state characterization is emphasized by examining a case where solid-state transformation occurred in a marketed drug. Ritonavir is a pharmaceutical compound used for treatment of HIV/AIDS.[14] It was introduced to the market in 1996, but was removed in 1998, due to an issue in the drug's formulation which drastically reduced the pharmaceutical's performance.[15] A solid form screen was performed, revealing that the drug was able to crystallize in two different solid forms (now identified as polymorphs, Form I and Form II), which have drastically different solubilities, and thus different bioavailability.[14,16] In this example, the selected crystal form for development was not the most stable crystal structure, resulting in phase change and inadequate performance. Careful material characterization and development of stable formulations are necessary to produce reliable pharmaceutical products.

An effective purification via crystallization is important to ensure that impurities are not included in the final drug product. Impurities can be detrimental to the safety of a drug, as demonstrated for a drug, ranitidine. In 2019, the antacid was recalled when a carcinogen was detected in distributed products.[17] High purity can be achieved using crystallization. While most impurities are rejected from a crystal, some impurity can be incorporated with the crystal via several mechanisms including agglomeration, surface deposition, surface absorption, co-crystallization etc.[6] Therefore sequential purification processes can improve the quality of the purification.

These examples demonstrate how crystallization serves multiple purposes in pharmaceutical development. Crystallization is important for purification of drug substances, to ensure a pure and safe product is provided to the consumer. Formulating a drug product requires selecting the crystal form that provides optimal stability and solubility of the drug.

1.1 Crystallization and formulation

1.1.1 Polymorphism in pharmaceuticals

Solids have the ability to take on multiple crystal structures, known as polymorphs (**Figure 1.2**). Polymorphs are created when molecules rotate and translate in different molecular arrangements during crystallization. These molecular rearrangements impact the intermolecular bonding motifs associated with each polymorph. For example, for glycine, the β polymorph is composed of single molecular layers held together by hydrogen bonds.[18] The α polymorph is composed of hydrogen bonding double layers of glycine molecules, packed with van der Waals forces.[18] Since there are different intermolecular forces holding these crystals together, the crystal structures also have unique thermodynamic stabilities. For glycine the β polymorph is less stable compared to the α polymorph.[19]

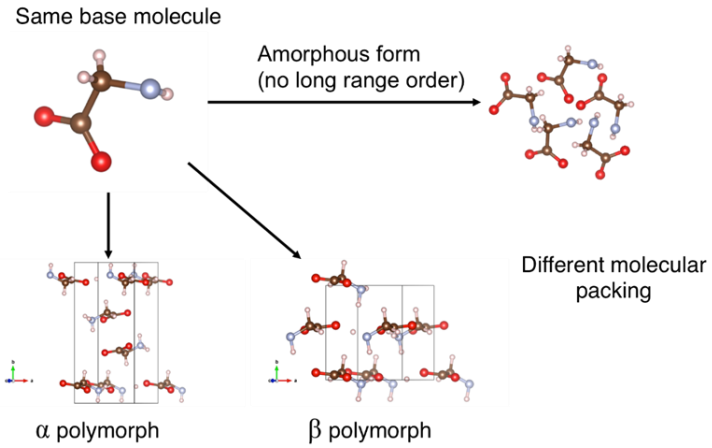

Figure 1.2 Polymorphs are crystals composed of the same molecular compounds. However, polymorphs have different crystal structures due to unique molecular arrangements within the lattice. Glycine can crystalize in several forms, for example α and β.

Ostwald's rule of stages states that molecules in less stable polymorphs are able to reorient, reconfigure and recrystallize in more stable crystal forms (e.g. β glycine can recrystallize as the more stable α polymorph).[20,21] Relevant to drug delivery, a solid converting to a more stable structure will exhibit lower solubility. Energy minimization and phase transformation will occur repeatedly until the globally stable structure is found, exhibiting the lowest solubility (**Figure 1.3**).

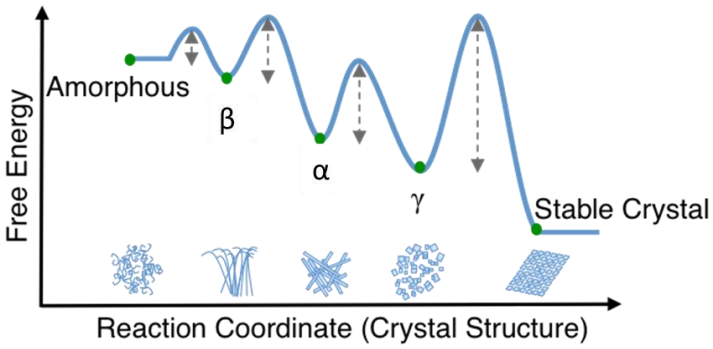

Figure 1.3 Schematic of potential energy description of solid states. Polymorphs are isolated in potential energy minima associated with their unique structures. The example of glycine is shown, with β having higher potential compared to α and γ glycine. Less stable phases can reconfigure as more stable phases until a globally stable structure is isolated.

Careful control of solid form is required for pharmaceutical delivery applications, because a drug product must both stable and soluble, two opposing properties. Polymorphism is known to affect the quality, safety, and efficacy of a drug product.[22] As such, the FDA has guidelines to thoroughly characterize solid state characteristics of drug candidates during development.[22,23] Anticipating the number and type of unique crystal structures that exist for a molecule is a significant challenge, since each molecule has a unique electron density, resulting in unique intermolecular interactions, which drive molecular packing during crystallization.

Polymorph characterization is carried out in screening processes, which are often material intensive, trial and error processes. Screening typically consists of solution-based crystallizations that change solvent environment, relative degree of supersaturation and crystallization time to sample a variety of thermodynamic and kinetic crystallization conditions.[24] However, there is no guarantee that a screen will find all of the polymorphs. Further, early in development the amount of material available to perform screening is limited, pushing for efficiency during the screening process. It is an advantage to have tools accessible to efficiently screen for multiple crystalline phases while sampling a wide variety of crystallization conditions (such as changing solvent, temperature, or concentration). Industry has focused on implementing high throughput screening and automation protocols to improve the efficiency, reproducibility and sample size of the polymorph screening process.[25]

1.1.2 Importance of crystal size and shape

Crystal size and shape are characteristics that are relevant to pharmaceutical development because they influence the timescale of drug delivery. The impact of crystal size on the rate of crystal dissolution is described by the Noyes-Whitney equation:[26]

$$\frac{dC}{dt} = \frac{DA(C_s - C)}{h}$$

Where $\frac{dC}{dt}$ is the dissolution rate of drug particles, D is the diffusivity of the drug in the surrounding solvent, A is the effective surface area of the drug particle, C_s is the saturation solubility of the drug in solution, C is the concentration of drug in the bulk fluid, and h is the thickness of the boundary layer. By this relationship, the dissolution rate is directly related to the particle size. As the particle size is decreased (while keeping mass constant) the surface area is increased (**Figure 1.4**). Formulations comprised of nanoparticles, nanocrystals and nanosuspensions have been employed to increase the dissolution rate of poorly soluble drugs.[26]

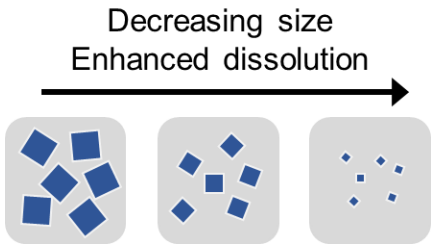

Figure 1.4 Particle size reduction is a technique to increase the dissolution rate for APIs. Controlling crystal size distribution is important to achieve a desired drug release profile.

By the same relationship, different crystal shapes can be selected to increase the effective surface area of the particle. Crystals grow with faceting that reflects preferential growth of certain crystal planes. Changing the solvent environment during crystallization can affect the faceting to minimize surface energy between the solvent and the growing crystal.[27] Through this, a crystal shape can range from high aspect ratio needles and plates to lower aspect ratio spheres or cubes while exhibiting the same crystal structure (polymorph).[12] Achieving non-equilibrium crystal shapes can be utilized as a technique to increase dissolution rate.[12,28] Studies have recently demonstrated enhanced dissolution rates that were achieved by changing the crystal shape, pushing the field towards producing spherical crystal shapes to modulate drug delivery timescales.[29] Finally, smaller and more spherical crystals are desirable from a material handling

perspective, because they have better flowability compared to needle shaped crystals, which can stick together and clog equipment.[30]

Decreasing the size of crystals can be achieved through mechanical processes like grinding or milling, which breaks larger crystals into smaller sizes.[31,32] Alternatively, crystal size can be affected by directly controlling crystallization conditions, such as the degree of supersaturation.[33] Spray drying has been employed as a technique for producing micro and nanocrystals of pharmaceutical materials.[34] The technique is advantageous because it is a continuous process with simple handles for controlling crystal size and shape (e.g. feed rate, nozzle size).[35,36]

1.1.3 Formulation

During formulation, the information gathered during solid state characterization (polymorphism, crystal shape, size) is utilized to design a strategy for drug delivery. Formulation entails integration of the API with additional materials which serve to protect the API from degradation or phase transformation while controlling the drug release kinetics. Typically, the product is a solid tablet with the selected polymorph, crystal size and shape as critical controlled parameters.

Raza et al provides a summary of guidelines for formulating materials, considering the existence of multiple polymorphs:[8]

1. The thermodynamically stable polymorph should be preferentially selected for development
2. Excipients should be utilized to enhance the bioavailability of the lowest energy polymorph prior to selecting a metastable form for development
3. If a metastable polymorph is selected for development the product must be stored such that it will not undergo transformations to a more stable form

4. If a polymorphic transition does occur throughout the products shelf life, it should not significantly affect the product quality and bioavailability

Formulation simultaneously addresses the stability and bioavailability of the API. While it is preferred to select the most stable polymorph, it is possible to select a metastable polymorph (as a method to increase solubility and bioavailability) as long as the drug product does not undergo any phase transformations.[37]

Incorporating polymer additives and coatings is a common approach to stabilize API formulation.[38] Coatings on the tablet surface are used to protect water sensitive materials from ambient environmental conditions and can act as a barrier to control the timescale of drug release.[39,40] Additives and excipients can be used to change the dissolution kinetics, either speeding them up or slowing them down.[41] There is interest in developing technologies to enhance the drug loading capacity in drug carriers.[42] Recently, metal organic frameworks (MOFs) have been presented as a scaffold for storage and delivery of APIs with the potential for achieving high drug loading.[43,44]

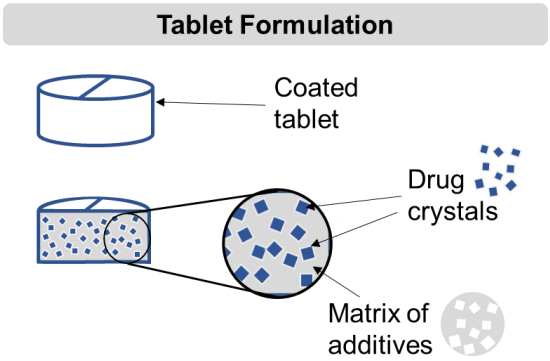

Figure 1.5 A tablet is formed by compressing additives (e.g. inert polymers and binders) and drug crystals to create a formed object. Tablets are typically coated on the outside to stabilize and protect internal components and make it easier to ingest.

1.2 Thin films as an emerging platform for drug delivery

Thin films can be employed for use in API formulations such as orally dissolving strips or transdermal patches.[45,46] Thin films have increased surface area to facilitate fast dissolution. Further, recent studies suggest that thin films can be used to control crystal polymorphism and morphology characteristics; the techniques employed include dropcasting, spin coating, printing and meniscus guided coating (**Figure 1.6**[47], from ©2014 Diao et al.; licensee, The Royal Society of Chemistry).

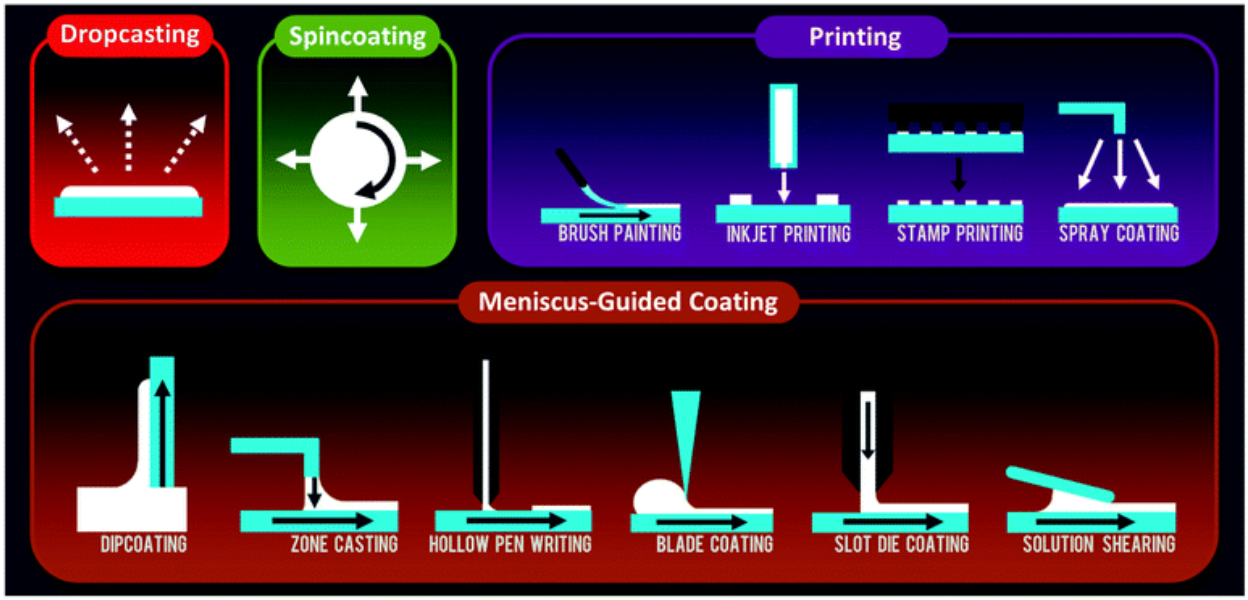

Figure 1.6 Overview of thin film fabrication methods typically used in organic semiconductor processing and recently explored for pharmaceutical crystallization (Figure from ©2014 Diao et al.; licensee, The Royal Society of Chemistry).

1.2.1 Dropcasting

In 2015, Reischl et al. drop-casted phenytoin on glass slides and dried in an oven to allow crystallization to occur.[48] Ethanol and tetrahydrofuran (THF) were used as solvents in film preparation, and the films formed using THF isolated multiple polymorphs. By studying the dissolution kinetics of these films, the researchers found enhanced solubility of the thin film polymorphisms relative to bulk; the polymorphic thin film exhibited greater than 2 times faster release kinetics, emphasizing the importance of controlling crystal polymorphism during drug discovery.

In 2019, Werzer et al used dropcasting to create pharmaceutical thin films of phenytoin, clotrimazole and indomethacin.[49] In this work, phenytoin crystallized on the silicon substrate while clotrimazole and indomethacin remained as amorphous forms throughout experimentation. Layering a polymer coating on the pharmaceutical films allowed for tunable drug release.

1.2.2 Spincoating

In 2014, Werzer et al. looked at the morphology and molecular packing of phenytoin deposited on a silica substrate using spincoating.[50] Crystal morphology was changed while crystal structure was unaffected by processing conditions. Dissolution was found to be enhanced for thin films compared to bulk, attributed to the enhanced surface area for solvent interaction compared to nanopores. The study showed dissolution on a shorter timescale for thin films compared to bulk material, and the maximum solubility observed was increased in the thin film sample.

In 2018, Simões et al. also used spincoating and changing solution concentrations to isolate forms I and II of piracetam.[51] The authors determined that the presence of polar groups in many pharmaceuticals contributes to their ability to form hydrogen bonds, impacting the intermolecular interactions that dictate crystallization.

1.2.3 Printing

Printing encompasses multiple approaches, including inkjet printing and 3D printing. Inkjet printing is promising for use in high throughput screening of crystal polymorphs and developing new formulations in pharmaceuticals.[52] Genina et al demonstrated the ability to print Loperamide hydrochloride and caffeine using inkjet printing.[53] They demonstrated the formation of a stable crystal phase for loperamide hydrochloride and partial recrystallization occurred with caffeine. The work provides a proof of concept for individualized dosing using printing technology. Spray drying is another printing technique that, in addition to controlling crystal size, can be used to create thin films.[54] 3D printing is a type of additive manufacturing that extends upon single layer printing

technologies. Multiple layers of drug material can be sequentially printed to enable formulation of tangible drug products with tunable drug release and custom doses.[55]

1.2.4 Meniscus guided coating techniques

Solution shearing is a meniscus guided coating (MGC) technique extensively studied and used in organic semiconductor and photovoltaic film deposition.[56,57] Giri et al. used solution shearing to fabricate thin films of an organic semiconductor, 6,13-Bis(triisopropylsilylethynyl)pentacene (TIPS-pentacene).[58] Using MGC enhanced organic thin film transistor performance by aligning crystals and tuning molecular packing, leading to and an increase charge carrier mobility.[59]

In 2018, Hortsman et al. applied the solution shearing technique to a pharmaceutical molecule, ellipticine.[60] In this work, polymorphism was observed to occur with changing solution concentration and shearing speed. Further, multilayer nanocomposites are created to address the need for scalability; the technique must be capable of forming larger amounts of material with controlled morphology and polymorphism for dosing potential.

These examples demonstrate promising results for thin films to be used for drug delivery. We look to utilize a thin film platform to explore the use of thin films for drug delivery, while controlling crystal attributes like polymorphism, size and shape. There is still a significant need for development and innovation before these technologies become feasible for implementation in the pharmaceutical industry.

1.3 Improving pharmaceutical manufacturing

Traditionally, the pharmaceutical industry has relied on batch and semi batch crystallization for the majority of compounds produced.[61,62] With batch technology, development at the lab bench does not translate to identical processing conditions at the pilot plant scale or at full scale manufacturing sites.[63] Lack of transferrable knowledge at different manufacturing scales is detrimental to product quality. Further, reworking process parameters in batch systems

contributes to process inefficiencies, and contributes to the enormous costs associated with pharmaceutical development.[63]

The FDA has urged pharmaceutical companies to adopt a quality by design approach (QbD) to improve development and manufacturing practices.[64] The goal of QbD is to minimize issues related to product quality, by designing manufacturing process that are reproducible and create products with controllable attributes. Among many areas for improvement, QbD can be achieved by developing and utilizing controlled and scalable process technology to enable continuous manufacturing processes and optimize processing conditions.[65] Already, there has been extensive work to develop scalable platforms to aid in critical steps of pharmaceutical production including the reaction and purification.[66,67] Continuous pharmaceutical manufacturing would streamline the process of creating a drug product by integrating synthesis, crystallization, granulation and tableting.[68] Therefore, the development of new manufacturing technologies should be carried out with this goal in mind.

This guides us in our pursuit of developing a platform for the fabrication of pharmaceutical thin films, while controlling critical material attributes (crystal polymorphism, size and morphology). Of the thin film fabrication techniques outlined, printing and meniscus guided coating provide the advantage of being easily scalable, and are thus the techniques explored in this dissertation.

1.4 Summary of dissertation

MGC is a promising, scalable technique to produce thin films of pharmaceutical molecules. This dissertation explores the application of the technique to control various parameters relevant in pharmaceutical crystallization, including polymorphism, size and shape. Beyond MGC platforms, I present work towards understanding drug loading and release, through the development of 3D printed tablets and a nanofluidic device for visualizing molecular transport in metal organic frameworks for eventual drug delivery applications.

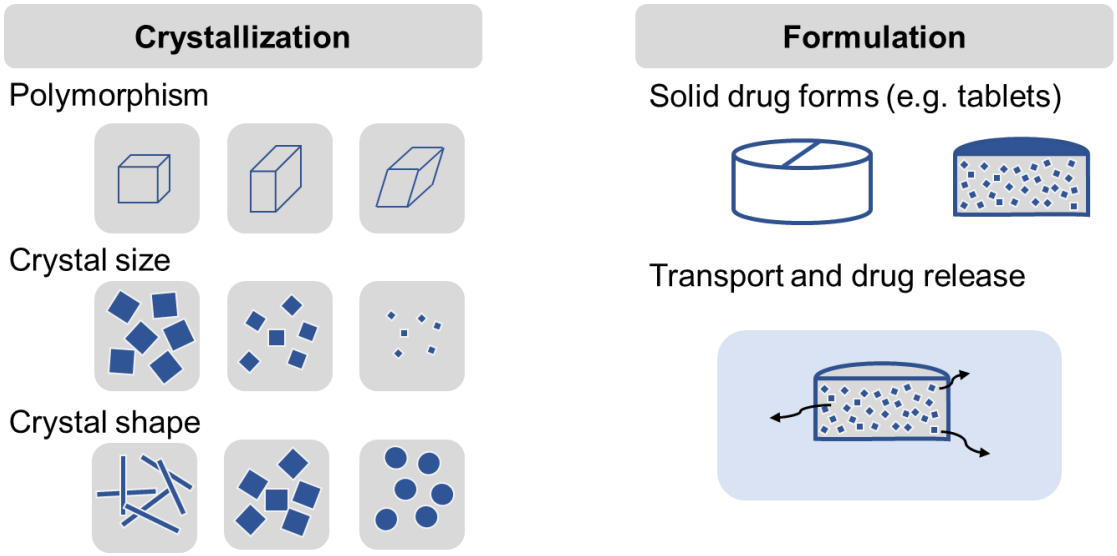

Figure 1.7 A summary of important considerations during drug development, ranging from crystallization to formulation. Polymorphism, crystal size and crystal shape can impact drug performance. 3D printed tablets are created as a solid drug form with crystals in a polymer matrix. Small molecule transport within metal organic frameworks is discussed for drug delivery.

1.4.1 Polymorphism in APIs using solution shearing

A tool for polymorph screening is developed and characterized in Chapter 2 and Chapter 3 of this dissertation. Chapter 2 presents MGC for creating thin films of glycine and acetaminophen and finds that tunable film thickness is significant for isolating polymorphs for these materials. Chapter 3 studies the coating process in-situ using synchrotron based grazing incidence X-ray diffraction to understand the mechanism of crystallization and formation of different crystal orientations within thin films during coating.

1.4.2 Size and shape control of APIs using solution shearing

In this work (chapter 4), solution shearing is employed as a meniscus guided coating technique for controlling the size and shape of crystals. Acetaminophen microcrystals are created with this technology through operation with novel coating conditions. A new coating regime is characterized and we present a hypothesis for the existence of a nucleation dominant crystallization regime.

1.4.3 Developing technologies for novel formulations

In chapter 5, a nanofluidic platform was developed for MOF crystallization, allowing for fundamental study of small molecule/MOF transport. A MOF (HKUST-1) was crystallized in the device and is demonstrated to have the capacity for selective small molecule storage. The platform serves as a tool for characterizing small molecule transport in metal organic frameworks. This work presents strides in fundamental understanding of MOF/small molecule interactions. Such work is necessary to guide and inform technological development prior to implementation of MOF technology for drug delivery for consumer use.

In chapter 6, 3D printing is utilized to create drug loaded polymer tablets. A polymer/API (poly vinyl alcohol/glycine) gel was developed to enable extrusion-based printing. Tablets ranging from 1 to 50 layers were created and characterized to determine crystal form and interactions between the drug and polymer matrix. Tablet dissolution was assessed using spectroscopy.

Finally, the dissertation is concluded by presenting future directions for exploration related to MGC for pharmaceutical crystallization and formulation development.

1.5 References

1. Wouters, O. J., McKee, M. & Luyten, J. Estimated Research and Development Investment Needed to Bring a New Medicine to Market, 2009-2018. *JAMA - J. Am. Med. Assoc.* **323**, 809–902 (2020).

2. Dunne, S., Shannon, B., Dunne, C. & Cullen, W. A review of the differences and similarities between generic drugs and their originator counterparts, including economic benefits associated with usage of generic medicines, using Ireland as a case study. *BMC Pharmacol. Toxicol.* **14**, (2013).

3. Woodcock, J. & Woosley, R. The FDA Critical Path Initiative and Its Influence on New Drug Development. *Annu. Rev. Med.* **59**, 1–12 (2008).

4. Center of Drug Evaluation and Research. Regulatory classification of pharmaceutical co-crystals, guidance for industry. *Food Drug Adm. U.S. Dep. Heal. Hum. Serv.* (2018).

5. Patel, P. Preformulation Studies: An Integral Part of Formulation Design. in *Pharmaceutical Formulation Design - Recent Practices* (2020). doi:10.5772/intechopen.82868.

6. Urwin, S. J. *et al.* A Structured Approach to Cope with Impurities during Industrial Crystallization Development. *Org. Process Res. Dev.* **24**, 1443–1456 (2020).

7. Fujiwara, M., Nagy, Z. K., Chew, J. W. & Braatz, R. D. First-principles and direct design approaches for the control of pharmaceutical crystallization. *J. Process Control* **15**, 493–504 (2005).

8. Raza, K. Polymorphism: The Phenomenon Affecting the Performance of Drugs. *SOJ Pharm. Pharm. Sci.* **1**, 10 (2014).

9. Couillaud, B. M., Espeau, P., Mignet, N. & Corvis, Y. State of the Art of Pharmaceutical Solid Forms: from Crystal Property Issues to Nanocrystals Formulation. *ChemMedChem* **14**, 8–23 (2019).

10. Gardner, C. R., Walsh, C. T. & Almarsson, Ö. Drugs as materials: Valuing physical form in drug discovery. *Nat. Rev. Drug Discov.* **3**, 926–934 (2004).

11. Baghel, S., Cathcart, H. & O'Reilly, N. J. Polymeric Amorphous Solid Dispersions: A Review of Amorphization, Crystallization, Stabilization, Solid-State Characterization, and Aqueous Solubilization of Biopharmaceutical Classification System Class II Drugs. *J. Pharm. Sci.* **105**, 2527–2544 (2016).

12. Tiwary, A. K. Modification of crystal habit and its role in dosage form performance. *Drug Dev. Ind. Pharm.* **27**, 699–709 (2001).

13. Brown, C. J. *et al.* Enabling precision manufacturing of active pharmaceutical ingredients: workflow for seeded cooling continuous crystallisations. *Mol. Syst. Des. Eng.* **3**, 518–549 (2018).

14. Chemburkar, S. R. *et al.* Dealing with the Impact of Ritonavir Polymorphs on the Late Stages of Bulk Drug Process Development. *Org. Process Res. Dev.* **4**, 413–417 (2000).

15. Morissette, S. L., Soukasene, S., Levinson, D., Cima, M. J. & Almarsson, Ö. Elucidation of crystal form diversity of the HIV protease inhibitor ritonavir by high-throughput crystallization. *Proc. Natl. Acad. Sci. U. S. A.* **100**, 2180–2184 (2003).

16. Bauer, J. *et al.* Ritonavir: An extraordinary example of conformational polymorphism. *Pharm. Res.* **18**, 859–866 (2001).

17. Mahase, E. FDA recalls ranitidine medicines over potential cancer causing impurity. *BMJ* (2019) doi:10.1136/bmj.l5832.

18. Iitaka, Y. The crystal structure of γ-glycine. *Acta Crystallogr.* **14**, 1–10 (1961).

19. Moggach, S. A., Marshall, W. G., Rogers, D. M. & Parsons, S. How focussing on hydrogen bonding interactions in amino acids can miss the bigger picture: A high-pressure neutron powder diffraction study of ε-glycine. *CrystEngComm* (2015) doi:10.1039/c5ce00327j.

20. Ostwald, W. Studien uber die Bildung und Umwandlung fester Korper. *Zeitschrift für Phys. Chemie* **22**, 289–302 (1897).

21. Burley, J. C., Duer, M. J., Stein, R. S. & Vrcelj, R. M. Enforcing Ostwald's rule of stages: Isolation of paracetamol forms III and II. *Eur. J. Pharm. Sci.* **31**, 271–276 (2007).

22. Food and Drug Administration. Guidance for Industry Regulatory Classification of Pharmaceutical Co-Crystals. *FDA* (2013).

23. Food and Drug Administration. Guidance for Industry; ANDAs: Pharmaceutical Solid Polymorphism; Chemistry, Manufacturing, and Controls Information. (2007).

24. Braun, D. E. *et al.* Solid-state forms of β-resorcylic acid: How exhaustive should a polymorph screen be? *Cryst. Growth Des.* **11**, 210–220 (2011).

25. Müller, M. *et al.* Process development strategy to ascertain reproducible API polymorph manufacture. *Cryst. Growth Des.* **6**, 946–954 (2006).

26. Dizaj, S. M., Vazifehasl, Z., Salatin, S., Adibkia, K. & Javadzadeh, Y. Nanosizing of drugs: Effect on dissolution rate. *Res. Pharm. Sci.* **10**, 95–108 (2015).

27. Li, J. & Doherty, M. F. Steady state morphologies of paracetamol crystal from different solvents. *Cryst. Growth Des.* **17**, 659–670 (2017).

28. Ren, Y. *et al.* Impact of crystal habit on solubility of ticagrelor. *Crystals* **9**, 556 (2019).

29. Pena, R., Oliva, J. A., Burcham, C. L., Jarmer, D. J. & Nagy, Z. K. Process Intensification through Continuous Spherical Crystallization Using an Oscillatory Flow Baffled Crystallizer. *Cryst. Growth Des.* **17**, 4776–4784 (2017).

30. Mahanty, S., Sruti, J., Patra, C. N. & Rao, M. E. B. Particle Design of Drugs by Spherical Crystallization Techniques. *Int. J. Pharm. Sci. Nanotechnol.* (2010).

31. Chaudhary, A. *et al.* Enhancement of solubilization and bioavailability of poorly soluble drugs by physical and chemical modifications: A recent review. *J Adv Pharm Educ Res* **2**, 32–67 (2012).

32. Yang, Y., Song, L., Gao, T. & Nagy, Z. K. Integrated Upstream and Downstream Application of Wet Milling with Continuous Mixed Suspension Mixed Product Removal Crystallization. *Cryst. Growth Des.* **15**, 5879–5885 (2015).

33. Wu, Z., Yang, S. & Wu, W. Application of temperature cycling for crystal quality control during crystallization. *CrystEngComm* **18**, 2222–2238 (2016).

34. Babcock, W. C., Friesen, D. T., Nightingale, J. A. S. & Shanker, R. M. Pharmaceutical solid dispersions. (2013).

35. Jain, M. *et al.* Spray Drying in Pharmaceutical Industry: A Review. *Res. J. Pharm. Dos. Forms Technol.* (2012).

36. Ziaee, A. *et al.* Spray drying of pharmaceuticals and biopharmaceuticals: Critical parameters and experimental process optimization approaches. *Eur. J. Pharm. Sci.* **127**, 300–318 (2019).

37. Singhal, D. & Curatolo, W. Drug polymorphism and dosage form design: A practical perspective. *Advanced Drug Delivery Reviews* vol. 56 335–347 (2004).

38. Long, B., Ryan, K. M. & Padrela, L. Investigating Process Variables and Additive Selection to Optimize Polymorphic Control of Carbamazepine in a CO2Antisolvent Crystallization Process. *Org. Process Res. Dev.* **24**, 1006–1017 (2020).

39. Gendre, C. *et al.* Comprehensive study of dynamic curing effect on tablet coating structure. *Eur. J. Pharm. Biopharm.* **81**, 657–665 (2012).

40. Algahtani, M. S., Mohammed, A. A., Ahmad, J. & Saleh, E. Development of a 3D printed coating shell to control the drug release of encapsulated immediate-release tablets. *Polymers (Basel).* **12**, 1395 (2020).

41. Solorio, L., Sundarapandiyan, D., Olear, A. & Exner, A. A. The Effect of Additives on the Behavior of Phase Sensitive in Situ Forming Implants. *J. Pharm. Sci.* **104**, 3471–3480 (2015).

42. Müller, R. H., Mäder, K. & Gohla, S. Solid lipid nanoparticles (SLN) for controlled drug delivery - A review of the state of the art. *Eur. J. Pharm. Biopharm.* **50**, 161–177 (2000).

43. Fernández-Paz, C. *et al.* Metal-Organic Framework Microsphere Formulation for Pulmonary Administration. *ACS Appl. Mater. Interfaces* **12**, 25676–25682 (2020).

44. Tibbetts, I. & Kostakis, G. E. Recent Bio-Advances in Metal-Organic Frameworks. *Molecules* **25**, 1291 (2020).

45. Karki, S. *et al.* Thin films as an emerging platform for drug delivery. *Asian J. Pharm. Sci.* **11**, 559–574 (2016).

46. Irfan, M. *et al.* Orally disintegrating films: A modern expansion in drug delivery system. *Saudi Pharm. J.* **24**, 537–546 (2016).

47. Diao, Y., Shaw, L., Bao, Z. & Mannsfeld, S. C. B. Morphology control strategies for solution-processed organic semiconductor thin films. *Energy Environ. Sci.* **7**, 2145–2159 (2014).

48. Reischl, D. *et al.* Surface-Induced Polymorphism as a Tool for Enhanced Dissolution: The Example of Phenytoin. *Cryst. Growth Des.* **15**, 4687–4693 (2015).

49. Werzer, O., Tumphart, S., Keimel, R., Christian, P. & Coclite, A. M. Drug release from thin films encapsulated by a temperature-responsive hydrogel. *Soft Matter* **15**, 1853–1859 (2019).

50. Werzer, O., Baumgartner, R., Zawodzki, M. & Roblegg, E. Particular Film Formation of Phenytoin at Silica Surfaces. *Mol. Pharm.* **11**, 610–616 (2014).

51. Simões, R. G., Salzmann, I., Resel, R., Röthel, C. & Geerts, Y. H. Stabilization of the Metastable Form I of Piracetam by Crystallization on Silicon Oxide Surfaces. *Cryst. Growth Des.* **18**, 4123–4129 (2018).

52. Scoutaris, N., Ross, S. & Douroumis, D. Current Trends on Medical and Pharmaceutical Applications of Inkjet Printing Technology. *Pharm. Res.* **33**, 1799–1816 (2016).

53. Genina, N., Fors, D., Palo, M., Peltonen, J. & Sandler, N. Behavior of printable formulations of loperamide and caffeine on different substrates - Effect of print density in inkjet printing. *Int. J. Pharm.* **453**, 488–497 (2013).

54. Jacquot, M. & Pernetti, M. Spray Coating and Drying Processes. in *Fundamentals of Cell Immobilisation Biotechnology. Focus on Biotechnology* (Springer, Dordrecht, 2004). doi:https://doi.org/10.1007/978-94-017-1638-3_19.

55. Khaled, S. A., Burley, J. C., Alexander, M. R., Yang, J. & Roberts, C. J. 3D printing of five-in-one dose combination polypill with defined immediate and sustained release profiles. *J. Control. Release* **217**, 308–314 (2015).

56. Gu, X., Shaw, L., Gu, K., Toney, M. F. & Bao, Z. The meniscus-guided deposition of semiconducting polymers. *Nat. Commun.* **9**, 534 (2018).

57. Pascoe, A. R. *et al.* Directing nucleation and growth kinetics in solution-processed hybrid perovskite thin-films. *Sci. China Mater.* 617–628 (2017) doi:10.1007/s40843-017-9043-y.

58. Giri, G. *et al.* Tuning charge transport in solution-sheared organic semiconductors using lattice strain. *Nature* **480**, 504 (2011).

59. Giri, G. *et al.* One-dimensional self-confinement promotes polymorph selection in large-area organic semiconductor thin films. *Nat. Commun.* **5**, 3573 (2014).

60. Horstman, E. M. *et al.* Solution Coating of Pharmaceutical Nanothin Films and Multilayer Nanocomposites with Controlled Morphology and Polymorphism. *ACS Appl. Mater. Interfaces* **10**, 10480–10489 (2018).

61. Cole, K. P. & Johnson, M. D. Continuous flow technology vs. the batch-by-batch approach to produce pharmaceutical compounds. *Expert Rev. Clin. Pharmacol.* **11**, 5–13 (2018).

62. McWilliams, J. C. *et al.* The Evolving State of Continuous Processing in Pharmaceutical API Manufacturing: A Survey of Pharmaceutical Companies and Contract Manufacturing Organizations. *Org. Process Res. Dev.* **22**, 1143–1166 (2018).

63. Suresh, P. & Basu, P. K. Improving pharmaceutical product development and manufacturing: Impact on cost of drug development and cost of goods sold of pharmaceuticals. *J. Pharm. Innov.* **3**, 175–187 (2008).

64. Yu, L. X. *et al.* Understanding pharmaceutical quality by design. *AAPS J.* **16**, 771–783 (2014).

65. Poechlauer, P., Manley, J., Broxterman, R., Gregertsen, B. & Ridemark, M. Continuous processing in the manufacture of active pharmaceutical ingredients and finished dosage forms: An industry perspective. *Org. Process Res. Dev.* **16**, 1586–1590 (2012).

66. Zhang, P. *et al.* Advanced Continuous Flow Platform for On-Demand Pharmaceutical Manufacturing. *Chem. - A Eur. J.* **24**, 2776–2784 (2018).

67. Imbrogno, J., Rogers, L., Thomas, D. A. & Jensen, K. F. Continuous purification of active pharmaceutical ingredients utilizing polymer membrane surface wettability. *Chem. Commun.* **54**, 70–73 (2017).

68. Steve Kuehn. Pharmaceutical Manufacturing: Current Trends and What's Next. *Chemical Engineering Progress* (2018).

Chapter 2. Controlling polymorphism using solution shearing

2.1 Abstract

In this work, two model pharmaceutical compounds, glycine and acetaminophen, were crystallized using a meniscus guided coating technique, termed solution shearing, to create thin films with controllable polymorphism. Controlling polymorphism in pharmaceutical compounds can provide optimized solubility and bioavailability. Thin films of glycine and acetaminophen were obtained using a simple flow coating method, and these films were characterized using cross polarized optical microscopy and grazing incidence X-ray diffraction. Films crystallized as different polymorphs (α and β for glycine and form I and form II for acetaminophen) by controlling processing temperature and shearing speed. The amorphous phase of acetaminophen was also stabilized, and the kinetic transformation to the metastable form II was studied. We hypothesize that one-dimensional confinement plays a significant role in stabilizing metastable polymorphs and amorphous phases. Solution shearing has the potential to be used as a high throughput technique to screen polymorphs in industry.

2.2 Introduction

In the pharmaceutical industry, significant resources are allocated to control the stability and solubility of a drug product, as the drug needs to be stable during processing and storage, and follow predictable dissolution kinetics in the body.[1] For small organic molecules, most drug products are stored and ingested as solid forms.[2] The crystal morphology and the packing (polymorphism) of the pharmaceutical compound in the solid drug product determine the solubility and the associated bioavailability.[3] The bioavailability of many newly developed drug candidates

Parts of this work are published or in preparation for publication as:

1. Stephanie Guthrie., Detlef-M. Smilgies, and Gaurav Giri. "Controlling polymorphism in pharmaceutical compounds using solution shearing." *Crystal Growth & Design* 18.2 (2018): 602-606. Figures used with permission.
2. Stephanie Guthrie, Yuan Gau, Baoxing Xu, Gaurav Giri. “Probing molecular assembly of small organic molecules during meniscus guided coating using experimental and molecular dynamics approaches.” *(in preparation).*

is a concern, as the drugs are practically insoluble.[4,5] Making drugs readily available in the body has emerged as a challenge that prevents many newer candidates from being pushed forward in development. If candidate drugs have improved solubility and bioavailability, these candidates can be screened with greater emphasis on their biological efficacy. Numerous methods are being researched or used in industry to increase the biological activity of insoluble drugs, but at the cost of increased complexity during formulation.[6]

We aim to control the formation of amorphous and metastable crystalline solid-state phases to improve the solubility of the active pharmaceutical ingredient (API).[7] Nonequilibrium (including metastable polymorphs and amorphous solid phases) formulations are a promising route for increased solubility since the nonequilibrium solid phase is, by definition, less stable than the equilibrium phase. Not only is it advantageous to obtain polymorphs with increased solubility, but regulatory agencies mandate that (1) polymorphs, solvates, hydrates, and amorphous forms of drug compounds are known, (2) potential phase transformations are well characterized, and (3) each polymorphic form is patented separately for development.[8] Gaining this understanding is important because, while lower stability polymorphs have enhanced dissolution, they may also have reduced shelf life. Controlling kinetics of phase transformations is thus an important area of study.

The search for polymorphs with better solubility, coupled with regulatory guidelines to characterize all known polymorphs, has pushed pharmaceutical companies to carry out extensive searches in the API development phase to identify as many drug polymorphs as possible. However, there are no generally applicable routes for finding polymorphs. Many different trial-and-error methods are combined and employed to induce polymorphism, including variable solvent input, thermal cycling, and additives (including cocrystals, cosolvents, and excipients).[9] Other methods to obtain polymorphs are being researched, such as computational structure prediction, vapor exposure, crystallization on treated surfaces, thin films, and capillary crystallization.[10–14]

Recently, nanoscale confinement methods such as crystallization in controlled pore glass and nanodrops have shown great utility in obtaining or stabilizing polymorphs of numerous pharmaceutical compounds.[15–18] These results suggest that there is a fundamental connection between confined environments and metastable crystallization.[19] However, these methods do not yield significant amounts of the metastable polymorph for further testing and processing.

In the field of organic electronics, polymorphs are also of great importance for reliably and consistently preparing high performance devices. A solution based crystallization technique termed solution shearing has recently been extensively utilized to control the polymorphism of organic semiconductors.[20,21] Solution shearing can be scaled up for high-throughput industrial production while preserving lab results.[22] Giri et al. have previously showed that in solution shearing, one-dimensional confinement is responsible for obtaining metastable polymorphs of organic semiconductors.[23] We build upon this work to understand how one-dimensional confinement can control pharmaceutical solid-state behavior. Previous studies have outlined numerous routes to stabilize various polymorphs of glycine and acetaminophen, making them ideal molecules to understand the influence of one-dimensional confinement on API polymorphism.[24,25] We show controllable polymorphism in glycine and acetaminophen by changing solution shearing conditions. We also stabilize the amorphous form of acetaminophen and study the transformation to crystalline phases. We foresee that solution shearing will have vast utility in screening candidate drug molecules to determine the polymorphic landscape with minimal material usage.

2.3 Materials and Methods

Materials

Glycine (98.5%) and acetaminophen (98%) were obtained from Sigma-Aldrich. Protocol® deionized water was obtained from Thermo Scientific. Small organic molecules were dissolved in de-ionized water at a concentration of 10 mg/mL for all experiments.

Films were formed using a solution shearing setup consisting of a heat source (IKA RTC Basic hot-plate), linear driver (Harvard Apparatus PHD 2000 infuse/withdraw syringe pump), substrate, and shearing blade. The volumetric flow rate and input diameter on the syringe pump were set such that a desired linear coating speed was obtained.

Silicon wafers cut into approximately 1 cm^2 pieces were used as substrates. Wafers from Silicon Quest International were 100 mm in diameter and 500 μm thick with native oxide surface and crystallographic orientation <1 0 0>. Silicon wafers were washed using toluene, acetone, DI water, and isopropyl alcohol then dried using air. Prior to shearing, clean wafers were exposed to ultraviolet light (BioForce UV/Ozone ProCleaner) for at least 15 minutes to render the surface hydrophilic.

A silicon wafer shearing blade was functionalized with 1H,1H,2H,2H-Perfluorooctyltriethoxysilane (FTS) (98%, Sigma-Aldrich). To functionalize the surface, a wafer was cut to size and cleaned with toluene, acetone, IPA and dried with air. The clean blade was then placed in a UV/ozone chamber for 15 minutes. The UV activated blade was sealed in a vacuum desiccator with 200 uL of silane and left under vacuum for 8 hours to form a vapor deposited hydrophobic surface.

Clean wafer substrates were removed from the UV chamber prior to shearing. After securing the wafer to the hotplate with double sided tape (3M). The FTS functionalized shearing blade was placed on top of the substrate and ~20 μL of prepared solution (10 mg/mL) was placed at the blade/substrate interface. Capillary action distributed the solution between the blade and substrate. Translation of the blade across the substrate created the evaporation front, and

evaporation of the solvent gave rise to the solid thin film. The range of temperatures (70 - 100℃) and shearing speeds (0.027 - 3 mm s^{-1}) were selected to obtain uniform thin film behavior. The films were characterized using white light interferometry, polarized optical microscopy, and X-ray diffraction.

Characterization

A Zygo NewView 7300 Optical Surface Profiler (Zygo Corporation, Middlefield, CT) was used to measure film thickness. Films were scratched to reveal the silicon substrate. Samples were sputter coated and the relative difference between peak (film surface) and valley (scratched region with exposed substrate) was taken as the film thickness. Measurements were taken in several regions and line scans were taken to obtain roughness and thickness variation across the sample. MetroPro software was used to collect and analyze data.

Optical images were acquired on a Zeiss Axio A.1 Microscope (Carl Zeiss AG, Oberkochen, Germany) with 5x, 10x, 20x, 50x objective lenses, using brightfield and cross-polarized light.

Grazing incidence X-ray diffraction (GIXD) was carried out at the Cornell High Energy Synchrotron Source (CHESS). The D1 beamline incident X-rays ranged in wavelength 0.1162-0.117 nm through two beamtime runs. The incident angle was 0.15˚. Reflections were recorded using a Pilatus 200K (Dectris USA Inc., Philadelphia, PA) detector located 160-180 mm from the sample. The 2D data was analyzed using the indexGIXS software pack developed by Detlef Smilgies.[26] Fit2d was used to integrate 2D diffraction images.[27] Mercury was used to produce simulated powder patterns from deposited CIF data in the Cambridge crystal structure database from previous literature.[28–31]

2.4 Results and Discussion

Solution shearing was used to create pharmaceutical thin films of glycine and acetaminophen. In this method, a solution containing the solute of interest is placed between a bottom heated substrate and a top shearing blade. As the top blade is translated, solution is spread across the substrate and an evaporation front is created at the meniscus. As the solvent evaporates, the solution becomes supersaturated and the solute nucleates, forming a solid thin film (**Figure 2.1**).

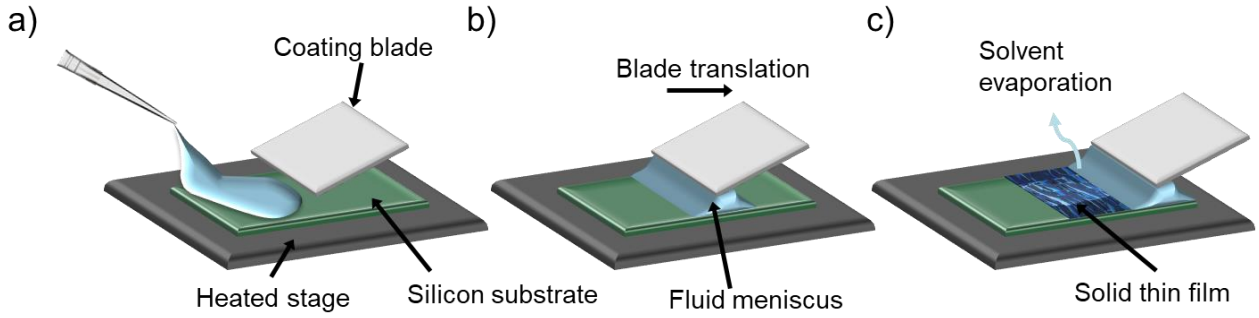

Figure 2.1 Conceptual image of the solution shearing technique. a) Fluid loading between the coating blade and substrate. b) A fluid meniscus forms as the blade is translated across the heated substrate. c) Fluid evaporation from the meniscus deposits a solid thin film.

We obtain different crystal thickness and morphologies by varying the temperature and coating speed.[32] In the conditions used in this study, the solution shearing process operates in the evaporative regime, characterized by decreasing solid film thickness with increasing blade speed (**Figure A2.1**). In the evaporative regime, the time scales of solution coating speed (which controls fluid deposition) and evaporation (which controls solid state formation) are similar. Therefore, controlling either the coating speed or the substrate temperature impacts the resulting film thickness. We can vary this thickness from tens of nanometers to several microns (**Figure A2.1**).

A representative case of solution shearing at 90 °C shows the effect of coating speed on the crystalline morphologies of glycine and acetaminophen (**Figure 2.2).** For glycine, crystalline films were formed in all cases. Large, continuous crystalline domains were obtained when the film

was cast at speeds of 0.1 mm s^{-1} or slower (**Figure 2.2a**). Conversely, thinner, needle-like crystals appeared at faster speeds (**Figure 2.2b**). In both cases, the crystals were aligned with the coating

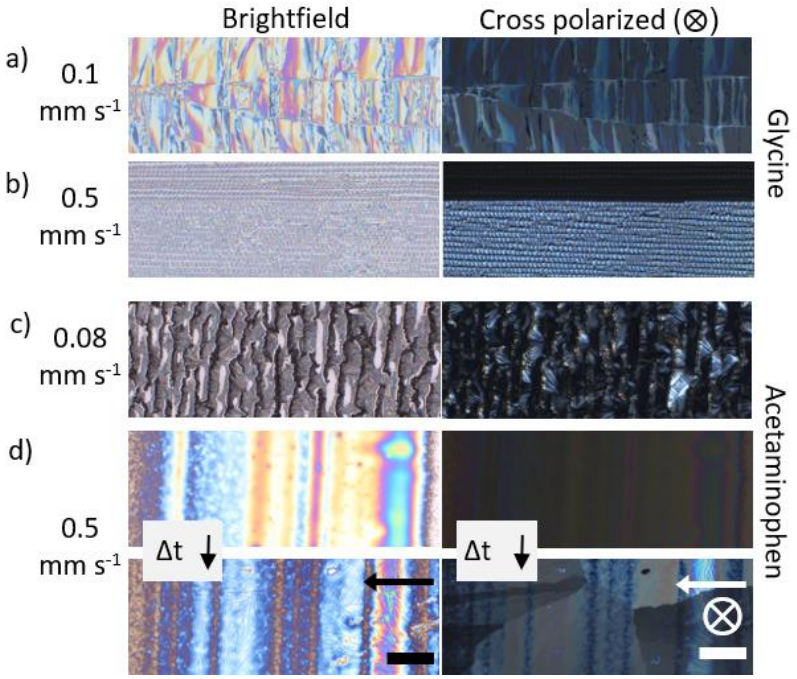

Figure 2.2 Brightfield and cross polarized optical microscopy (⊗) of glycine (a, b) and acetaminophen films (c, d) Subfigure (d) shows amorphous to crystalline transition. All films were formed at 90 °C. Shearing direction is indicated with arrow, similar for all images. Scale bars are 100 μm, similar for all images.

direction (**Figure A2.2**). A comprehensive discussion of the effect of coating speed on glycine alignment is included in the appendix (**Figures A2.4, Figure A2.5, Figure A2.6, Figure A2.7**), where the degree of polarization is used to quantify relative changes in crystal alignment.

For acetaminophen, either amorphous or crystalline phases could be obtained after solution shearing, with the amorphous phase eventually transforming to a crystalline film over a longer time scale. At slow coating speeds (0.08 mm s^{-1} and slower, **Figure 2.2c**), crystalline films were deposited. The film texture was nonuniform, with stick–slip motion during coating causing bands of thick and thin crystalline regions.[33] Coating speeds of 0.5 mm s^{-1} or greater (**Figure 2.2d**) produced an amorphous thin film that transformed into a spherulitic crystalline film. These crystalline films were isotropic in the plane of the substrate.

Grazing incidence X-ray diffraction was used to determine the crystal polymorph of glycine and acetaminophen. The peak positions are identical to previously obtained polymorphs for the APIs (**Figure 2.3**, **Figure A2.8**). For glycine, the α (monoclinic, P21/n) and β (monoclinic, $P2_1$,)

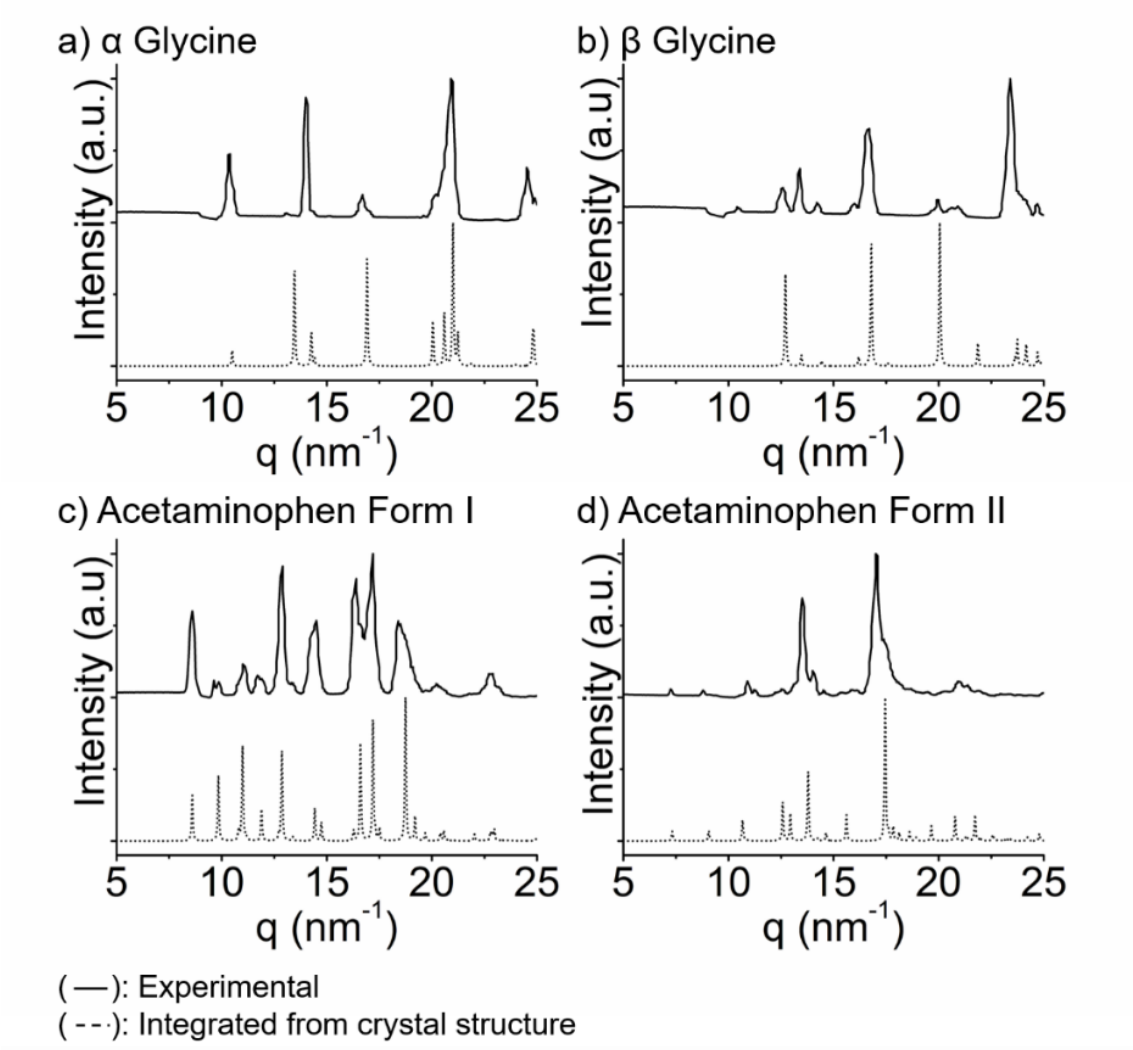

Figure 2.3 Representative scans obtained from integrating two-dimensional (2D) grazing incidence X-ray diffraction (GIXD) patterns. Dashed patterns are literature reported data (a) α glycine formed at 70 °C, 0.03 mm s^{-1}, (b) β glycine formed at 80 °C and 0.11 mm s^{-1}, (c) acetaminophen form I formed at 100 °C, 0.03 mm s^{-1}, (d) acetaminophen form II formed at 100 °C and 0.5 mm s^{-1}.

phases were obtained, and the γ polymorph was not isolated in this study.[28,29] Both α and β are metastable polymorphs, however at 25 °C and 1 atm, β is the less stable polymorph. For acetaminophen, form I (monoclinic, equilibrium) and form II (orthorhombic, metastable)

polymorphs were obtained.[30,31] It was observed that the amorphous phase formed during solution shearing of acetaminophen preferentially crystallized as form II.

We show reproducible formation of equilibrium and metastable polymorphs by varying solution coating speed (0.027–3.0 mm s^{-1}) and temperature (70–100 °C). The processing diagrams in **Figure 2.4** and **Figure A2.9** show that pure phases are isolated at the slowest and fastest coating speeds, with intermediate speeds producing both polymorphs. The transformation boundary—where the polymorph selection changes—was studied in more detail by increasing the sample size.

For glycine, the films had a tendency to form as pure α or β polymorph. A relationship between the crystal morphology and polymorph could be obtained. Large crystalline domains

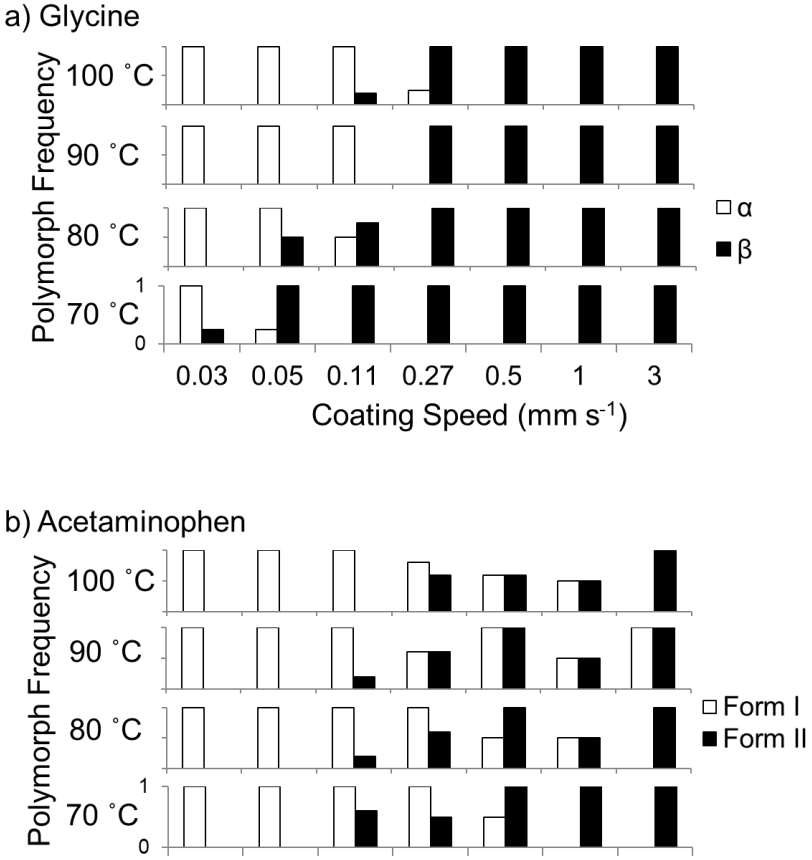

Figure 2.4 Relative frequency of polymorph occurrence was assembled into bar graphs, arranged by coating speed and temperature for (a) glycine and (b) acetaminophen. Polymorph selection is influenced by the solution shearing speed. Column graphs indicate the relative occurrence of each polymorph in the films. Summation of the bar graphs over 1 for any condition indicates film formation with multiple polymorphs in one sample.

were preferentially composed of the α polymorph, while needle-like crystals were preferentially composed of the β polymorph. No interconversion occurred during solution shearing. However, due to variability in the solution shearing process, both polymorphs could be obtained at the transformation boundary.

For acetaminophen, the pure polymorphic films were isolated at conditions characterized by fast/slow coating speeds. The amorphous films formed by solution shearing at faster speeds consistently crystallized as the form II polymorph, while the acetaminophen films solution sheared at lower speeds crystallized as the form I polymorph. However, the intermediate region (characterized by coating speeds 0.11–0.5 mm s^{-1}) captured a transition between amorphous and crystalline behavior, where films with both forms I and II were observed.

It is not surprising for both polymorphs to be present in a film when the samples are processed at intermediate conditions, as nucleation is a stochastic process.[34] It is likely that at the transformation boundary, free energies of formation for the metastable form II and the equilibrium form I are similar, giving rise to both polymorphs.

For glycine, previous literature has reported that α glycine is more stable than β glycine and for acetaminophen, stability follows as form I > form II > amorphous phase.[16,35,36] Therefore, for both molecules, the faster coating speeds (which create the thinnest films), isolate the less stable polymorph (**Figure 2.1b, Figure 2.4**).[32] This result supports the hypothesis that the one-dimensional confinement of the film thickness during solution shearing is responsible for the stabilization of metastable polymorphs.[23] It is also important to note that the transformation boundary for both glycine and acetaminophen occurs at similar temperatures and coating speeds, indicating that for these molecules, one-dimensional confinement is significant in directing polymorph selection at similar thicknesses.

The ability to change processing conditions without changing techniques to create different polymorphs is relevant to the pharmaceutical industry, where it is desirable to screen for the existence of multiple polymorphs quickly. It is convenient that the metastable forms are

isolated at faster speeds for both molecules tested. This is ideal both for scaled up processing and high throughput screening for metastable solid phases.

Glycine does not deposit as an amorphous film because the time scales for crystal nucleation and growth are similar to the time scale of film deposition. However, for acetaminophen, the time scale for nucleation is slower than for solid film formation at faster coating speeds. This mismatch enabled us to isolate the amorphous phase. We were also able to obtain amorphous phases of another molecule, carbamazepine (**Figure A2.10**). The transient crystallization dynamics of acetaminophen were studied to construct a solid-state transformation diagram (**Figure 2.5**) based on the coating speed. The operating lines specify the beginning of the solid-state change from amorphous to crystalline (marked by the first optical activity under polarized light), and the end of the solid-state phase change (signified by a fully crystalline thin film).

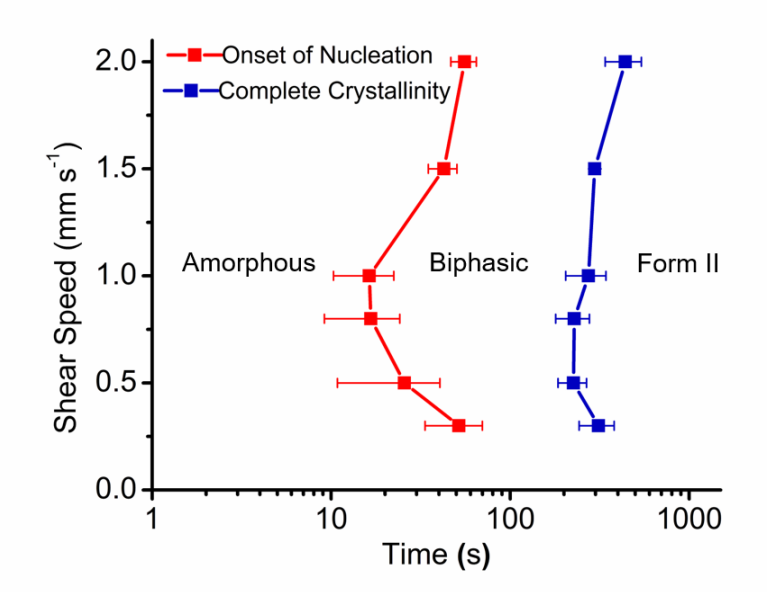

Figure 2.5 Transformation diagram showing how blade speed relates to the time scale of nucleation and overall crystallization for acetaminophen thin films created at 90 °C.

2.5 Conclusion

The solution shearing technique is a simple and straightforward method to obtain the amorphous phase of APIs, which is of interest because amorphous phases have rapid dissolution dynamics. Further, this technique has utility in obtaining the amorphous phase at elevated temperatures. Normally, the amorphous phase is highly prone to undergoing transformations and is typically controlled using careful temperature control, humidity control, or inclusion of materials (like polymers) that inhibit crystallinity.[37,38]

Understanding and controlling solid state phase transformations can be utilized to study the balance between molecular mobility, nucleation and growth, as well as study the relative phase stability. The transformation diagrams obtained through solution shearing can also provide insight about the crystallization kinetics, similar to how a time temperature transformation diagram is used for undercooled melt systems.[39]

Solution shearing is an effective tool to sample processing conditions rapidly while utilizing a small amount of material, and is a robust method to isolate equilibrium and metastable polymorphs, as demonstrated in organic semiconductors.[21] This work broadens the relevance of solution shearing to include pharmaceuticals. In this study, we show that controlling the coating speed and temperature allows us to obtain polymorphic phases in glycine and acetaminophen with metastable polymorphs being present in the thinnest films. We hypothesize that confinement is responsible for stabilization of metastable polymorphs. Previous studies have demonstrated that shearing induces polymorphism due to one-dimensional confinement.[23] The observed solid-state phase formation of a molecule using solution shearing is highly dependent on the molecular structure, but solution shearing is capable of isolating the amorphous phase in multiple candidate APIs, even those exhibiting low aqueous solubility, such as carbamazepine. Moving forward, solution shearing can be adopted as a method to aid in polymorph screening and selection during drug development, with the processing diagrams provided as a starting point to obtain metastable polymorphs.

2.6 Chapter 2 Appendix

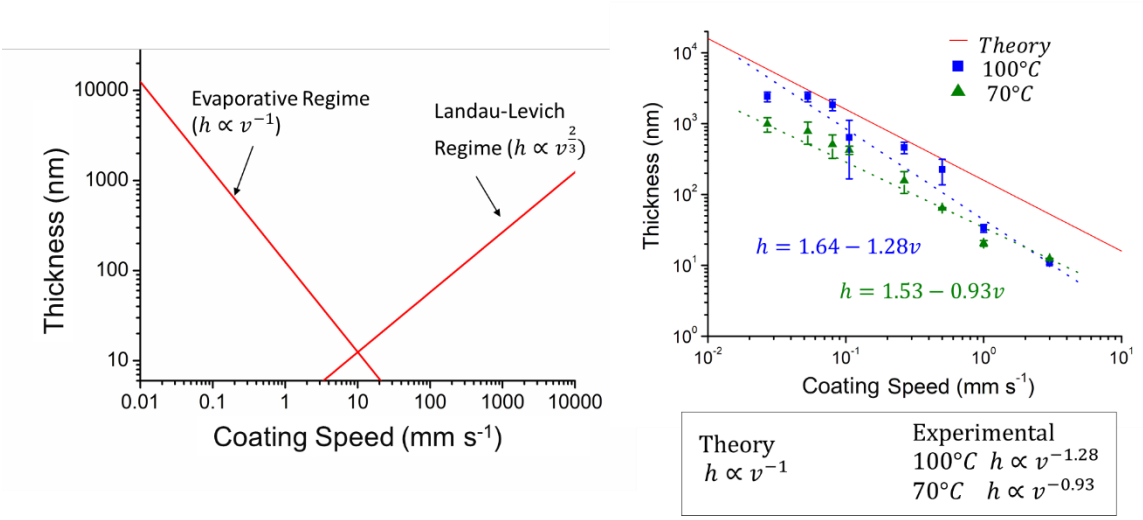

Figure A2.2 The coating speed is significant for dictating final film thickness. The log-log transformed data show the inverse linear relationship between shearing speed and film thickness for films created at 90 °C.

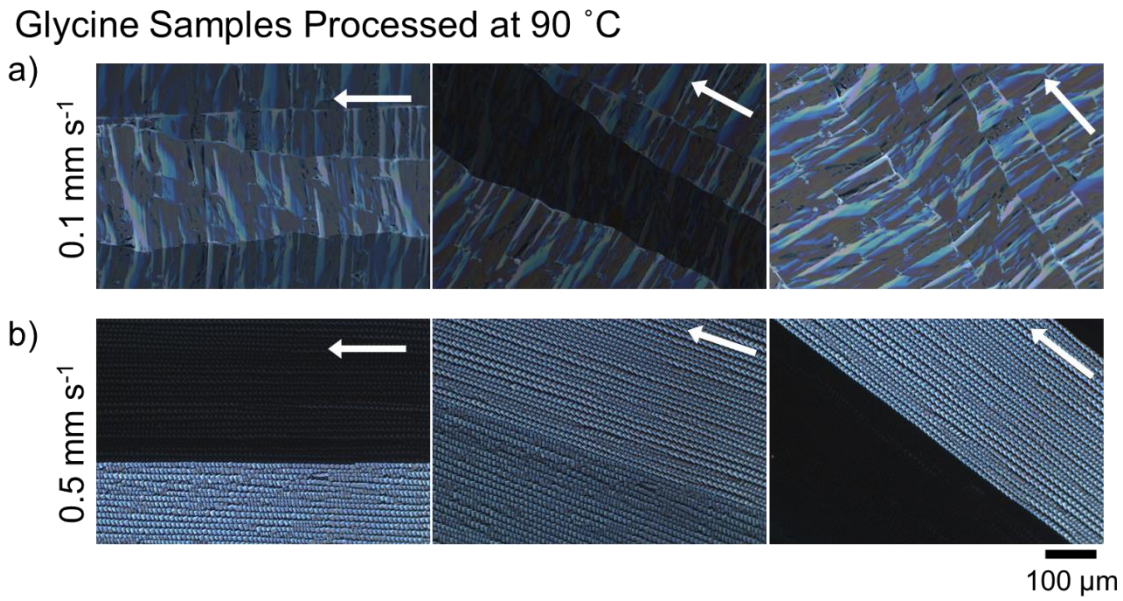

Figure A2.3 Glycine thin films with a) wide crystals and b) needle like crystals. Both crystal morphologies are aligned in the direction of coating in the film. Films coated at 90 °C. Scale bar is 100 µm. Arrow indicates direction of coating as samples are rotated under polarizers to show crystal domains with similar alignment.

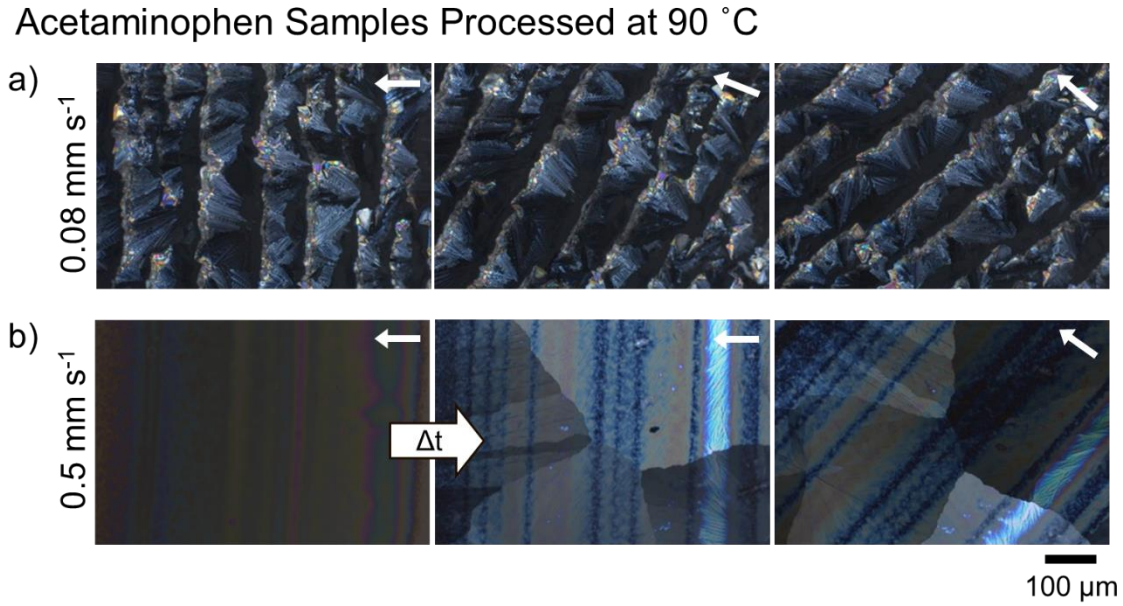

Figure A2.4 Acetaminophen thin films with a) stick slip fluid flow creating non-uniform regions of thick and thin crystals and b) a smooth amorphous film transforms to spherulitic crystals over time.

Degree of polarization measurement and calculation

The degree of polarization is a measure of the ability for a thin film to redirect a beam of light. If a film is highly aligned, it will be able to polarize the incident light. Therefore, the thin film could produce a high intensity signal of light in one orientation and a weak signal in another. The degree of polarization is a measure of this ability to modulate the light intensity depending on the film orientation. A more aligned film will have a greater influence on the ability to redirect light (leading to high contrast between the maximum and minimum observed polarization intensity) while a disordered or isotropic film has less ability to control and direct the light.[40,41]

As the sample is rotated under a polarizer (as shown in **Figure A2.4**), the average intensity (I) for the image is measured using ImageJ's "measure" function. For a given film, the orientation and image with I_{max} and I_{min} are recorded for use in this calculation of the DOP:

$$Degree\ of\ Polarization = \frac{I_{max} - I_{\min}}{I_{max} + I_{min}}$$

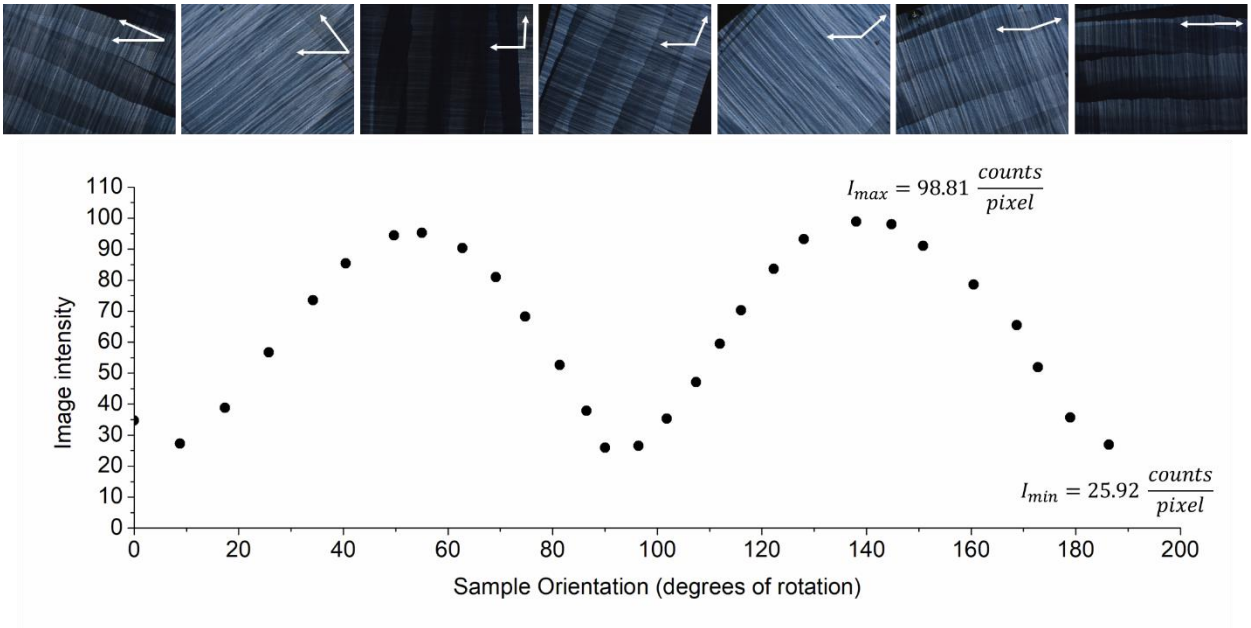

Figure A2.5 Optical images demonstrate the orientation of the thin film relative to a reference direction (left is referenced as 0 degrees of rotation). As the films are rotated under the linearly cross polarized light, the average film intensity changes. The maximum and minimum intensity (arbitrary units) is recorded to calculate the degree of polarization.

An example of this calculation for a solution sheared sample created at 90°C and 0.5 mm s^{-1} is shown for the case described in **Figure A2.4**.

$$DOP = \frac{I_{max} - I_{\min}}{I_{max} + I_{min}} = \frac{98.81 - 25.92}{98.81 + 25.92} = 0.58$$

Taking into account exposure time during image acquisition, the coating speed has a significant impact on the image intensity vs substrate rotation plot (**Figure A2.5**). The slow coating speed has higher intensity per ms of exposure, and has a periodic trend with higher amplitude (DOP approaches 1). The faster coating speed, has much smaller varition in image intensity and a low amplitude (DOP approaches 0).

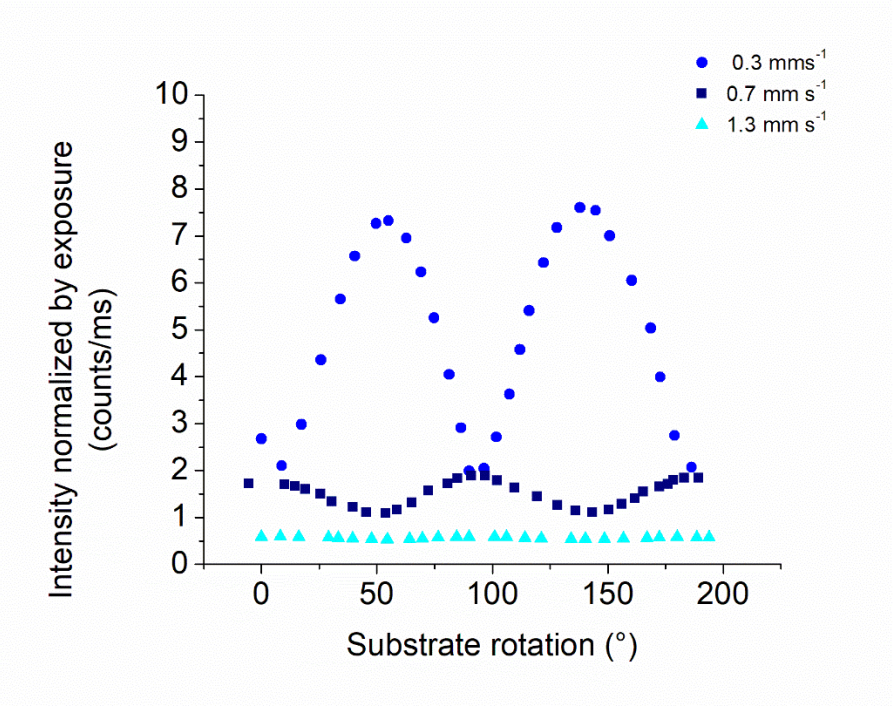

Figure A2.6 Image intensity counts normalized by exposure demonstrates the separation in the rotation curves for determining degree of polarization in aligned film samples. Slower shearing speeds correlate with higher amplitude and vertical shift on the intensity axis while faster shearing speed curves have low amplitude and are shifted towards y=0.

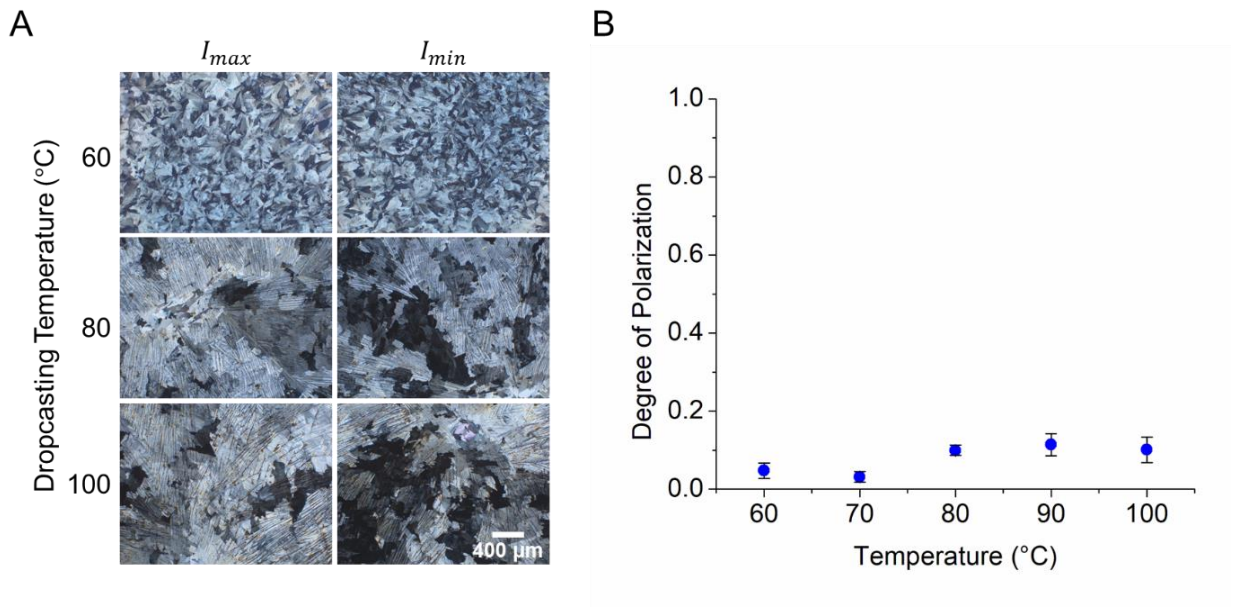

Figure A2.7 a) Polarized optical microscopy images of dropcast thin films at 60, 80, and 100 °C. As films are rotated under the polarizer, the orientations with maximum and minimum overall image intensity are shown. The scale bar is 400 µm for all images. b) The degree of polarization for dropcast films is low for all conditions, with higher temperatures having slightly higher DOP. The y-axis ranges from 0 - 1 to reflect the upper and lower bound of the DOP.

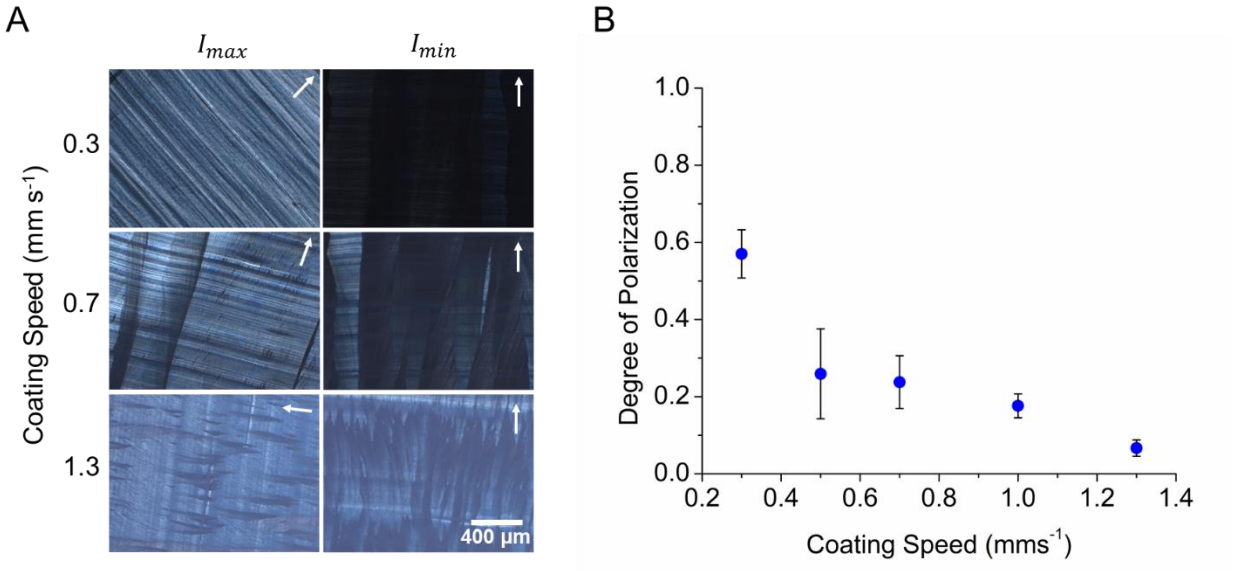

Figure A2.8 a) Polarized optical microscopy images of thin films created at 90 °C and 0.3, 0.7, and 1.3 mm s^{-1}. As the coating speed is increased, the films exhibit less redirection of the cross-polarized incident light. The slow coating speed produces films where I_{max} and I_{min} are drastically different. Scale bar is 400 µm and is the same for each image. Arrows demonstrate the shearing direction. b) The degree of polarization shows a dependence on shearing speed, with fast coating speeds having lower DOP.

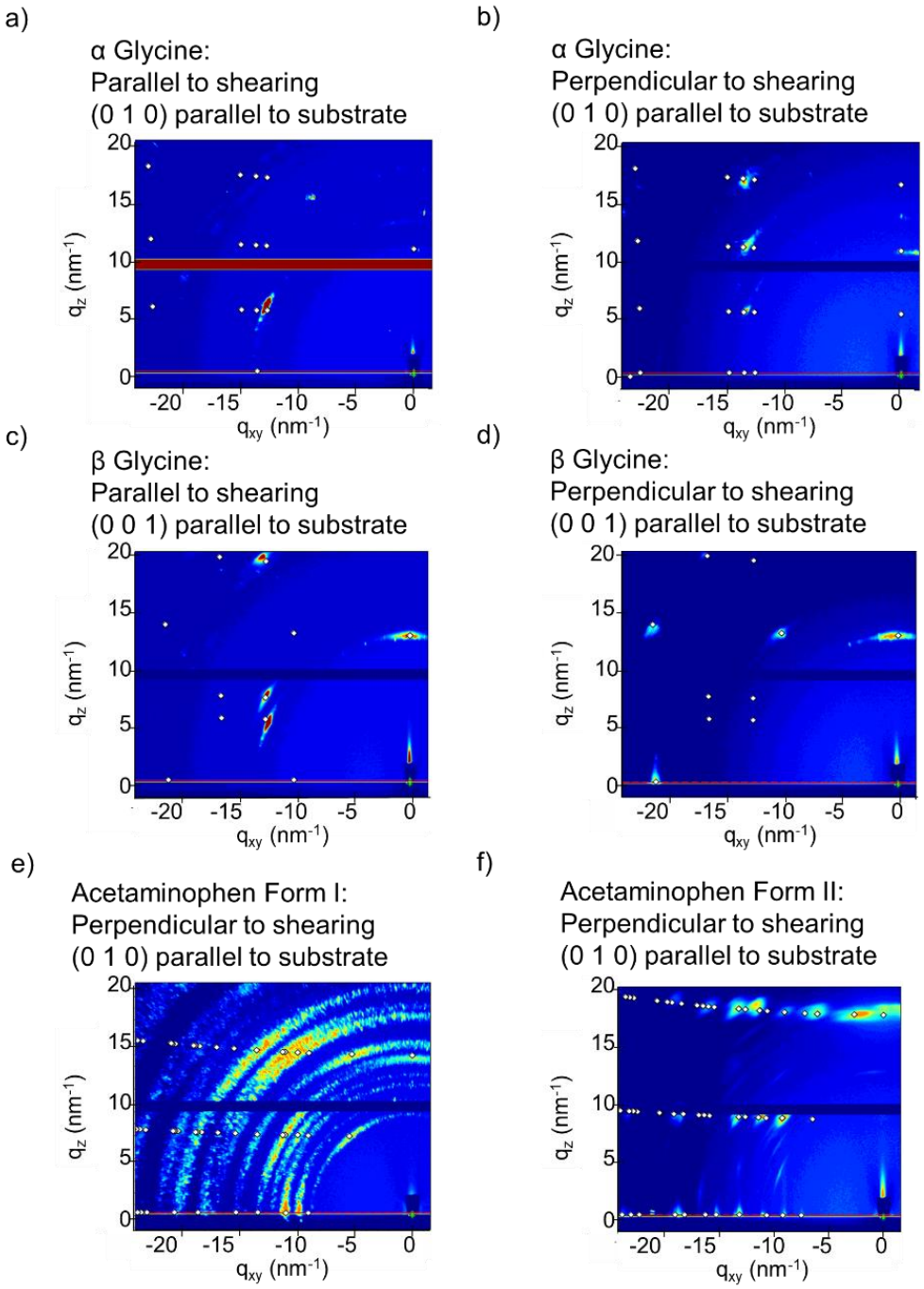

Figure A2.9 2D grazing incidence X-ray diffraction images, with peak indexing to determine crystal orientation and confirm polymorphic identity. α glycine (a, b) exhibits (010) orientation while β glycine (c, d) shows (001) orientation. Glycine films are measured parallel and perpendicular to the coating direction to collect sufficient diffraction to characterize polymorphism. Acetaminophen films are isotropic and are crystallized as e) form I with (010) orientation and f) form II with (010) orientation.

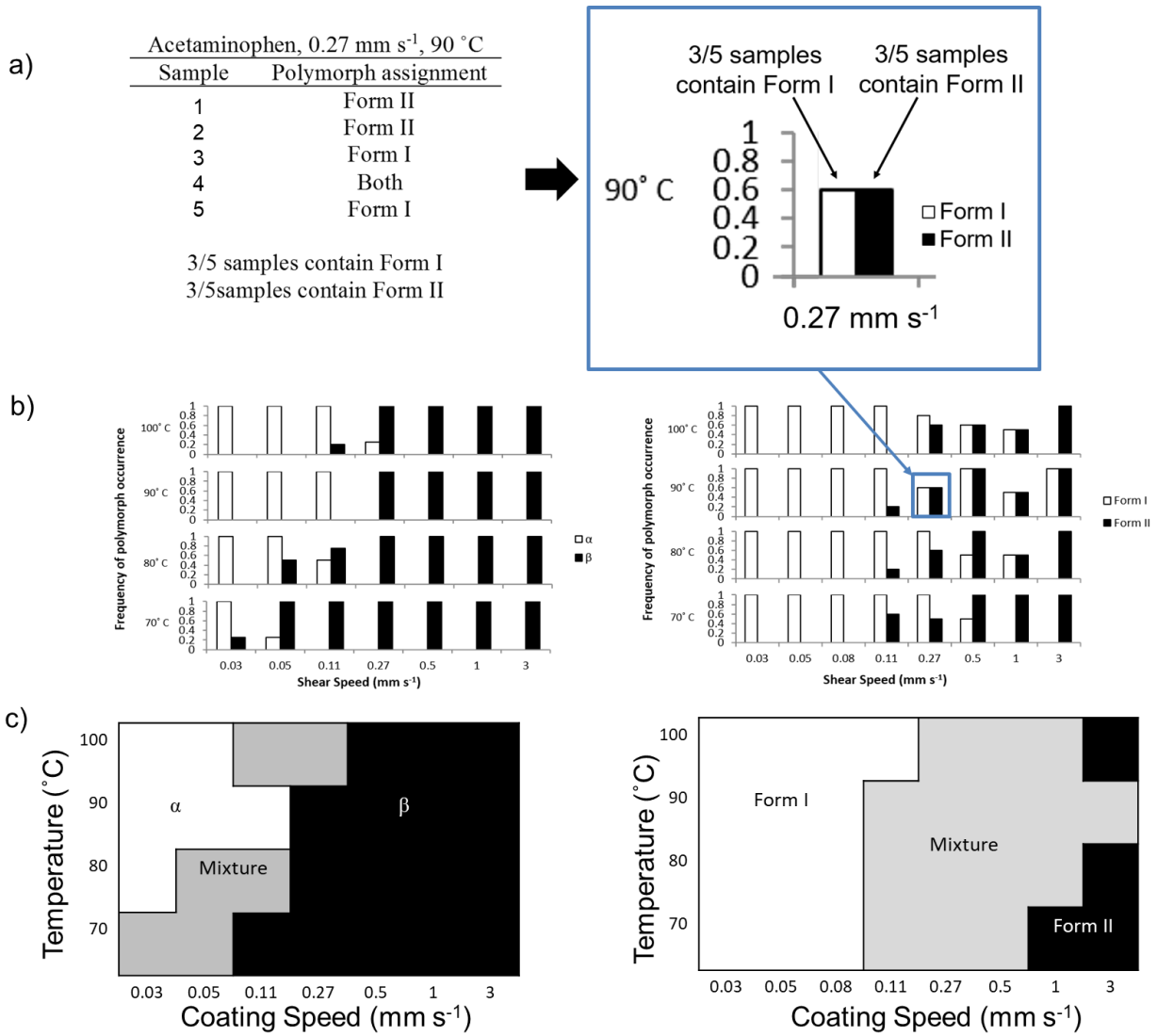

Figure A2.10 a) Multiple samples fabricated at each processing condition were assessed for polymorphic identity. Bar graphs present the relative proportion of each polymorph isolated at each processing condition. b) bar graphs arranged by coating speed and temperature show polymorphic phase purity can be achieved by selecting processing conditions. c) a simplified diagram, presenting the same information from subfigure b, for ease of visualization of phase purity.

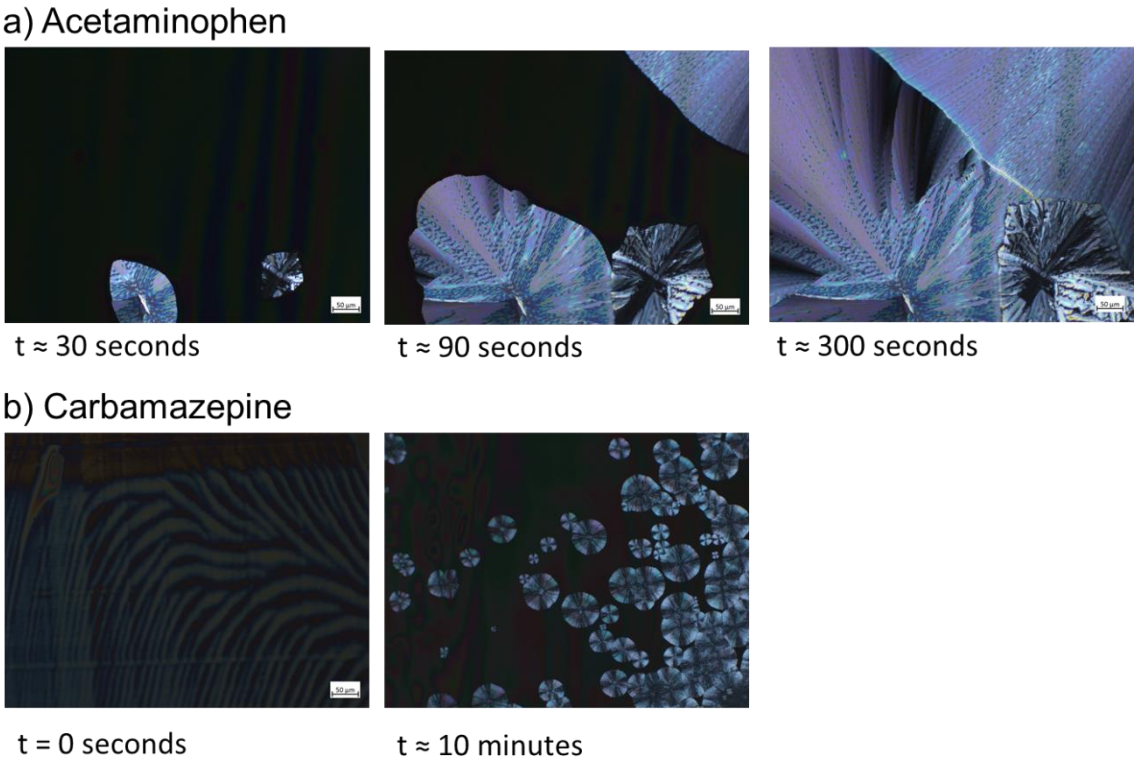

Figure A2.11 a) acetaminophen and b) carbamazepine amorphous phase transforms to a crystalline phase composed of spherulitic crystals.

2.7 References

1. Parks, C. *et al.* Nanocrystal dissolution kinetics and solubility increase prediction from molecular dynamics: The case of α-, β-, and γ-glycine. *Mol. Pharm.* **14**, 1023–1032 (2017).

2. Byrn, S. R., Pfeiffer, R. R., Stephenson, G., Grant, D. J. W. & Gleason, W. B. Solid-State Pharmaceutical Chemistry. *Chem. Mater.* **6**, 1148–1158 (1994).

3. Brittain, H. G., Grant, D. J. R. & Myrdal, P. B. Effects of polymorphism and solid-state solvation on solubility and dissolution rate. in *Polymorphism in Pharmaceutical Solids: Second Edition* (2016).

4. Dwyer, L., Kulkarni, S., Ruelas, L. & Myerson, A. Two-stage crystallizer design for high loading of poorly water-soluble pharmaceuticals in porous silica matrices. *Crystals* **7**, 131 (2017).

5. Kalepu, S. & Nekkanti, V. Insoluble drug delivery strategies: Review of recent advances and business prospects. *Acta Pharm. Sin. B* **5**, 442–453 (2015).

6. Fahr, A. & Liu, X. Drug delivery strategies for poorly water-soluble drugs. *Expert Opin. Drug Deliv.* **4**, 403–416 (2007).

7. Hilfiker, R., Blatter, F. & Raumer, M. von. Relevance of Solid-state Properties for Pharmaceutical Products. in *Polymorphism: in the Pharmaceutical Industry* (2006). doi:10.1002/3527607889.ch1.

8. Newman, A. W. & Byrn, S. R. Solid-state analysis of the active pharmaceutical ingredient in drug products. *Drug Discov. Today* **8**, 898–905 (2003).

9. Hilfiker, R., De Paul, S. M. & Szelagiewicz, M. Approaches to Polymorphism Screening. in *Polymorphism* 287–308 (2006). doi:doi:10.1002/3527607889.ch11.

10. Childs, S. L. *et al.* A metastable polymorph of metformin hydrochloride: Isolation and characterization using capillary crystallization and thermal microscopy techniques. *Cryst. Growth Des.* **4**, 441–449 (2004).

11. Price, S. L. The computational prediction of pharmaceutical crystal structures and polymorphism. *Adv. Drug Deliv. Rev.* (2004) doi:10.1016/j.addr.2003.10.006.

12. Lee, E. H. A practical guide to pharmaceutical polymorph screening & selection. *Asian J. Pharm. Sci.* **9**, 163–175 (2014).

13. Leon, R. A. L. *et al.* Highly Selective, Kinetically Driven Polymorphic Selection in Microfluidic Emulsion-Based Crystallization and Formulation. *Cryst. Growth Des.* **15**, 212–218 (2015).

14. Ehmann, H. M. A. & Werzer, O. Surface mediated structures: Stabilization of metastable polymorphs on the example of paracetamol. *Cryst. Growth Des.* **14**, 3680–3694 (2014).

15. Jiang, Q. & Ward, M. D. Crystallization under nanoscale confinement. *Chem. Soc. Rev.*

43, 2066–79 (2014).

16. Hamilton, B. D., Hillmyer, M. A. & Ward, M. D. Glycine polymorphism in nanoscale crystallization chambers. *Cryst. Growth Des.* **8**, 3368–3375 (2008).

17. Buanz, A. B. M. & Gaisford, S. Formation of Highly Metastable β Glycine by Confinement in Inkjet Printed Droplets. *Cryst. Growth Des.* **17**, 1245–1250 (2017).

18. Trauffer, D. I., Maassel, A. K. & Snyder, R. C. Non-Needle-like Morphology of β-Glycine Particles Formed from Water Solutions via Monodisperse Droplet Evaporation. *Cryst. Growth Des.* **16**, 1917–1922 (2016).

19. Lee, S., Feldman, J. & Lee, S. S. Nanoconfined Crystallization of MAPbI3 to Probe Crystal Evolution and Stability. *Cryst. Growth Des.* **16**, 4744–4751 (2016).

20. Becerril, H. A., Roberts, M. E., Liu, Z., Locklin, J. & Bao, Z. High-Performance Organic Thin-Film Transistors through Solution-Sheared Deposition of Small-Molecule Organic Semiconductors. *Adv. Mater.* **20**, 2588–2594 (2008).

21. Giri, G. *et al.* Tuning charge transport in solution-sheared organic semiconductors using lattice strain. *Nature* **480**, 504 (2011).

22. Gu, X. *et al.* Roll-to-Roll Printed Large-Area All-Polymer Solar Cells with 5% Efficiency Based on a Low Crystallinity Conjugated Polymer Blend. *Adv. Energy Mater.* **7**, 1602742 (2017).

23. Giri, G. *et al.* One-dimensional self-confinement promotes polymorph selection in large-area organic semiconductor thin films. *Nat. Commun.* **5**, 3573 (2014).

24. Pilling, S. *et al.* The influence of crystallinity degree on the glycine decomposition induced by 1 MeV proton bombardment in space analog conditions. *Astrobiology* **13**, 79–91 (2013).

25. Zimmermann, B. & Baranović, G. Thermal analysis of paracetamol polymorphs by FT-IR spectroscopies. *J. Pharm. Biomed. Anal.* **54**, 295–302 (2011).

26. Smilgies, D. M. & Blasini, D. R. Indexation scheme for oriented molecular thin films studied with grazing-incidence reciprocal-space mapping. *J. Appl. Crystallogr.* **40**, 716–718 (2007).

27. Hammersley, A. P. FIT2D: A multi-purpose data reduction, analysis and visualization program. *J. Appl. Crystallogr.* **49**, 646–652 (2016).

28. Iitaka, Y. The crystal structure of β-glycine. *Acta Crystallogr.* **13**, 35–45 (1960).

29. Marsh, R. E. A refinement of the crystal structure of glycine. *Acta Crystallogr.* **11**, 654–663 (1958).

30. Haisa, M., Kashino, S., Kawai, R. & Maeda, H. The Monoclinic Form of p-Hydroxyacetanilide. *Acta Crystallogr. Sect. B Struct. Crystallogr. Cryst. Chem.* **B32**, 1283–1285 (1976).

31. Thomas, L. H., Wales, C., Zhao, L. & Wilson, C. C. Paracetamol form II: An elusive polymorph through facile multicomponent crystallization routes. *Cryst. Growth Des.* **11**, 1450–1452 (2011).

32. Le Berre, M., Chen, Y. & Baigl, D. From convective assembly to Landau - Levich deposition of multilayered phospholipid films of controlled thickness. *Langmuir* **25**, 2554–2557 (2009).

33. Aranson, I. S., Tsimring, L. S. & Vinokur, V. M. Stick-slip friction and nucleation dynamics of ultrathin liquid films. *Phys. Rev. B - Condens. Matter Mater. Phys.* **65**, 125402 (2002).

34. Goh, L. *et al.* A stochastic model for nucleation kinetics determination in droplet-based microfluidic systems. *Cryst. Growth Des.* **10**, 2515–2521 (2010).

35. Peterson, M. L. *et al.* Crystallization and transformation of acetaminophen trihydrate. *Cryst. Growth Des.* **3**, 761–765 (2003).

36. Dawson, A. *et al.* Effect of high pressure on the crystal structures of polymorphs of glycine. *Cryst. Growth Des.* **5**, 1415–1427 (2005).

37. Yu, L. Amorphous pharmaceutical solids: Preparation, characterization and stabilization. *Adv. Drug Deliv. Rev.* **48**, 27–42 (2001).

38. Zhao, Y. *et al.* Melt-Processing of Complementary Semiconducting Polymer Blends for High Performance Organic Transistors. *Adv. Mater.* **29**, 1605056 (2017).

39. Yu, L. *et al.* Isothermal Crystallization Kinetics and Time-Temperature-Transformation of the Conjugated Polymer: Poly(3-(2′-ethyl)hexylthiophene). *Chem. Mater.* **29**, 5654–5662 (2017).

40. Ye, L. *et al.* The controllable intensity and polarization degree of random laser from sheared dye-doped polymer-dispersed liquid crystal. *Nanophotonics* **7**, 473–478 (2017).

41. Bi, Z. F., Yang, M. & Shang, G. Y. Optical polarization response at gold nanosheet edges probed by scanning near-field optical microscopy. *Chinese Phys. B* **27**, 087801 (2018).

Chapter 3. In situ grazing incidence X-ray diffraction to obtain spatial and temporal resolution of β glycine crystal structures formation

3.1 Abstract

Meniscus guided coating (MGC) is a class of techniques that has previously shown the ability to isolate new crystal structures and morphologies in pi-pi stacking small organic molecules, such as TIPS pentacene. In this work, we explore the application of MGC for a small molecule, glycine, where the crystal structure is directed by hydrogen bonding; we hypothesized that it could be possible to isolate new crystal structures or morphologies for this material as well. Grazing incidence wide angle X-ray diffraction (GIXD) was used to probe the crystal structures of glycine in thin films created using MGC. Using ex situ characterization, we observed the tendency for the (021) plane to have variable d-spacing by observing the Bragg peak location. However, we were unable to directly correlate processing conditions to an observed change in crystal structure. We turned to in situ GIXD to observe crystallization directly during the coating process. Through this we observed three Bragg peaks occurring near the (021) Bragg peak position. Through peak indexing with different crystallographic orientations, we found that the (100) and (001) crystal planes are both present within the samples. These two orientations can account for two of the Bragg peaks near the (021) plane. Therefore, the peaks could be associated with different crystal orientations or metastable crystal structures.

3.2 Introduction

During manufacturing, the processing conditions can impact the material structural properties and performance.[1,2] Recently, meniscus guided coating has been identified as a processing technique that can change lattice spacing and improve charge transport in organic semiconductors (OSCs).[3] This has motivated numerous structural studies of polymorphism in pi-

This work is in preparation for publication:

Stephanie Guthrie, Deflef-M Smilgies, Gaurav Giri. In situ grazing incidence X-ray diffraction to obtain spatial and temporal resolution of β glycine crystal structures formation (*in preparation*).

pi stacking systems, which show that small changes in lattice structure can occur in conjugated polymer and small molecule systems as a result of changing processing conditions.[4,5]

6,13-Bis(triisopropylsilylethynyl)pentacene (TIPS-pentacene) is a pi-pi stacking OSC, that exhibits changes in polymorphism in response to processing conditions.[6] TIPS-pentacene polymorphs have only a small shift in lattice parameters or angle, while preserving the general crystal structure.[7] This work has shown that potential energy metabasins or multi-minima exist for these systems, and that MGC is a processing technique that provides access to different, yet similar, solid phases, kinetically trapping metastable polymorphs in these metabasins.[7,8]

The concept of multiple energetic minima of solid phases of small molecules has been explored using computational approaches for diverse systems, including crystals stabilized through pi-pi stacking and hydrogen bonding interactions.[9] Computational work by Dybeck et al. has demonstrated that energetically, there are many polymorphic structures that could be present, even though few of them are observed experimentally.[9] During crystallization, different polymorphic outcomes are related to unique intermolecular interactions that occur during molecular rearrangements.[10] Therefore, it is of interest to extend our understanding of structure-processing relationships during MGC to include materials with hydrogen bonding motifs, and to see whether metastable polymorphs can be stabilized for glycine using MGC.

Recently, meniscus guided coating has been used to create thin films of small molecules relevant for pharmaceutical applications, including glycine, acetaminophen, ellipticine, and aspirin.[11,12] Many pharmaceutical molecules have chemical motifs where pi-pi stacking (if present) often occurs alongside hydrogen bonding forces.[13] In crystals of these molecules, the polymorphism that is observed due to MGC process is different compared to OSCs. While pi-pi stacking OSCs show small lattice changes are slightly different from the same parent crystal structure, hydrogen bonding small molecules have shown polymorphism with drastically different crystal structures. For example, acetaminophen polymorphs can be stabilized as monoclinic and orthorhombic structures.[11] Ellipticine also showed monoclinic and orthorhombic structures.[12] For

glycine, two polymorphs (α and β) forms were isolated.[11] Each of these examples have drastically different lattice parameters and unit cells. In these hydrogen bonding systems, we have not yet observed polymorphs that seem to originate from the same parent structure with slight changes in lattice parameters as in the OSC, TIPS- pentacene. There is a need for improved understanding of how molecular packing changes and crystallization occurs during MGC for hydrogen bonding systems.

State of the art X-ray diffraction techniques have enabled enhanced understanding of crystallization mechanisms. Specifically, in situ grazing incidence wide angle x-ray diffraction (in situ GIWAXD) has proved to be instrumental for probing dynamic processes, such as MGC, as it allows for direct observation of 1) relative timescales of solvent evaporation and crystallization, 2) the formation of intermediate structures 3) processing stability of intermediate structures. This provides a venue to develop mechanisms that describe crystallization pathways and describe the assembly of thin films.

Previously, in situ GIWAXD methods were developed at the Cornell High Energy Synchrotron Source (CHESS) by Smilgies et al, where precise optics provided a beam size of 15 μm and data collection reached 100 frames/s to probe thin film formation during MGC.[14] Giri et al. first applied the in situ technique to determine that the one-dimensional self-confinement is responsible for TIPS-pentacene polymorph selection during MGC.[6] In subsequent studies, in situ GIWAXD has been to probe the formation of diverse material systems. Sanchez-Botero et al. investigated coating of cellulose nanocrystal suspensions and determined a mechanism to describe ordering.[15] Zhong et al. studied lead-halide perovskites and found that coating conditions change crystallization pathways, and that intermediate solvate formation can be circumvented to improve solar cell efficiency.[16] While photovoltaic processing and performance has been improved due to understanding crystallization mechanisms, the pharmaceutical industry has not yet harnessed and applied the same understanding.

The United States Food and Drug Administration has identified that the pharmaceutical industry faces significant challenges with efficiency during drug development.[17] The concept of quality by design (QbD) has been introduced to encourage pharmaceutical companies to improve their processing approaches, to develop scalable manufacturing techniques, and to monitor processes in real time for improved process analytics.[18] We suggest that MGC techniques, like MGC, can be used as a versatile platform for efficient crystallization and polymorph selection in pharmaceuticals, because it has proved to be a scalable and effective processing technique in other fields.[19] In situ GIWAXD and other real-time process monitoring tools can improve process efficiency by revealing mechanisms of crystallization, allowing for enhanced understanding of structure-processing relationships in the pharmaceutical industry, and moving away from trial and error approaches.[1]

This study presents the application of the in situ GIWAXD technique to study crystallization in a hydrogen bonding small molecule, glycine. Ex situ crystal structure analysis shows that the β polymorph of glycine can be isolated using MGC. Further analysis suggests that in addition to Bragg peaks occurring in the expected positions, occasionally the Bragg peaks exhibited a shift in reciprocal space position. Ex situ measurements do not provide a clear understanding of the relationship between the observed Brag peaks and processing conditions. Using in situ GIWAXD to observe the film coating process in real time provides insight to the formation of multiple Bragg peaks. We hypothesize that the Bragg peaks could be associated with different crystallographic orientations of glycine or metastable crystal structures in the thin film. These new structures form at different times in the coating process. Changing the X-ray incidence angle provides spatial information, that the one orientation or structure predominantly crystallizes on the surface of the film while the other orientation or crystal structure is more likely to be present near the silicon substrate.

3.3 Materials and Methods

Grazing incidence X-ray Diffraction

Grazing incidence wide angle X-ray diffraction was performed at D-1 beamline at Cornell High Energy Synchrotron Source (CHESS) using monochromatic radiation with a wavelength of 1.162 Å. A Pilatus 200k 2D area detector (Dectris) with a pixel size of 172 µm x 172 µm was placed 180 mm from the sample. The incident angle of the X-ray beam was set to 0.15°, an angle that allows for the X-ray to sample the full thin film during coating. The X-ray beam was focused to approximately 15 µm, as previously described for the in situ coating process.[14]

Time-resolved data (in situ) was collected during glycine thin film coating. As coating speeds varied, data collection parameters were adjusted to capture kinetics. For a coating speed of 0.05 mm/s, collection rate was 2.5 frames per second. For a coating speed of 0.5 mm/s, collection rate was 50 frames per second.

Ex situ characterization was also carried out after the coating process. The incident X-ray angle was varied between 0.03 - 0.21° to look at spatial depth changes in film structure.

X-ray analysis

Analysis was performed using GIXSGUI in MATLAB (MathWorks, Natick, MA), including conversion of 2D maps to 1D profiles using the linecut feature. Bragg peak locations in reciprocal space were identified using the peak finder function in GIXSGUI, with a manually selected region of interest.[20] Bragg peak position (q) for specific crystal planes (hkl) was correlated to interplanar spacing (d) through the relationship $q_{hkl} = \frac{2*\pi}{d_{hkl}}$.

3.4 Results and Discussion

MGC was used to fabricate thin films of glycine with varied coating speed and temperature. This technique was previously applied extensively in TIPS-pentacene to identify new crystal structures for the molecule.[3] We hypothesized that MGC could provide a platform for the isolation of new glycine polymorphs. We previously discussed the ability to isolate α and β polymorphs.[11] In this work, we aim to investigate how the MGC process contributed to changes in the crystal

structure of β glycine. Grazing incidence X-ray diffraction was utilized, with a 2D area detector to visualize the diffraction. For the samples measured, the observed Bragg peaks positions were determined using GIXSGUI. The data was aggregated and the peak positions were re-plotted to characterize the distribution of peak positions obtained. In **Figure 3.1**, we show the resulting peak positions from three separate beamtime data collections at two synchrotrons (CHESS and SLAC). Relevant to this discussion, the 0L1 and 02L peaks are annotated on the figure. Notably, the (021) peak show broad distributions of peak positions relative to other peaks. With grazing incidence X-ray geometry, peak shifts can occur in the radial coordinate (q_{xyz}) or along the polar angle coordinate (θ). A shift in the polar angle coordinate could indicate texture or misorientation of crystals on the substrate. A radial shift (to larger or smaller q_{xyz}), however is an indication that the crystal structure is different (retraction or expansion of the particular crystal plane). We assessed the radial peak shift for the (021) plane in ex situ samples.

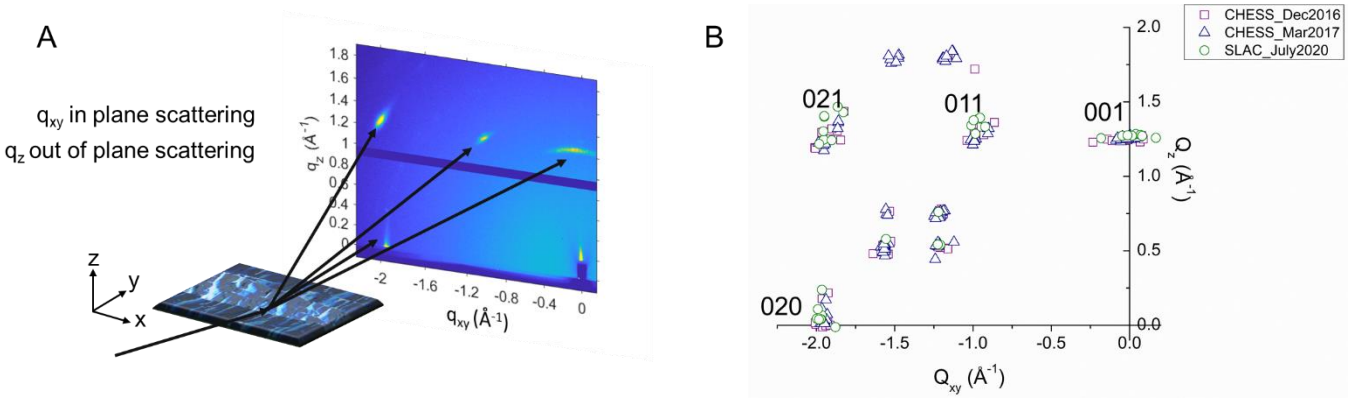

Figure 3.1 a) Sample and grazing incidence X-ray diffraction geometry. b) Peak center positions were determined for individual samples and replotted on the same diagram to visualize peak spread. The (021) peak appears to have appreciable variation in peak position.

Table 3.1: Simulated peak position and experimental peak positions for the (021), (001) and (020) crystal planes (n=25). Experimentally, the average peak position is consistent with the calculated, expected position.

	$q_{(021)}$ ($Å^{-1}$)	$q_{(001)}$ ($Å^{-1}$)	$q_{(020)}$ ($Å^{-1}$)
Simulated position (GLYCIN, CCDC 1169352)	2.37	1.27	2.01
Experimental position (standard deviation) n = 25	2.37 (0.04)	1.27 (0.01)	1.99 (0.03)

We characterized the average position of the (021) peaks and found the average to occur at q = 2.37 ± 0.04 $Å^{-1}$, (n = 25). This matches the expected position of the (021) peak (2.37 $Å^{-1}$) according to data from literature reported single crystal X-ray analysis (**Table 3.1**).[21] However there were occasional samples with peak positions that fall outside the error. The maximum $q_{(021)}$ position was found to be q =2.45 $Å^{-1}$ and the minimum position was centered at q = 2.28 $Å^{-1}$, which are nontrivial shifts from the expected peak location, as they are more than one standard deviation from the mean. We hypothesize that these outliers could be explained by multiple phenomena: 1) they may be Bragg peaks associated with different crystal planes in β glycine or 2) they may be Bragg peaks associated with new crystal lattice arrangements that expand or retract the (021) plane.

The (021) plane is a convolution of the (020) and (001) planes. Therefore, by studying the (001) and (020) Bragg peak positions, we aimed to gain insight about which planes contribute to the spread in the (021) peaks. From experimental samples, the average position of the (001) peak was centered at 1.27 ± 0.01 $Å^{-1}$ (expected position 1.27 $Å^{-1}$), matching the expected position. The (020) peak was centered at 1.99 ± 0.03 $Å^{-1}$ (expected position 2.01 $Å^{-1}$); the expected peak position. The (020) peak has more spread compared to the (001) peak, indicated by the deviation from the mean, and therefore could contribute more to the spread in the (021) peaks. However this is not conclusive regarding the cause of the spread in (021) peaks.

Ex situ analysis is limited in providing mechanistic understanding of how the MGC process contributes to peak spread. We were unable to correlate coating speed or temperature directly to a shift in peak position for the (021) plane. In a more focused experimeent, we varied coating speed at two levels (low = 0.03 mm/s, high = 1.3 mm/s) while holding the temperature constant. This strategy was employed by Giri et al to create strained TIPS-pentacene lattices, where the coating speed was correlated to a change in Bragg peak position.[3] In this work, after determining the Bragg peak location for the (001), (020) and (021) planes, we were unable to conclude that

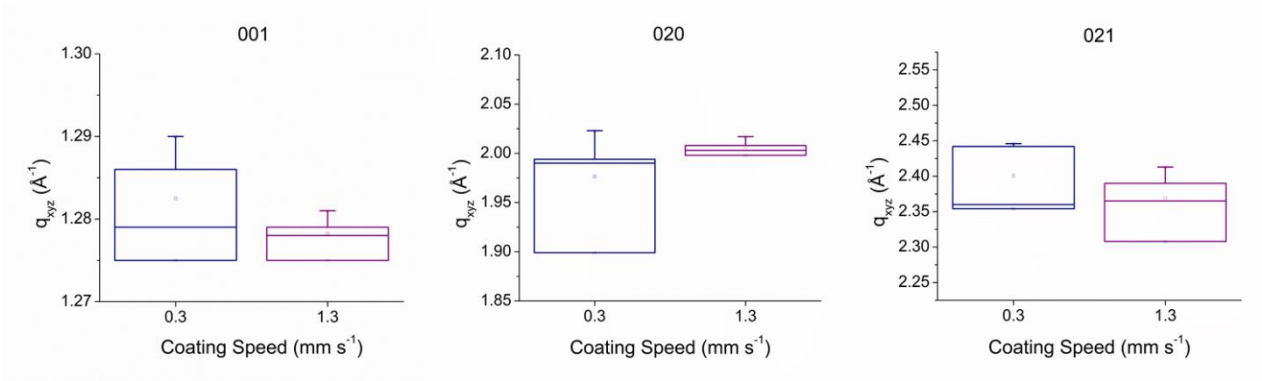

Figure 3.2 Experimental peak positions ((001), (020), (021) planes) for a 90 °C coating temperature, and speeds of 0.3 (n=4) and 1.3 mm s^{-1} (n=4).

coating speed alone is a predictor of peak position (**Figure 3.2**). The full data for the (020), (001) and (021) peak positions is listed in **Table A3.1.**

Ex situ synchrotron-based work reveals that there are variations in Bragg peak positions for β glycine. However, we cannot obtain conclusive information regarding how the variation in peak positions occurs, and if it is a function of data collection error, a true underlying phenomenon of small lattice shifts, or due to a factor like crystal orientation. Glycine is highly soluble in water, and further, β glycine is prone to changing forms in ambient conditions. We observed morphological changes reminiscent of crystal reorientation in the films within days of storage in ambient conditions. It is possible that we could not determine precise relationships between processing conditions and crystal structure change due to the changes occurring at ambient conditions prior to the ex situ sample measurement. Films which were originally highly aligned

exhibited loss of alignment and the formation of misoriented patches (**Figure 3.3**). This optical observation of thin film change could be accompanied by a change in crystal structure, thin film

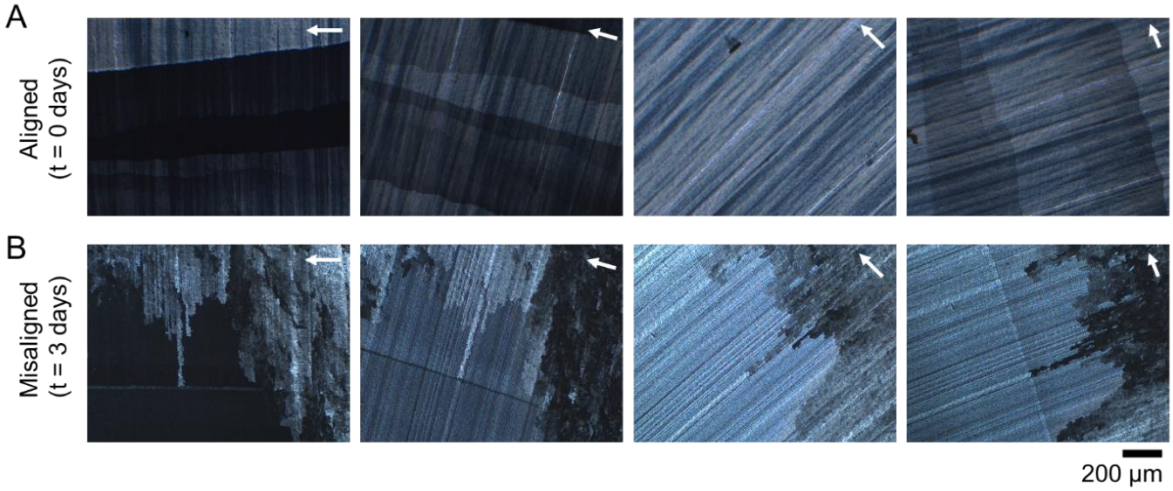

Figure 3.3 Polarized optical microscopy images of thin films prepared at 90°C and 0.3 mm s^{-1} a) imaged immediately after fabrication and b) imaged 3 days after fabrication. Arrows show direction of coating and rotation of sample polarizers. Scale bar is 200 µm for all images.

texture and morphology, impacting X-ray diffraction measurements.

Therefore, it was of interest to gain a deeper understanding of crystallization occurring during the thin film coating process. Measuring diffraction during the film coating process can directly observe structural formation and evolution of Bragg peaks. We utilized the D1 beamline at CHESS to perform in situ grazing incidence wide angle X-ray diffraction (in situ GIXD) during the MGC process. **Figure 3.4** provides a schematic of the process and data collection. As the coating blade translates across the substrate, material is deposited from the fluid meniscus. Initially, the X-ray beam is blocked from the detector (**Figure 3.4a**) and there is no detected signal because the coating is occurring upstream from the X-ray beam (**Figure 3.4d, 3.4g**). As the blade continues to move, eventually the meniscus region is aligned with the X-ray, where solvent evaporation is actively occurring (**Figure 3.4b**) producing a broad ring of diffuse scattering associated with the solvent (**Figure 3.4e, 3.4h**). Finally, the fluid meniscus is downstream from the area of sample exposed to the X-ray beam (**Figure 3.4c**) and crystallization dynamics are collected (**Figure 3.4f, 3.4i**).

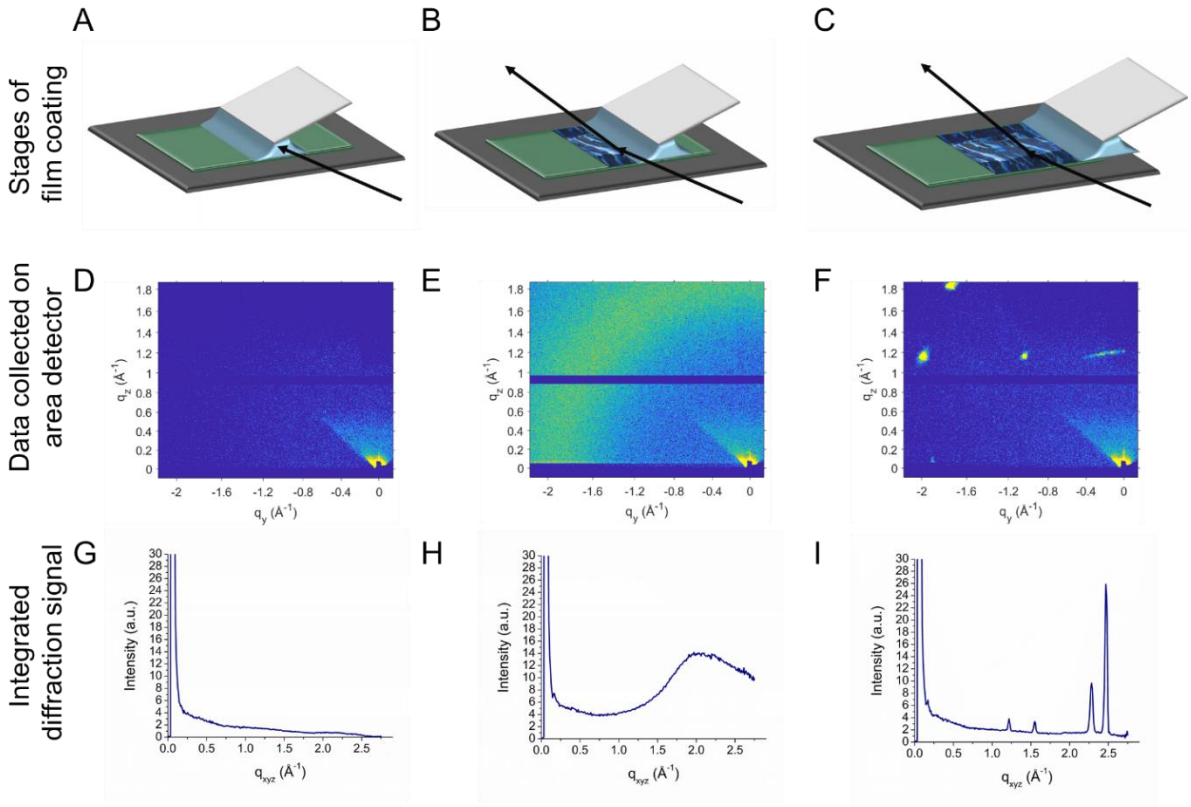

Figure 3.4 Schematic of film coating with a) meniscus upstream from X-ray (indicated by arrow), b) meniscus and evaporation front aligned with X-ray beam and c) crystallization aligned with X-ray (meniscus downstream). A 2-dimensional (2D) detector collects the signal showing temporal stages of crystallization with d) no signal observed, e) broad peak associated with water scattering and f) diffraction signal from crystalline film. The 2D images are integrated to produce 1-dimensional (1D) diffraction signals g) no signal h) broad peak and i) sharp diffraction peaks.

We performed in situ GIXD at CHESS (**Table A3.2**) with varying coating speeds and temperatures to obtain different polymorphic outcomes. Consistent with results from previous work discussed in Chapter 2, slow coating speeds isolate the α polymorph while faster coating speeds isolate β.[22] However, two samples created under conditions to produce the β polymorph produced unexpected results. The β polymorph was isolated, but the diffraction showed time variation in the appearance of Bragg peaks near the (021) plane.

The diffraction intensity as a function of time is presented for a sample coated at 90°C and 0.5 mm s^{-1}, which demonstrated unexpected results (**Figure 3.5**). Time is on the x-axis while q, the momentum transfer vector, is plotted on the y-axis. In the beginning of coating, t = 0 - 0.4 seconds, no diffraction is occurring, and the film coating is occurring upstream from the X-ray beam as in **Figure 3.4a**. from t = 0.4 - 0.5 seconds, diffraction signal appears as well as solvent scattering. From t > 0.5 s, the diffraction peaks continue to develop and evolve (**Figure 3.5a, b,**

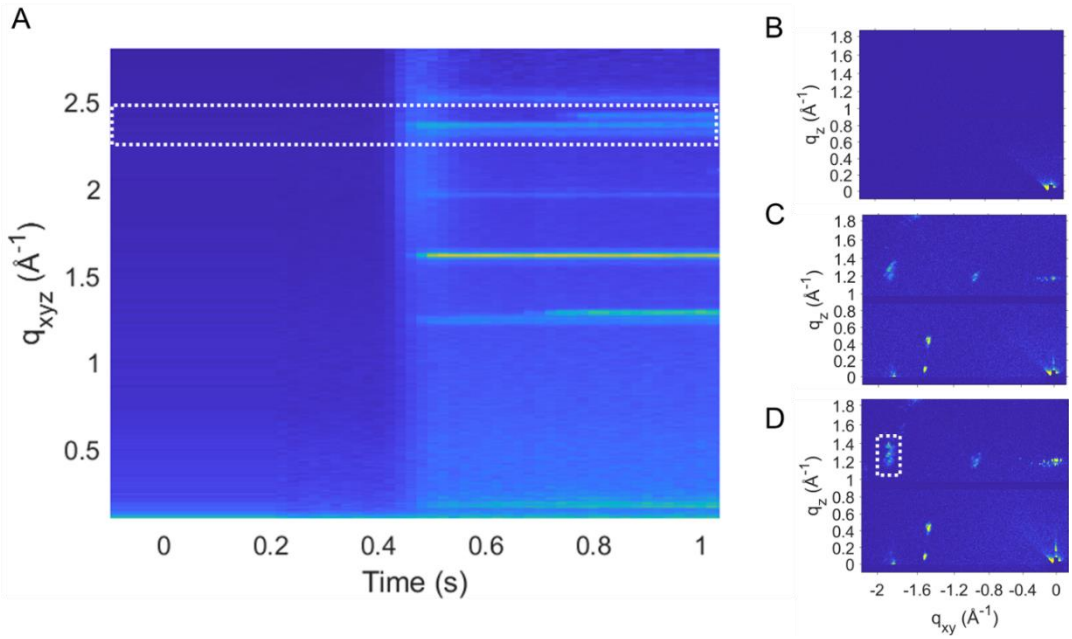

Figure 3.5 a) diffraction signal as a function of time for in situ film coating at 90°C and 0.5 mm s^{-1}. b) initial image with no signal, c) early diffraction and d) final diffraction pattern after film crystallization is complete. Dashed box in subfigures a and d are corresponding regions.

c) suggesting the formation of new crystals. Informed by observations from ex situ sample measurements discussed previously, we note that the (021) peak exhibits the most variation in peak location. From in situ measurements, we are able to observe the time evolution of the (021) peak (**Figure 3.6**). The time dependent peak evolution is presented as 1-dimensional (q_{xyz} (t), **Figure 3.6a**)) and 2-dimensional (q_{xy} and q_z at discrete time points, **Figure 3.6b**). The first peak to appear is located at the expected position (q_{xyz}= 2.37 Å^{-1}). At almost the same time, a second

diffraction peak appears below the first peak. Within 300 ms (between 0.5 and 0.8 seconds, **Figure 3.6b**), we observe the formation of a third peak positioned below the first two.

The peak positions were determined by performing three Gaussian fits (**Figure 3.6c**). The peaks appear to be discretely spaced with the middle peak falling at the expected equilibrium peak position for the (021) plane of β glycine. Recall from **Table 3.1**, the expected position of the (021) diffraction peak is at q_{xyz} = 2.37 Å^{-1}. However, we see evidence two additional possible crystal structures or orientations in the film, as evident by the presence of two additional and discrete Bragg diffraction peaks (centered at q_{xyz}= 2.32 Å^{-1} and q_{xyz}= 2.42 Å^{-1}). The three peaks observed using in situ measurement correspond with the variation in peak position observed in

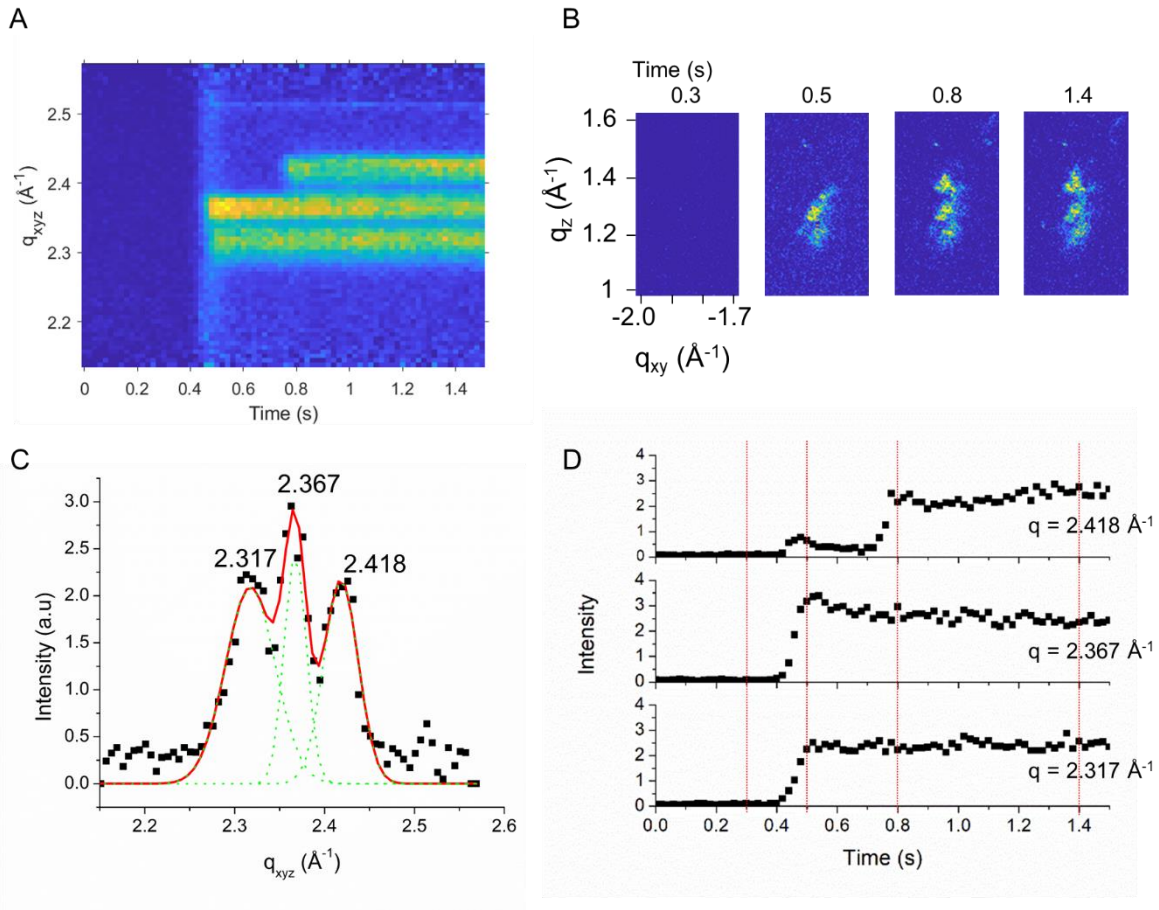

Figure 3.6 a) 021 peak evolution as a function of time in 1-dimension. b) Looking at the diffraction in 2 dimensions reveals that the new peaks appear shifted in the q_z direction from the original peak position. c) Three gaussian peak fits show that the middle peak is centered at 2.367 Å^{-1}, corresponding to the expected (021) peak position for β glycine. D) Time resolved peak intensity for each of the three diffraction peaks.

ex situ experimentation, where the Bragg peak positions sometimes were found at q_{xyz} = 2.42 Å^{-1} and q_{xyz} = 2.32 Å^{-1}.

To determine the origin of these new peaks, the peaks were indexed (indicated by white diamonds in **Figure 3.7**) by simulating expected peak positions for different crystal orientations in the films. A (001) orientation explains the occurrence of the middle peak at q_{xyz} = 2.37 Å^{-1} (**Figure 3.7a**), and identifies this as the true (021) peak. The (100) orientation accounts for the top peak at 2.42 Å^{-1} (**Figure 3.7b**), which could be identified as the (120) Bragg peak. The (010) crystal orientation (indexed in **Figure 3.7c**) was not observed. Therefore, the peak at 2.32 Å^{-1} is still not accounted for. However, this peak could be associated with the (10-2) crystal plane, through comparison to a powder diffraction pattern. Because peak indexing could account for the observed peaks, it is more likely that changes in crystal orientation are responsible for the multiple Bragg peaks as opposed to new crystal structures or strained lattices as previously found in TIPS-pentacene.[3]

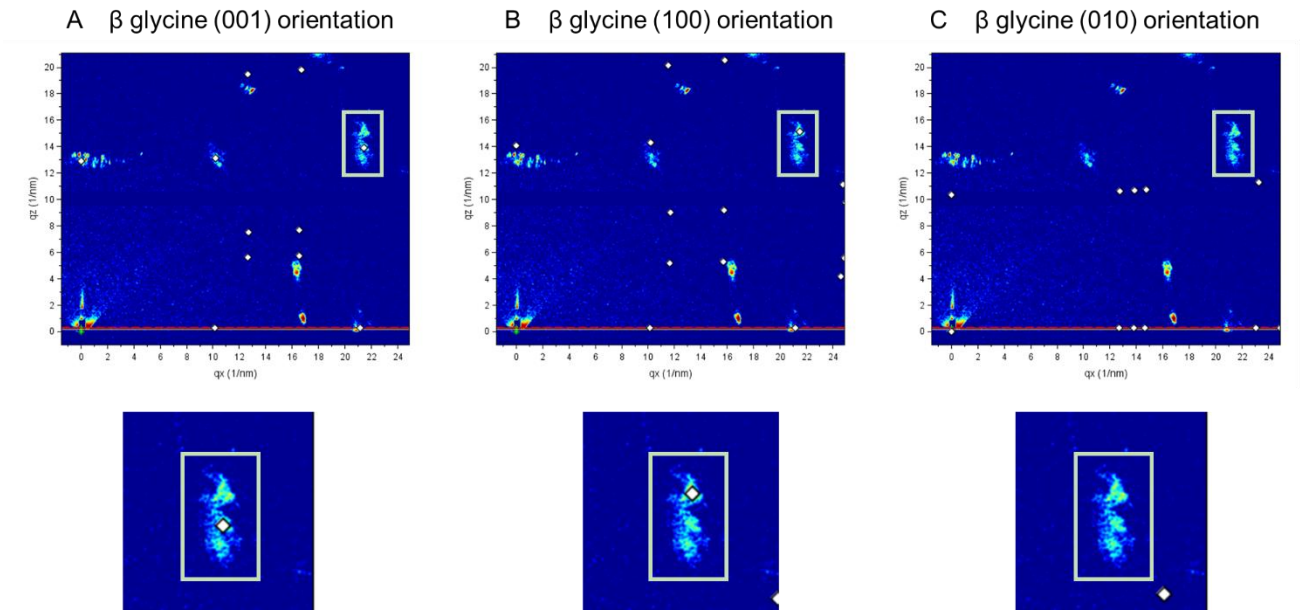

Figure 3.7 Reciprocal space diffraction maps with peak indexing (Note the image is flipped from previous reciprocal maps). a) peak indexing identifies the middle peak associated with (001) crystal orientation. The top peak b) is associated with the (100) orientation. c) The (010) orientation is not observed. Zoomed regions of interest below full diffraction images to view peak indexing more closely.

We found that three peaks appear at different times during film crystallization. The spatial distribution of the peaks can provide insight to mechanism of crystallization to determine how and why different orientations may occur. To probe the location of the different crystal structures in the thin film, we performed depth profiling through changing the incident angle of the X-ray beam. At shallow angles, the surface of the film is sampled while at deeper angles, the full film thickness is probed (**Figure 3.8a**). The in situ data collection was performed with an incident of 0.15°. By

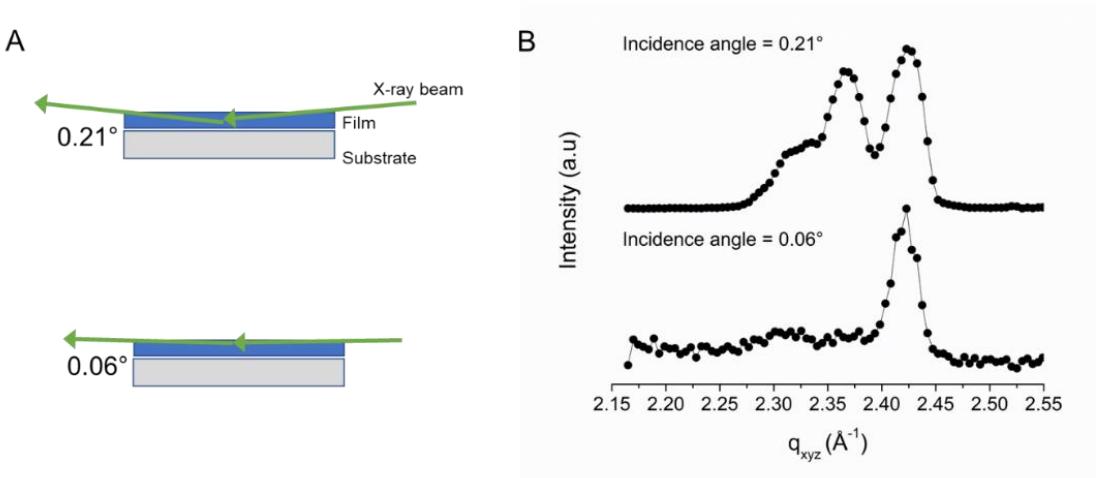

Figure 3.8 a). Changing the X-ray beam incident angle allows for depth profiling for spatial analysis of film heterogeneity A deeper angle penetrates the full film thickness, while a shallower angle grazes the surface. b) Peak intensity of the cluster of three peaks changes as a function of X-ray beam incident angle. The (001) orientation peak (middle peak) appears strongly with a 0.21° incident while the (100) peak at higher q is the dominant peak using a 0.06° incident angle.

changing the angle to 0.21°, we still identify three peaks in the sample (**Figure 3.8b**). However, with a shallow angle of 0.06° the peak at 2.42 Å^{-1} is prominent. The angle scan indicates that there is a depth dependence on location of the crystal orientations. Three orientations of β glycine are present in the film towards the substrate but one orientation (100) is found on the film surface.

We can couple spatial and temporal understanding of peak development to propose a mechanism of crystallization. First, because the (100) orientation is present at the substrate and not at the surface and because this peak appeared first, we can hypothesize that crystallization occurred from the substrate towards the air/liquid interface. Second, we observed that the (001) orientation is isolated on the film surface as crystallization is completed. We hypothesize that as

evaporation of solvent occurs, a thin layer of solvent remains at the air/liquid interface, which creates a confined environment that promotes crystallization of new crystal orientations. This same technique was previously utilized by Giri et al. to probe the spatial and temporal evolution of crystallization in TIPS-pentacene.[6] Their work showed a different mechanism of crystallization; crystallization of the OSC proceed from the air liquid interface towards the substrate, isolating metastable polymorphs (or different orientations) on the substrate.[6] Using in situ X-ray diffraction has revealed that different molecular systems can exhibit different mechanisms of crystallization, resulting in heterogeneous thin film structures.

3.5 Conclusion

In situ grazing incidence X-ray diffraction was used in this work to describe the time dependent formation of different orientations of β glycine. Using ex situ measurement, we saw additional Bragg peaks located near the (021) peak. Motivated by previous work that shows MGC can isolate metastable polymorphs and strained lattice structures, we considered the possibility of metastable β glycine structures through assessing the shift of Bragg peaks to larger reciprocal lattice vector positions. However, observation of different film morphologies using optical microscopy indicated that it was possible that different crystal orientations were isolated in films. Next, we applied the in situ GIWAXD technique to probe crystallization in real time. We observed three peaks appearing near the (021) plane at different times during the coating process. Through peak indexing, we identified that the Bragg peak shifts are likely attributed to discrete crystal planes, made apparent due to the existence of different crystal orientations in the films. The (001) orientation is last to occur in the film and that the (001) orientation is present towards the film surface while the (100) orientation is predominant towards the substrate. Finally, crystallization occurs from the substrate towards the air/liquid interface in this system.

In this work, collecting additional diffraction information would improve understanding of the different orientations present within samples. If peaks are still not described after gathering more complete diffraction, then orientation arguments may not account for all of the observed diffraction

peaks. In this case, we hypothesize that additional polymorphs could be present in the thin film, as in previous works by Giri et al.[3] In situ GIWAXD has proven to be useful for gaining understanding of dynamic crystallization processes. Across diverse material systems (including organic semiconductors, polymers, cellulose nanocrystals, and now small hydrogen bonding molecules), in situ GIWAXD has provided a means to observe the formation of thin films and has facilitated the development of mechanisms to describe crystallization and film assembly.[14–16,23]

3.6 Chapter 3 Appendix

Table A3.1: Sample conditions and peak positions for (021), (001), (020) peaks for ex situ measurements

	Sample	Speed (mm s^{-1})	Temp. (°C)	(021) Peak		(001) Peak		(020) Peak	
				q_{xyz} ($Å^{-1}$)	% Peak shift	q_{xyz} ($Å^{-1}$)	% Peak shift	q_{xyz} ($Å^{-1}$)	% Peak shift
2016	54_1	0.5	110	2.379	-0.23%	1.285	-1.06%	2.007	0.0%
2016	55_1	1	110	2.414	-1.67%	1.240	2.48%	2.040	-1.7%
2016	56_1	3	110	2.363	0.48%	1.272	-0.11%	1.995	0.5%
2016	58_2	0.5	100	2.276	4.14%	1.248	1.81%	2.000	0.3%
2016	59_1	1.00	100	2.330	1.84%	1.277	-0.50%	1.973	1.7%
2016	60_1	3.00	100	2.346	1.16%	1.253	1.45%	1.959	2.3%
2016	62_1	0.5	90	2.391	-0.72%	1.269	0.19%	2.044	-1.9%
2016	64_1	3.00	90	2.371	0.12%	1.273	-0.19%	1.977	1.4%
2017	179_2	0.5	120	2.362	0.51%	1.261	0.79%	2.003	0.2%
2017	185_5	0.5	110	2.332	1.79%	1.256	1.21%	1.982	1.2%
2017	186_1	1.00	110	2.371	0.12%	1.261	0.79%	1.991	0.8%
2017	196_1	0.3	90	2.370	0.16%	1.271	-0.01%	1.969	1.9%
2017	197_2	0.5	90	2.340	1.45%	1.266	0.38%	1.965	2.0%
2017	201_1	0.1	80	2.350	1.00%	1.257	1.12%	2.009	-0.1%
2017	203_1	0.5	80	2.394	-0.84%	1.276	-0.42%	2.000	0.3%
2017	204_2	1.00	80	2.357	0.72%	1.268	0.25%	1.982	1.2%
2017	209_1	0.50	70	2.350	1.00%	1.261	0.81%	1.982	1.2%
2020	SG1	0.3	90	2.442	-2.87%	1.275	-0.30%	2.023	-0.8%
2020	SG2	0.3	90	2.360	0.61%	1.290	-1.50%	1.990	0.8%
2020	SG3	0.3	90	2.354	0.83%	1.279	-0.63%	1.994	0.6%
2020	SG4	0.3	90	2.446	-3.04%	1.286	-1.16%	1.899	5.3%
2020	SG5	1.3	90	2.390	-0.65%	1.275	-0.34%	2.017	-0.6%
2020	SG6	1.3	90	2.308	2.80%	1.278	-0.57%	1.998	0.4%
2020	SG7	1.3	90	2.413	-1.65%	1.279	-0.65%	2.003	0.2%
2020	SG8	1.3	90	2.365	0.40%	1.281	-0.79%	2.008	-0.1%

Table A3.2: Conditions sampled during in situ experimentation. * indicates observation of additional diffraction peaks

Sample name	Coating temperature (°C)	Coating Speed (mm s^{-1})	Polymorphic outcome (α or β)
SG_341	70	0.5	β
SG_342	70	0.5	β
SG_343	70	0.5	β
SG_344	70	0.5	β
SG_345	90	0.5	β
SG_346	90	0.5	β*
SG_347	90	0.5	β
SG_348	90	0.5	β*
Test 1	100	0.5	β
Test 2	100	0.5	β
SG_349	90	0.1	α
SG_350	90	0.1	α
SG_351	90	0.1	α
SG_352	90	0.1	α
SG_356	90	0.05	α

3.7 References

1. Sun, C. C. Materials science tetrahedron - A useful tool for pharmaceutical research and development. *J. Pharm. Sci.* **98**, 1671–1687 (2009).

2. Zhang, S. & Ali, N. *Nanocomposite Thin Films and Coatings*. *Nanocomposite Thin Films and Coatings* (2007). doi:10.1142/p502.

3. Giri, G. *et al.* Tuning charge transport in solution-sheared organic semiconductors using lattice strain. *Nature* **480**, 504 (2011).

4. Yao, Z. F., Wang, J. Y. & Pei, J. Control of π-π Stacking via Crystal Engineering in Organic Conjugated Small Molecule Crystals. *Cryst. Growth Des.* **18**, 7–15 (2018).

5. Chung, H. & Diao, Y. Polymorphism as an emerging design strategy for high performance organic electronics. *J. Mater. Chem. C* **4**, 3915–3933 (2016).

6. Giri, G. *et al.* One-dimensional self-confinement promotes polymorph selection in large-area organic semiconductor thin films. *Nat. Commun.* **5**, 3573 (2014).

7. Diao, Y. *et al.* Understanding polymorphism in organic semiconductor thin films through nanoconfinement. *J. Am. Chem. Soc.* **136**, 17046–17057 (2014).

8. Riera-Galindo, S., Tamayo, A. & Mas-Torrent, M. Role of Polymorphism and Thin-Film Morphology in Organic Semiconductors Processed by Solution Shearing. *ACS Omega* **3**, 2329–2339 (2018).

9. Dybeck, E. C., McMahon, D. P., Day, G. M. & Shirts, M. R. Exploring the Multi-minima Behavior of Small Molecule Crystal Polymorphs at Finite Temperature. *Cryst. Growth Des.* **19**, 5568–5580 (2019).

10. Sainz-Díaz, C. I., Francisco-Márquez, M. & Soriano-Correa, C. Polymorphism, Intermolecular Interactions, and Spectroscopic Properties in Crystal Structures of Sulfonamides. *J. Pharm. Sci.* **107**, 273–285 (2018).

11. Guthrie, S. M., Smilgies, D.-M. & Giri, G. Controlling Polymorphism in Pharmaceutical Compounds Using Solution Shearing. *Cryst. Growth Des.* **18**, (2018).

12. Horstman, E. M. *et al.* Solution Coating of Pharmaceutical Nanothin Films and Multilayer Nanocomposites with Controlled Morphology and Polymorphism. *ACS Appl. Mater. Interfaces* **10**, 10480–10489 (2018).

13. Zhang, F. *et al.* Repurposing DNA-binding agents as H-bonded organic semiconductors. *Nat. Commun.* **10**, 1–11 (2019).

14. Smilgies, D. M. *et al.* Look fast: Crystallization of conjugated molecules during solution shearing probed in-situ and in real time by X-ray scattering. *Phys. Status Solidi - Rapid Res. Lett.* **7**, 177–179 (2013).

15. Sanchez-Botero, L., Dimov, A. V., Li, R., Smilgies, D. M. & Hinestroza, J. P. In Situ and Real-Time Studies, via Synchrotron X-ray Scattering, of the Orientational Order of Cellulose Nanocrystals during Solution Shearing. *Langmuir* **34**, 5263–5272 (2018).

16. Zhong, Y. *et al.* Blade Coated Hybrid Perovskite Solar Cells with Efficiency > 17%: An In Situ Investigation. *ACS Energy Lett.* **3**, 1078–1085 (2018).

17. Gottlieb, S. Statement by FDA Commissioner Scott Gottlieb, M.D., on FDA's new steps to modernize drug development, improve efficiency and promote innovation of targeted therapies. https://www.fda.gov/news-events/press-announcements/statement-fda-commissioner-scott-gottlieb-md-fdas-new-steps-modernize-drug-development-improve (2018).

18. Yu, L. X. *et al.* Understanding pharmaceutical quality by design. *AAPS J.* **16**, 771–783 (2014).

19. Søndergaard, R., Hösel, M., Angmo, D., Larsen-Olsen, T. T. & Krebs, F. C. Roll-to-roll fabrication of polymer solar cells. *Mater. Today* **15**, 36–49 (2012).

20. Jiang, Z. GIXSGUI : a MATLAB toolbox for grazing-incidence X-ray scattering data visualization and reduction, and indexing of buried three-dimensional periodic nanostructured films. *J. Appl. Crystallogr.* **48**, 917–926 (2015).

21. Iitaka, Y. The crystal structure of β-glycine. *Acta Crystallogr.* (1960) doi:10.1107/s0365110x60000066.

22. Guthrie, S. M., Smilgies, D. M. & Giri, G. Controlling Polymorphism in Pharmaceutical Compounds Using Solution Shearing. *Cryst. Growth Des.* **18**, 602–606 (2018).

23. Gu, X., Gunkel, I., Hexemer, A., Gu, W. & Russell, T. P. An in situ grazing incidence X-ray scattering study of block copolymer thin films during solvent vapor annealing. *Adv. Mater.* (2014) doi:10.1002/adma.201302562.

Chapter 4. Precipitation Dominated Thin Film Formation – A New Regime of Flow Coating for Small Molecules

4.1 Abstract

Continuous crystallization processes are challenging to develop because they must provide control over multiple material attributes, including crystal structure, shape, and size. Recently, flow coating has been applied to small molecule pharmaceuticals and has demonstrated the ability to direct the formation of crystal polymorphs. However, the traditional flow coating regimes (evaporative and Landau-Levich) do not provide desirable size or shape control for these materials, namely the formation of small and low-aspect ratio crystals. In this work, processing conditions are adjusted to achieve three distinct film morphologies, characterized by polarized optical microscopy and scanning electron microscopy. Notably, we identified a set of processing conditions that results in microcrystal formation, facilitated by rapid evaporation and precipitation. We hypothesize the coating conditions affect the relative timescales of evaporation and film deposition, creating a coating regime previously unidentified. Crystals created with this technique produce crystals with average sizes 6-7 μm in diameter with nearly monodisperse size distributions with the average polydispersity index being 0.12. X-ray diffraction is used to assess polymorphism and crystal texture in thin films, revealing that microcrystals are preferentially oriented on the substrate. This work contributes new insight to processing techniques which may be relevant to continuous pharmaceutical manufacturing efforts.

4.2 Introduction

The pharmaceutical industry has made advances towards developing continuous processes for drug production.[1,2] Guided by quality by design (QbD), continuous manufacturing

This chapter will be submitted for publication as:

Stephanie Guthrie, Deflef-M Smilgies, Gaurav Giri. Precipitation Dominated Thin Film Formation – A New Regime of Flow Coating for Small Molecules (*in preparation*).

promises to improve process efficiency and product quality.[3] One challenging step in the production pipeline is associated specifically with continuous crystallization.[4] With continuous crystallization technologies, it is advantageous to have flexibility with product volume, and ease of integration with upstream and downstream unit operations.[5] There is a persistent need to develop scalable crystallization technologies which can provide control over critical characteristics of the final crystal product.[6]

Controlling crystal size, shape and morphology while using scalable manufacturing techniques has become an active field of research.[7,8] Control over crystal size, shape and crystal size distribution (CSD) is necessary because there is a direct relationship of the crystal morphology of the pharmaceutical compound to the eventual biological performance.[9] For example, smaller crystals have shown faster dissolution rates compared to larger crystals due to increased surface area relative to volume.[10]

Crystal shape has been found to impact dissolution profiles as well.[11] Further, low aspect ratio crystals or aggregate shapes, such as spheres, have superior flowability for ease of processing.[11] These low aspect ratio shapes are therefore desirable from a processing standpoint compared to needles and other high aspect ratio shapes.

Multiple technologies have been studied to create these optimal crystal morphologies. Supercritical CO_2 facilitated spray drying have demonstrated their applicability for continuous production of spherical crystals.[12] The incorporation of additives in crystallization processes can also change crystal morphology during crystallization and allow for low aspect ratio crystal shapes.[13] Spray drying has also been utilized to create micro- and nano-crystals, for ease of dissolution.[14]

Another technique that has been utilized to manufacture organic molecule crystals is based on meniscus guided coating.[15] One such technique, solution shearing, is useful for controlled deposition of a thin film from liquid phase solutions.[16] The coating parameters (coating speed and substrate temperature) are used to create solid thin films with controllable thickness

and coverage by modulating evaporation and deposition timescales.[16] Previously, solution shearing has shown sensitivity for controlling polymorphism and modulating crystal morphology in organic semiconductor small molecules and polymers.[17,18] The technique has also gained popularity for fabrication of perovskite based thin films.[19] Recently, solution shearing was applied to pharmaceutical molecules including acetaminophen, glycine, ellipticine and aspirin.[20,21] The coating process was found to provide control over polymorphic phases.

For small molecules, the film deposition is often accompanied by a crystalline phase change; it is of interest to understand how coating parameters can also modulate the morphology of the resulting crystals through directly controlling nucleation and growth.[22] Specifically, we aim to understand the diversity of crystallization outcomes and identify conditions which produce crystals with desirable size and/or shape for their intended application. If it is possible to control these critical process parameters for pharmaceutical crystallization, such as the production of microcrystals and low aspect ratio crystals, solution shearing can be employed as a unit operation in continuous pharmaceutical production processes.

In this work, we study the applicability of solution shearing as a scalable processing technique for the continuous crystallization production of low aspect ratio microcrystals in a thin film. Thin film formulations are a desirable alternative for oral drug formulations when a tablet or liquid formulation is not possible.[23] Alternatively, it is feasible to remove crystals from the substrate after fabrication in the thin film to produce free flowing microcrystals. The use of solution shearing for crystallization control could facilitate the integration of crystallization with formulation of a drug product, thus streamlining the drug product formation process.

Although previous work has shown that multiple crystal morphologies can be isolated using solution shearing, there has been no study on controlling the formation of low aspect ratio microcrystals.[20,21] Here, we utilized higher processing temperatures than has been studied in literature, to create uniform microcrystals with low aspect ratios. We show that solution shearing above the boiling point of the solvent allows us to access a thin film coating regime that has not

been described previously. We demonstrate that the elevated temperature and slow coating speed produce a distinct coating regime for meniscus guided coating techniques, termed herein as a precipitation regime for crystallization. Utilizing solution shearing with these unconventional operating parameters produces a nucleation dominant crystallization regime, for continuous production of microcrystals ~6-7 um in diameter, and these crystal populations are nearly monodisperse (average polydispersity index = 0.12). Grazing incidence wide angle x-ray diffraction was used to assess the crystal texture within thin films. We find that the crystals within microcrystal films are oriented on the substrate, while films that are not close-packed or microcrystalline do not exhibit preferential crystal orientation. This finding contributes technological advancements to the field of pharmaceutical crystallization by presenting a solution for continuous processing with coupled crystal size control, and opens up a new regime of flow coating for other fields where organic molecule crystallization is important, such as in the field of organic electronics and energetic materials.

4.3 Materials and Methods

Solution Preparation: Acetaminophen (98%, Sigma-Aldrich) solutions were prepared with ultrapure water at room temperature (23 °C) with concentrations of 1, 5, 10, 14 mg mL^{-1}. Solutions were filtered through a 0.2 µm filter prior to use.

Solution shearing device: Films were created using an in-house solution coating machine. The equipment contains a custom designed and machined aluminum base with heating cartridges (McMaster-Carr) for thermal control. J-type Thermocouples (McMaster-Carr) and heating components are interfaced with a PID controller (Omega Engineering Inc.) to ensure temperature is maintained at the set point. The aluminum block contains a vacuum connection to secure the substrate to the heat source, ensuring good thermal contact. The shearing blade is secured via vacuum to a blade holder (custom), and is connected to angle/yaw (Opto Sigma Corporation) and height (Edmund Optics) micromanipulators and a motorized linear driver (Zaber Technologies) to control the speed of translation across the substrate.

Shearing Blade Functionalization: A functionalized silicon wafer edge was used as a shearing blade. The shearing blade was functionalized with trichloro(octadecyl)silane (OTS) by activating the cleaned wafer in a UV/ozone cleaner and placing the activated wafer in a 3% OTS/ethanol solution in a crystallization dish for 30 minutes. The functionalized wafer is cured on a hot plate set to 90 °C for 1 hour, and then sonicated for 10 minutes to remove any physically adsorbed material on the wafer surface. The contact angle was assessed to determine that the blade had a hydrophobic character.

Thin film fabrication: Silicon substrates were cut into 1 cm^2 pieces and were cleaned with toluene, acetone, water and IPA then dried under pressurized air. Clean wafers were placed in a UV/ozone cleaner (Bioforce ProCleaner Plus) for 10-15 minutes prior to their use. This treatment facilitates surface wetting of the aqueous solution. To create thin films, the desired temperature was set and applied to the substrates, ranging from 70 - 120 °C and shearing speeds were set at 0.01-3 mm s^{-1} in this work. For microcrystal morphology, 0.01 - 0.05 mm s^{-1} speeds were explored.

Characterization

Scanning Electron Microscopy: Samples were sputter coated with a gold palladium layer using a Hummer V sputter coater (Technics) prior to imaging. A FEI Quanta 650 scanning electron microscope (Thermo Scientific) was used with a 10 mm working distance, 5 KV an accelerating voltage, and spot size of 3-4.

Polarized optical microscopy: A Zeiss Axio Imager A.1 optical microscope (Carl Zeiss AG) with two polarizers oriented orthogonally produced linearly polarized light for characterizing thin film alignment and isotropy. Films were imaged using a Zeiss Axiocam 503 Color camera (Carl Zeiss AG).

Image Analysis: Crystal sizes were measured in ImageJ by drawing a line across the largest dimension of a crystal grain and using the measure feature. At least 40 crystals were measured for each sample, and at least three samples were created at each condition. Crystal

size distributions were plotted on histograms. For each sample, the polydispersity index (PDI) was determined as $PDI = \left(\frac{Standard\ Deviation}{Average}\right)^2$.[24,25]

Interferometry: A Zygo NewView 730 white light interferometer (Zygo Corporation) was used to determine the thickness of the films.

Grazing Incidence Wide Angle X-Ray Diffraction: Grazing incidence wide angle X-ray diffraction was used to characterize thin film polymorphism and texture. Diffraction patterns were gathered at the Cornell High Energy Synchrotron Source (CHESS) at the D-1 beamline (now retired). Incidence angles were set to 0.15°. The beam energy was 10.67 KeV and sample to detector distance was 175-177 mm. The Pilatus 200K detector was positioned to image one quadrant (Cartesian quadrant 2) of the diffraction in reciprocal space, with the beam center in the bottom right corner. The crystallographic orientation of crystals in the thin film was determined using peak indexing, with the indexGIXS software package developed by Smilgies et al.[26]

The crystal structure of acetaminophen form I was simulated in Mercury using previous reports from Nelyubina et al (CCDC deposition 754966, HXACAN30).[27] Form II was simulated from Nichols et al. (CCDC deposition 135452, HXACAN08).[28]

The texture in the film was characterized quantitatively by examining the distribution of diffraction intensity for the (110) crystal plane on a 2D diffraction image. The degree of crystal orientation was quantified by determining the amount of scattering that occurred in the expected (oriented) region of reciprocal space for a sample oriented with the (010) crystal plane parallel to the substrate, relative to the total amount of diffraction associated with the (110) plane.

The (110) plane is located at $q = 0.86\ \text{Å}^{-1}$. Applying a tolerance of $\pm\ 0.05\ \text{Å}^{-1}$, the region of reciprocal space analyzed was set to $0.81\ \text{Å}^{-1} < q < 0.91\ \text{Å}^{-1}$ in order to isolate the signal associated with the (110) plane without including diffraction from other crystal planes. The diffraction intensity of (110) plane (centered at $q = 0.86\ \text{Å}^{-1}$) was plotted as a function of χ (the polar angle of the reciprocal space vector). Background signal was subtracted from the integrated

intensity function prior to determining the degree of preferential orientation, defined in **Equation 1**:

$$Degree\ of\ Preferential\ Orientation = \frac{\int_{\chi=-54.8^\circ}^{\chi=-29.3^\circ} I_{110}(\chi)d\chi}{\int_{\chi=-90^\circ}^{\chi=0^\circ} I_{110}(\chi)d\chi} \qquad \textbf{(Equation 1)}$$

Where χ is the polar angle coordinate and I_{110} is the diffraction intensity associated with the (110) plane (see **Figure A4.6** for further discussion of variable definitions). In an oriented sample, the (110) peak center was determined to be at $\chi = -42.0°$. The full width at half max (FWHM) was found to be $12.76°$. Therefore in the numerator, the limits of the integral to study orientation were established as the peak center ± FWHM ($-54.8° < \chi < -29.3°$). The full signal associated with the (110) plane ($-90° < \chi < -0°$) is expressed in the denominator. An example of this calculation is included in the supporting information.

4.4 Results and Discussion

The solution shearing technique was used to create thin films of acetaminophen. We explored a parameter space using an acetaminophen/water solution (10 mg mL^{-1}), coating speeds ranging from 0.03 - 3 mm s^{-1} and temperatures ranging from 70 - 120 °C. **Figure 4.1a** shows a processing diagram that presents the morphology of acetaminophen crystals as a function of coating speed and temperature. We found three thin film morphologies, which are isolated in discrete regions (annotated in **Figure 4.1a**) on the processing diagram. In region 1, spherulitic crystals (**Figure 4.1b**) are obtained with fast coating speeds (0.3 mm s^{-1} and greater) across all temperatures. Spherulitic morphology was also obtained for coating temperature of 70 °C, and speed of 0.1 mm s^{-1}. In this region, the crystallization process is decoupled from the film deposition process; the film that is originally deposited during solution shearing is amorphous, and transitions to a crystalline film over time when stored at room temperature. The transformation to a crystalline film occurred on a relatively short timescale (minutes) after film deposition. This observation was described previously in our previous work.[20] Spherulitic morphology emerges from radial crystal growth from a central nucleation point. This result follows from the result that the film originally

deposited is amorphous. Therefore, there is no preferential direction to crystal growth, allowing for a spherulitic crystallization from the amorphous phase.

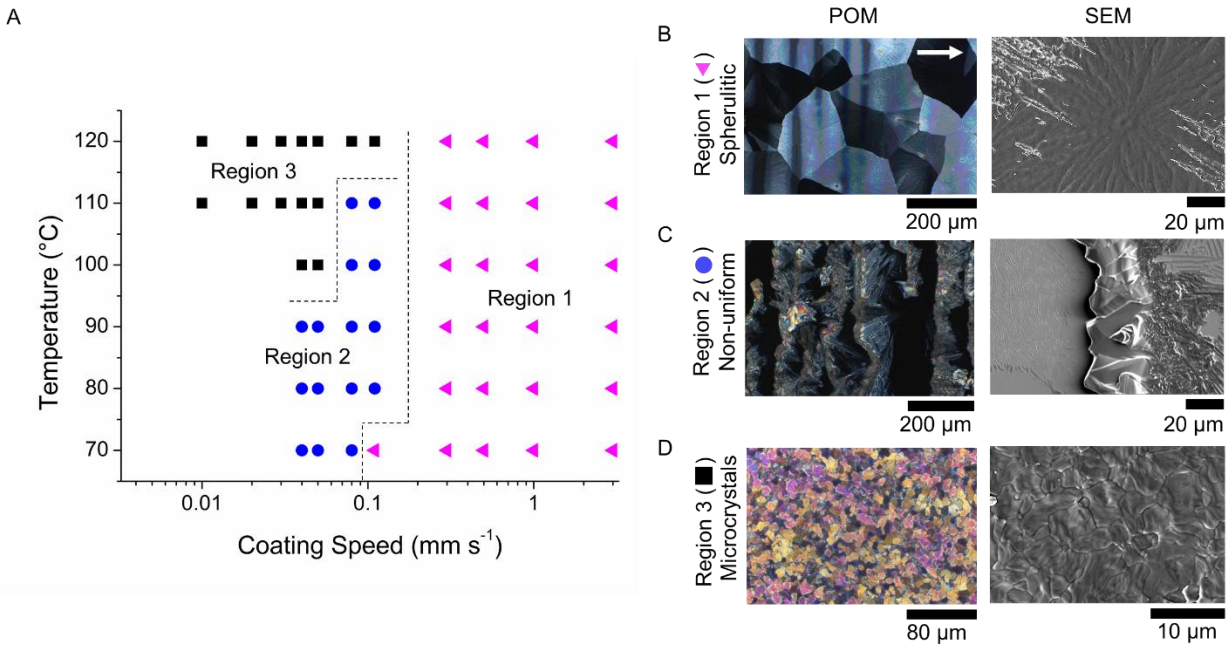

Figure 4.1 a) Processing diagram with solution shearing conditions, created by varying coating speed and substrate temperature for a starting concentration of 10 mg mL^{-1}. Three regions of thin film morphology identified using polarized optical microscopy (POM) and SEM images showing b) spherulitic crystals, c) non-uniform deposits and d) microcrystals. Coating direction indicated by arrow. Scale bars labeled.

Figure 4.1c shows the representative image of films created in region 2, obtained by decreasing the coating speed (0.03 - 0.3 mm s^{-1}), and casting at temperatures below 100 °C. The film morphology created with these conditions is variable ("non-uniform deposits") and the films show incomplete coverage. For these non-uniform films, crystalline acetaminophen is deposited on the substrate followed by a region without a significant amount of acetaminophen, which is assumed to occur due to stick-slip motion of the meniscus.[29]

The SEM of non-uniform deposits shows that the films are composed of thick, faceted crystals. A bulk deposit of material is followed by a region of thinner film, with smaller crystals and some needle-like extensions (SEM in **Figure 4.1c**). We hypothesize that after the larger faceted crystals are deposited, there is depletion of acetaminophen at the meniscus where film deposition occurs. This creates a diffusion limited condition in the thinner film regions. The crystals are also

elongated, due to the concentration gradient that exists during thin film formation when the films are created in this coating regime. While a slower coating speed (region 2) facilitated the formation of the crystalline film without the formation of an amorphous film first (region 1), these conditions did not produce desirable film coverage or low aspect ratio crystals.

In attempts to form a fully covered film, the substrate temperature was increased to 110 and 120 °C, which are above the boiling point of water, the working solvent. Accounting for a temperature drop from the heating source through the silicon substrate, we hypothesized that increasing the temperature (to 110 °C and 120 °C) would allow us to access evaporation at or above the solvent boiling point. These conditions would also allow us to maximize the amount of material deposited on the thin film. Using this set of processing conditions produces the morphology observed in region 3, where we isolated films comprised of microcrystals with highly uniform size and full coverage (**Figure 4.1d**). SEM shows that the microcrystal films are close packed crystals with only slight thickness variation across the film and within individual crystals. Changing processing conditions allows us to isolate unique crystal morphologies, and notably, it allowed us to discover a coating regime for microcrystal production.

To the author's knowledge, there is not another report of using temperatures that exceed the boiling point of the solvent to modulate particle morphology during film deposition. This microcrystal morphology is a great contrast to aligned crystal morphology typically observed from solution shearing. The solution coating process is predominantly utilized in the field of organic electronics and photovoltaics.[30] In these applications, ideal crystal morphology is described by the coherence and alignment of a large crystalline domain, as it facilitates directional charge transport.[31] Therefore, the development of solution coating technology and the typical operational parameters are designed to achieve such characteristics.[32] When utilizing the technology for pharmaceutical crystallization, it is necessary to reassess ideal film morphology characteristics. As a result, sampling a new set of conditions (high temperature and slow coating speeds) allowed this work to access a regime for microcrystal formation.

To explore the limitations of this technique for creating microcrystals, we extend further analyses to include higher (14 mg mL^{-1}) and lower (1, 5 mg mL^{-1}) starting concentrations. All of these concentrations are at and below the solubility limit of acetaminophen in water at 23°C (**Figure A4.1**).[33] We found that microcrystals were isolated at 14, 10 and 5 mg mL^{-1} conditions, but that reducing the concentration to 1 mg mL^{-1} produced films without microcrystal morphology (**Figure 4.2**). We hypothesize that below a critical concentration, the precipitation regime cannot be achieved so that crystal growth occurs, resulting in larger crystallites.

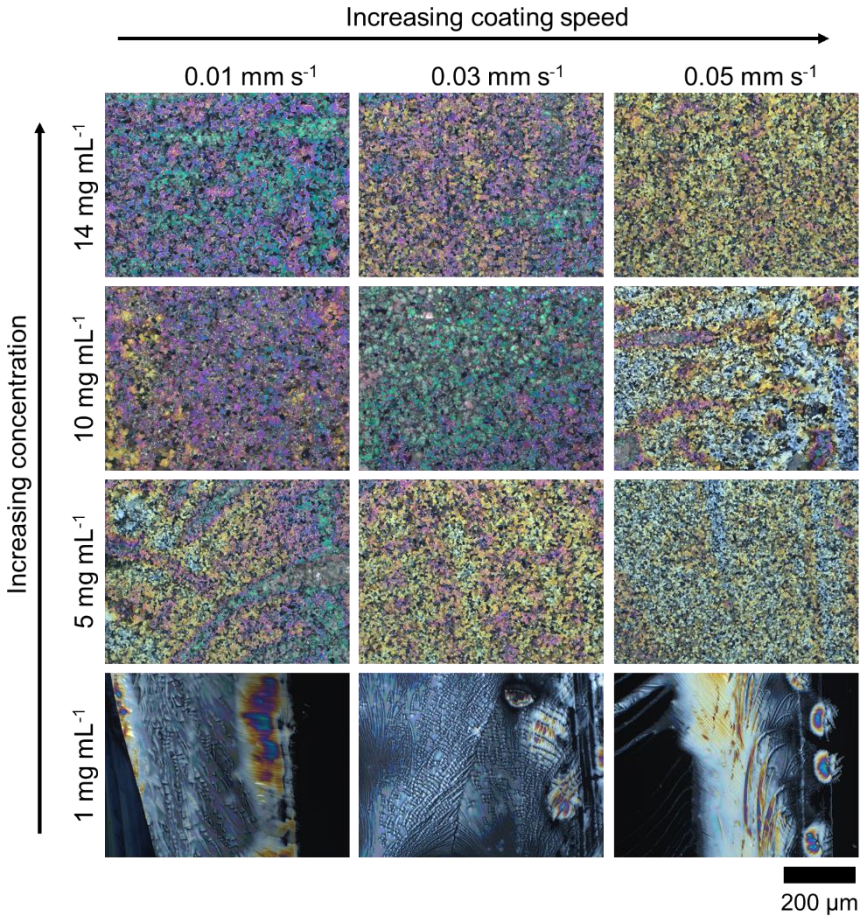

Figure 4.2 Microcrystals are isolated at 5, 10, 14 mg mL^{-1} starting solution concentrations but not at 1 mg mL^{-1}. Scale bar is 200 µm for all images.

We identified previously unobserved crystal morphology by accessing unique processing conditions. We hypothesize that the changes in crystal morphology are closely related to the coating regime and associated relative timescales of evaporation and film deposition.[34] Therefore,

it was of interest to investigate and characterize the coating regime and compare it to traditionally understood theory surrounding solution shearing.

Solution shearing and other meniscus guided coating techniques utilize fluid flow to create a uniform film. The shape of the meniscus is significant in directing film assembly, and frequently, the coating regime is characterized through relating the change in film thickness as a function of coating speed.[16,35] Described extensively in literature, slow coating speeds are associated with an evaporative coating regime, where an inverse relationship describes the coating speed and film thickness (thickness $\propto$ coating speed^{-1}).[16] Faster coating speeds are associated with the Landau-Levich coating regime, where the film thickness and coating speed are positively correlated (thickness $\propto$ coating speed$^{2/3}$).[16]

The coating regime for microcrystal thin films was characterized by determining the relationship between film thickness and coating speed. In **Figure 4.3a**, it can be seen that at all concentrations tested, the films are microns thick and do not have a dependence on either concentration or coating speed. Creating a log-log plot of the thickness as a function of coating speed and performing a linear fit, there does not appear to be an inverse relationship between film thickness and coating speed, as occurs in the evaporative regime (**Figure A4.2**). For each concentration, operating at slow coating speeds (0.01 - 0.05 mm s^{-1}) and elevated temperature (120 °C) produces films whose thicknesses do not follow evaporative or Landau-Levich regime trends. In fact, the coating speed does not appear to be a significant predictor of film thickness under these processing conditions.

These results suggest that solution shearing films above the boiling point of the solution results in a novel coating regime. While the Landau-Levich and evaporative regimes are well understood, the observed results here are not well described by these regimes. In the Landau-Levich regime the timescale (τ) of fluid deposition is slower than the timescale of fluid evaporation ($\tau_{\text{deposition}} < \tau_{\text{evaporation}}$). Relative to the Landau-Levich regime, the evaporative regime exists at

slower coating speeds. Slowing the coating speed allows for the formation of a well-developed meniscus to finely control the coating process. In this regime, the timescale of film deposition is on the same order of magnitude as the timescale of fluid evaporation ($\tau_{\text{deposition}} \sim \tau_{\text{evaporation}}$).

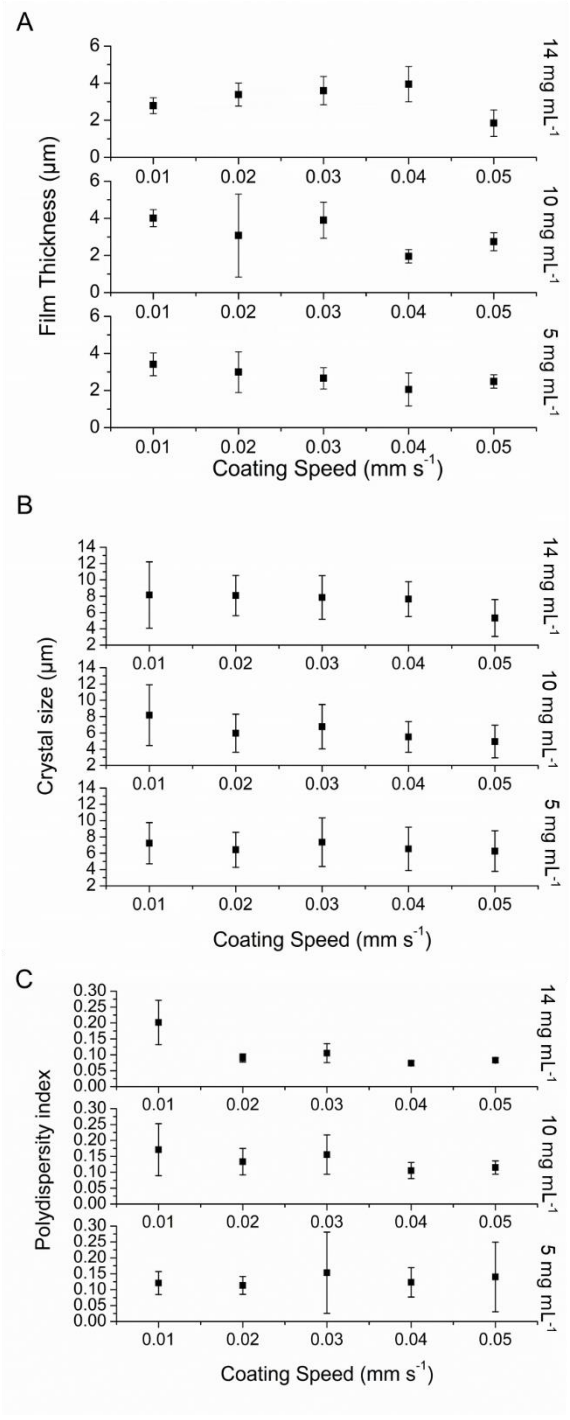

Figure 4.3 Film thickness (a), crystal sizes (b) and polydispersity (c) of samples fabricated at 5, 10, and 14 mg mL^{-1} concentrations, with coating speeds from 0.01-0.05 mm s^{-1}.

We hypothesize that the new regime described here is formed due to the fast evaporation relative to film deposition ($\tau_{\text{deposition}} > \tau_{\text{evaporation}}$). At higher temperatures, we hypothesize that the meniscus recedes and decouples the coating process such that the coating speed is not a significant parameter to control the film thickness. The fast evaporation rate causes rapid nucleation, which allows for the formation of small microcrystals. Therefore, we have identified a new application of the solution coating technique for the production of microcrystals, facilitated by the use of fast evaporation relative to the timescale of film deposition.

The change in microcrystal size was investigated as a function of coating speed and the initial solution concentration. The coating speed was varied from 0.01 - 0.05 mm s^{-1}, with concentrations of 5, 10 and 14 mg mL^{-1} since

these conditions consistently produced the desired microcrystal film morphology. Crystal size distributions (CSDs) were plotted on histograms and the average crystal size was found for each population (**Figure A4.3**).

The microcrystals were analyzed to determine the average crystal size and the polydispersity index, $PDI = \left(\frac{Standard\ Deviation}{Average}\right)^2$. We found that crystal sizes are not predictably different when changing processing conditions or the starting concentrations, and that most samples contained a similar distribution of crystal sizes, with the average size being 6-7 μm (**Figure 4.3b, Tables A4.1, A4.2, A4.3**). A polydispersity index of < 0.1 is an indication that the distribution of particles is monodisperse; most crystals are the same size (**Figure 4.3c**).[24,36] We found that the PDI of microcrystal samples can reach < 0.1 with the average PDI across all samples being 0.13. This indicates that it is possible to obtain a monodisperse CSD, however there is some variation from sample to sample.

Most applications of solution shearing (which utilize moderate temperatures and faster coating speeds) achieve control over crystal alignment through controlling crystal growth after limited nucleation events.[22,31] We hypothesize that the microcrystals obtained here are formed through reaching a condition that biases nucleation over growth. Further, because we do not observe significant change in microcrystal size across different processing conditions (speed, temperature and concentration), we hypothesize that the crystal growth must be limited, such that nucleation is the primary contributor to the final crystal size. This is similar to other methods of achieving precipitation, such as spray drying.[37] Reducing the starting concentration to 1 mg mL^{-1} prevents the system from achieving high nucleation rates. In this case, all of the fluid evaporates before the precipitation regime is reached, ending the coating process. The morphology returns to the large, aligned crystals as seen in region 2.

Finally, X-ray diffraction was used to understand the crystallization behavior, including polymorphism and crystal texture in thin films, and to understand whether homogenous or heterogeneous nucleation occurs in region 3. Polymorphism was determined by comparison of XRD spectra to previously published data for Form I and Form II of acetaminophen.[27,28] The spherulitic crystals from processing region 1 were found to be Form II while the non-uniform and microcrystal films were both composed of Form I (**Figure 4.4**).[20]

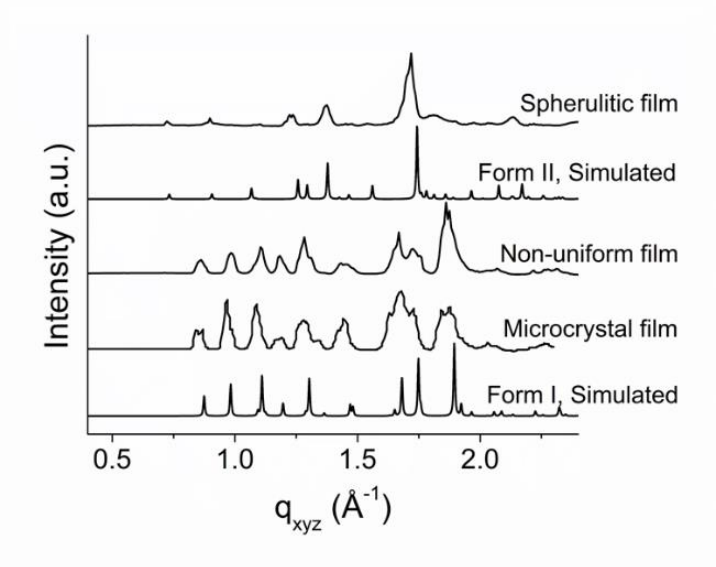

Figure 4.4 Representative XRD spectra of spherulitic, non-uniform and microcrystal crystal morphologies and simulated spectra for Form I and Form II of acetaminophen.

The use of an area detector and a synchrotron X-ray source (CHESS) also enabled us to observe the film texture associated with the different crystal morphologies. The microcrystal and non-uniform film samples produced in regions 3 and 2, respectively, have many crystallites, and each crystallite in line with the X-ray beam produces a unique diffraction event. Interestingly, while the non-uniform films and microcrystal films are both Form I, different film textures are obtained. The diffraction from microcrystal films appears in localized regions (**Figure 4.5a**). This is associated with preferential orientation of crystals on the substrate.[38] Using peak indexing, we found that the 010 plane lies parallel to the substrate (**Figure A4.4**). However, for the non-uniform films (**Figure 4.5b**) the peaks are dispersed without preferential orientation along the annular rings of constant q, associated with randomly oriented crystals.

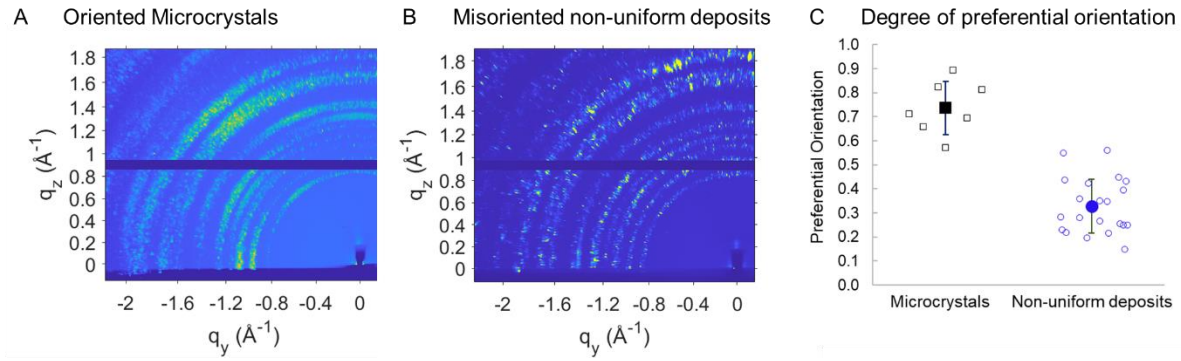

Figure 4.5 a) Microcrystal thin films exhibit preferential orientation. b) Films composed of non-uniform deposits are not oriented with respect to the substrate. c) Microcrystal films (n = 7, average = 0.74, stdev = 0.11) and non-uniform films (n = 22, average = 0.33, stdev = 0.11) show different degrees of preferential orientation, calculated using Equation 1. Groups are statistically different (p-value < 0.05). Sample processing conditions are in Table A4.4, Table A4.5.

To more thoroughly quantify the difference in crystal texture we used **equation 1** to measure the degree of preferential orientation of crystals on the substrate (**Figure A4.5**). The samples created by using processing regions 2 and 3 are divided into two populations according to the observed morphology: films composed of microcrystal morphology and films composed of the non-uniform deposits. Shown in **Figure 4.5c**, the average preferential orientation value for microcrystal films was 0.74 ± 0.11 (**Table A4.4**) while the non-uniform deposit samples had lower preferential orientation with an average value of 0.33 ± 0.11 (**Table A4.5**). The populations were found to be significantly different (p-value < 0.05). The average of the non-uniform deposit samples is similar to the theoretical value associated with an isotropic sample, exhibiting no preferential orientation. The microcrystal films however tend much closer to a having preferential orientation. This is interesting because the microcrystals do not exhibit faceted morphology, yet they are oriented on the substrate. This indicates that the microcrystal films must have some interaction with the substrate, and possibly that heterogeneous nucleation occurs as a mechanism that favors the growth of a (0L0) crystal plane on the substrate.

4.5 Conclusion

This work demonstrates a novel utilization of solution shearing, by using new processing conditions, to create thin film microcrystals with low aspect ratios for utility in the pharmaceutical industry. The morphology of acetaminophen films was described under different processing conditions. Coating speed and processing temperatures were adjusted to obtain three crystal habits (spherulitic, non-uniform faceted deposits, and microcrystals). The microcrystals were produced by using slow coating speeds and high processing temperature (substrate temperature is greater than the boiling point of the solvent).

We characterized the films comprised of microcrystals, including the film thickness, crystal size distributions and polydispersity. Through this, we identify 1) the coating regime produces a unique correlation between film thickness and coating speed and 2) the crystallization regime is similar to precipitation, with nucleation dominating crystal growth.

GIXD was used to assess the crystal form and texture in films. The films created at slow coating speeds were found to be form I of acetaminophen, and the film morphologies are correlated to the film texture. Microcrystal films exhibited significantly more preferential orientation on the substrate compared to the non-uniform crystalline films.

Microcrystals are of particular interest in the pharmaceutical industry, because the size and shape are amenable to fast dissolution, and the flowability of this shape is desirable compared to needles.[9,11] The pharmaceutical industry is actively seeking tools to aid in the production of crystals with controllable size and shape. We posit that this processing method could be adopted and further explored for use in continuous crystallization processes.

This novel regime of flow coating may also be useful in other fields to create new crystalline film morphologies. For example, crystal morphologies can impact charge transport (organic semiconductors and perovskites), battery performance, and even perceived flavors in the food industry[39–42].

4.6 Chapter 4 Appendix

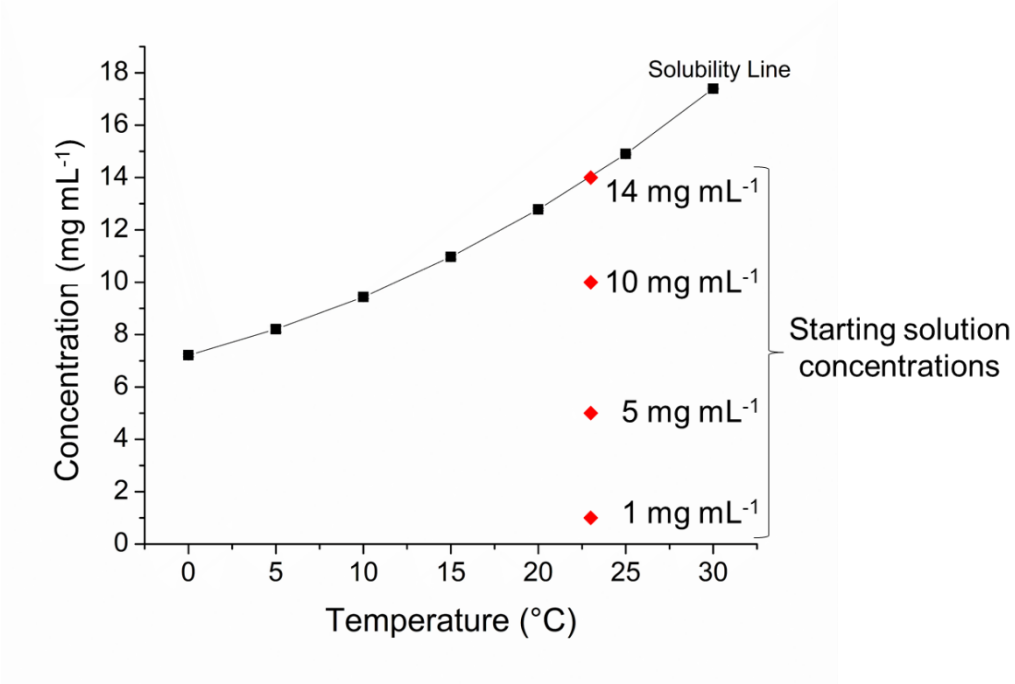

Figure A4.1 Initial solution concentrations (red diamonds) are below the solubility limit (black squares) of acetaminophen in water. Solubility data is from Roger et al.[33]

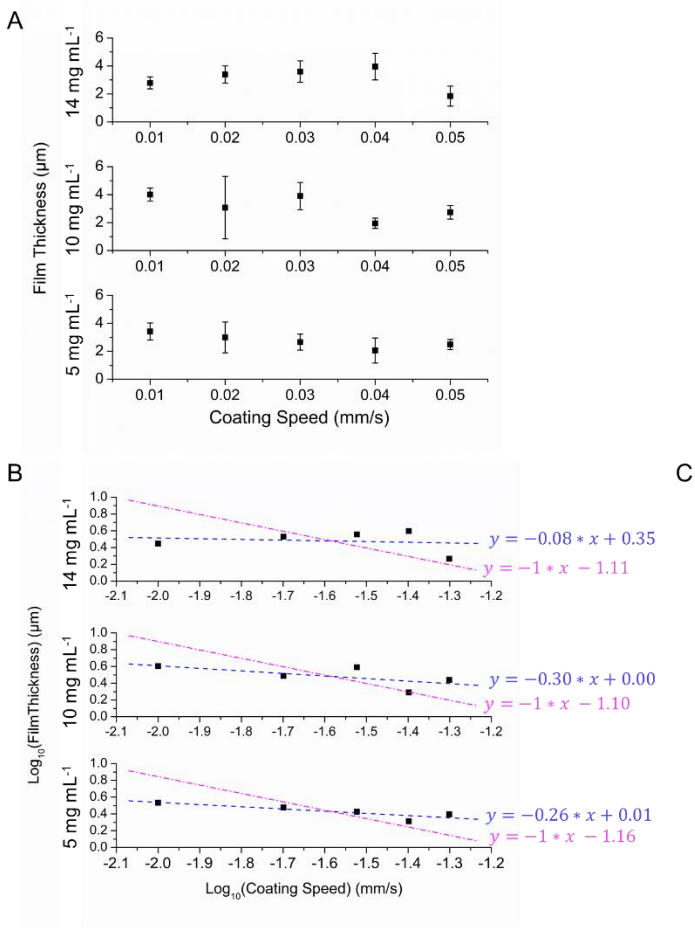

C

Model 1 (– – – – –): *regress* α *and* b *parameters*

$$\log_{10}(Film\ Thickness) = \alpha * \log_{10}(Coating\ Speed) + b$$

	α	b
14 mg /mL	-0.083 (0.270)	0.346 (0.433)
10 mg/mL	-0.304 (0.201)	0.000 (0.323)
5 mg/mL	-0.262 (0.085)	0.012 (0.137)

Model 2 (– · – · –): *Fix* $\alpha = -1$, *regress for* b

$$\log_{10}(Film\ Thickness) = -1 * \log_{10}(Coating\ Speed) + b$$

	$\alpha = -1$	b
14 mg /mL	-1	-1.105 (0.127)
10 mg/mL	-1	-1.102 (0.096)
5 mg/mL	-1	-1.155 (0.093)

Figure A4.2 a) Film thickness as a function of coating speed and concentration. b) log transformed thickness and coating speeds with two linear fits. c) Model 1 (blue, - - - line) presents a better fit to the data, while the evaporative regime model (model 2, pink - . - line) does not fit the data well.

Table A4.1: Crystal sizes and polydispersity for films created using 5 mg/mL acetaminophen in water

5 mg/ml				
Speed (mm s^{-1})		Average (µm)	Standard Deviation (µm)	PDI
0.01	Sample 1	7.02	2.13	0.09
0.01	Sample 2	7.02	2.82	0.16
0.01	Sample 3	7.80	2.58	0.11
0.02	Sample 1	6.66	1.97	0.09
0.02	Sample 2	6.14	2.03	0.11
0.02	Sample 3	6.37	2.41	0.14
0.03	Sample 1	7.20	2.34	0.11
0.03	Sample 2	7.21	1.71	0.06
0.03	Sample 3	7.61	4.15	0.30
0.04	Sample 1	4.87	1.86	0.15
0.04	Sample 2	6.92	1.83	0.07
0.04	Sample 3	7.90	3.10	0.15
0.05	Sample 1	5.62	1.70	0.09
0.05	Sample 2	6.46	1.62	0.06
0.05	Sample 3	6.84	3.52	0.27

Table A4.2: Crystal sizes and polydispersity for films created using 10 mg/mL acetaminophen in water

10 mg/ml				
Speed (mm s^{-1})		Average (µm)	Standard Deviation (µm)	PDI
0.01	Sample 1	6.68	3.42	0.26
0.01	Sample 2	10.19	3.93	0.15
0.01	Sample 3	9.09	2.91	0.10
0.02	Sample 1	5.38	1.62	0.09
0.02	Sample 2	7.05	2.59	0.14
0.02	Sample 3	5.49	2.29	0.17
0.03	Sample 1	7.13	3.32	0.22
0.03	Sample 2	6.09	1.87	0.09
0.03	Sample 3	7.23	2.85	0.16
0.04	Sample 1	5.95	1.97	0.11
0.04	Sample 2	5.69	2.03	0.13
0.04	Sample 3	4.80	1.34	0.08
0.05	Sample 1	5.83	1.76	0.09
0.05	Sample 2	3.26	1.17	0.13
0.05	Sample 3	5.50	1.93	0.12

Table A4.3: Crystal size and polydispersity for films created using 14 mg/mL acetaminophen in water

14 mg/ml				
Speed (mm s^{-1})		Average (µm)	Standard Deviation (µm)	PDI
0.01	Sample 1	10.03	5.27	0.28
0.01	Sample 2	7.09	3.11	0.19
0.01	Sample 3	7.32	2.71	0.14
0.02	Sample 1	7.52	2.11	0.08
0.02	Sample 2	8.51	2.52	0.09
0.02	Sample 3	8.21	2.65	0.10
0.03	Sample 1	6.28	2.35	0.14
0.03	Sample 2	8.14	2.45	0.09
0.03	Sample 3	8.78	2.56	0.09
0.04	Sample 1	7.80	2.20	0.08
0.04	Sample 2	7.03	1.94	0.08
0.04	Sample 3	8.37	2.14	0.07
0.05	Sample 1	4.28	1.19	0.08
0.05	Sample 2	4.29	1.29	0.09
0.05	Sample 3	7.81	2.20	0.08

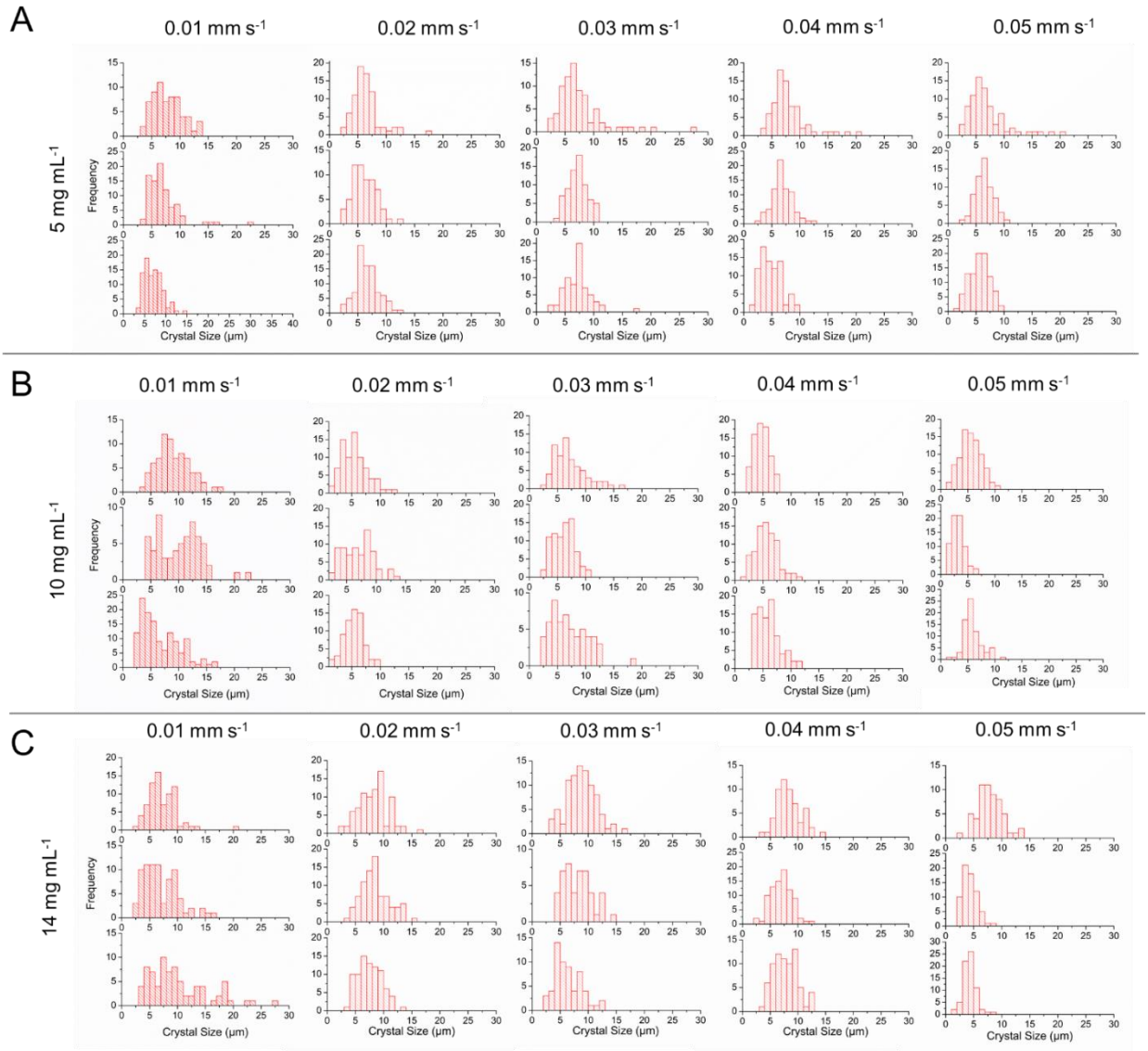

Figure A4.3 Histograms of crystal size distributions for a) 5 mg mL^{-1} b) 10 mg mL^{-1} and c) 14 mg mL^{-1} solution concentrations

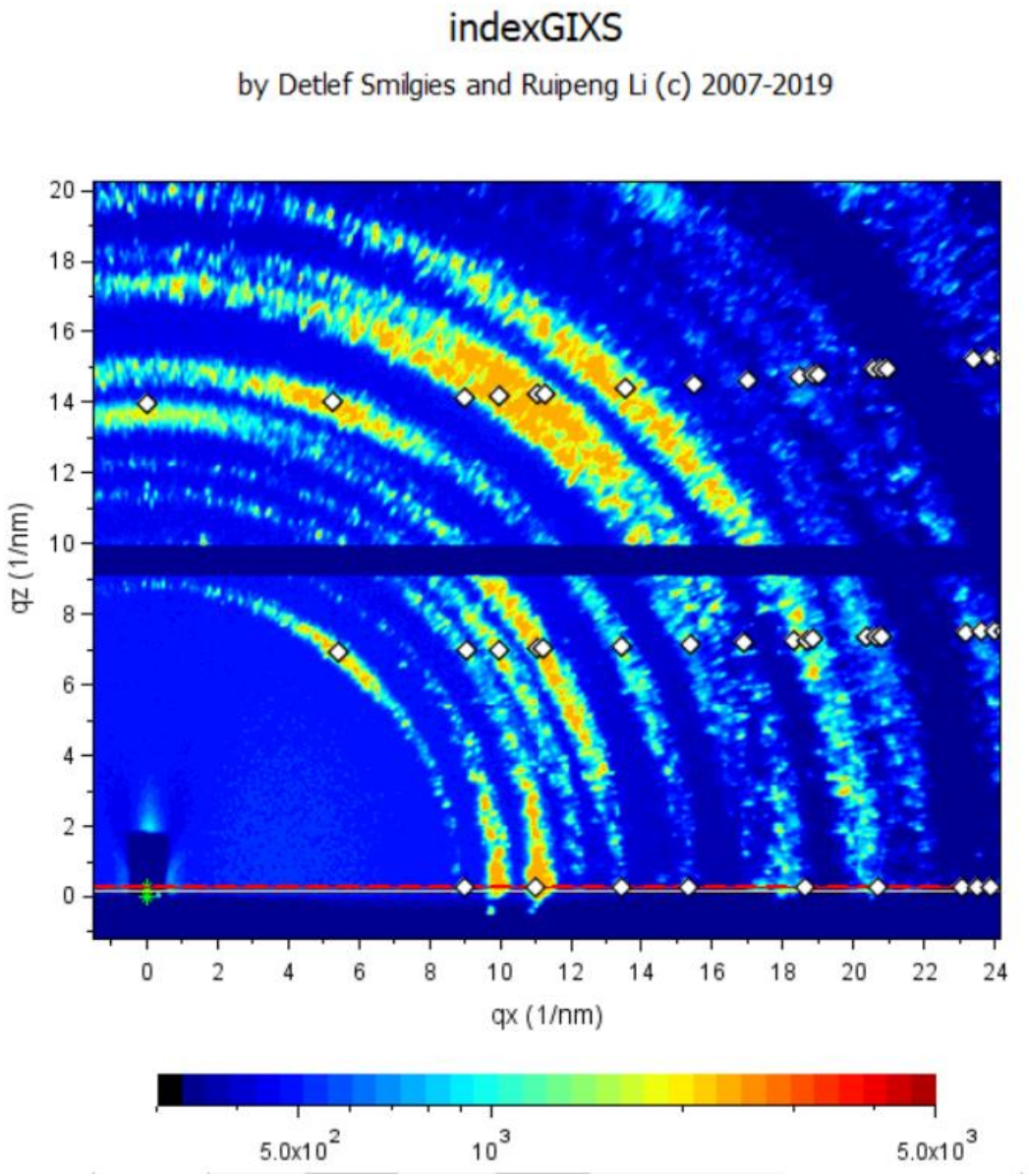

Figure A4.4 Microcrystal film diffraction pattern with simulated 010 oriented Form I peak positions marked (◊). This demonstrates the preferential 010 orientation (the 010 plane lies parallel to the substrate). Figure created using indexGIXS.[26]

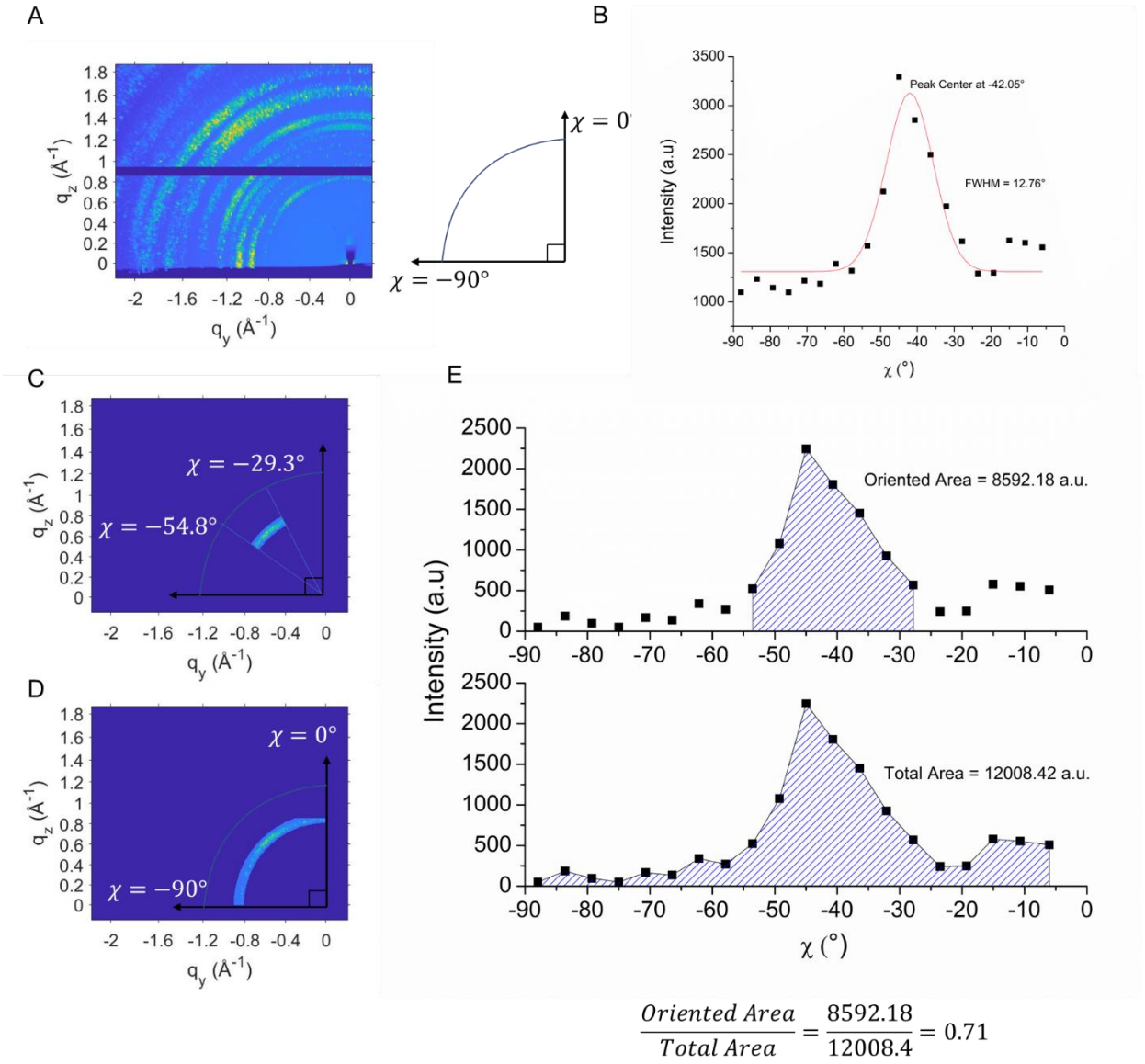

Figure A4.5 a) Full diffraction pattern for microcrystal thin film and axis definition for χ (0° pointing up and -90° to the left). b) integrated diffraction intensity for the 011 plane with gaussian fit, peak center and FWHM. c) Masked diffraction pattern isolating the oriented region associated with the 011 plane and d) masked diffraction pattern isolating the full signal associated with the 011 plane. e) 1D integration of the oriented and full 011 diffraction signals after background subtraction and calculation of preferential orientation =0.71.

Additional comments on Degree of Preferential Orientation:

$$Degree\ of\ Preferential\ Orientation = \frac{\int_{\chi=-29.3^\circ}^{\chi=-54.8^\circ} I_{(110)}(\chi)\, d\chi}{\int_{\chi=0^\circ}^{\chi=-90^\circ} I_{(110)}(\chi)\, d\chi}$$

The theoretical limits of this measure fall between 0 and 1, with 1 corresponding to a highly oriented sample (all diffraction is observed between $-29.3° < \chi < -54.8$. A value of 0 would indicate that none of the diffraction occurs between $-29.3° < \chi < -54.8$. However, an isotropic sample, where the diffraction occurs evenly across the interval (observed as Debye Scherrer rings around the origin) would result in a value of 0.28, as intensity (I) is a constant.

$$Degree\ of\ Preferential\ Orientation\ for\ an\ isotropic\ (powder\ texture)\ sample$$

$$\frac{\int_{\chi=-29.3^\circ}^{\chi=-54.8^\circ} I_{(110)}(\chi)\, d\chi}{\int_{\chi=0^\circ}^{\chi=-90^\circ} I_{(110)}(\chi)\, d\chi} = \frac{I_{(110)} * (-54.8 + 29.3)}{I_{(110)} * (-90 - 0)} = -\frac{-25.5}{-90} = 0.28$$

Therefore, while the theoretical range of this descriptor of orientation is 0 - 1, the expected functional limits are 0.28 – 1.

Table A4.4: Sample conditions and calculated degree of preferential orientation using the method described in **Figure A4.5** for microcrystal thin films (region 3 of processing diagram). Data corresponds to main text **Figure 4.5**.

Films with microcrystal morphology		
Temperature (°C)	Coating Speed (mm s^{-1})	Preferential Orientation
120	0.03	0.71
120	0.05	0.66
120	0.08	0.82
120	0.03	0.89
120	0.05	0.57
110	0.03	0.69
110	0.05	0.81
	Average (n=7)	0.74
	Standard Deviation	0.11

Table A4.5: Sample conditions and calculated degree of preferential orientation using the method described in **Figure A4.5** for nonuniform thin films (region 2 of processing diagram). Data corresponds to main text **Figure 4.5**.

Films with non-uniform morphology		
Temperature (°C)	Coating Speed (mm s^{-1})	Preferential Orientation
110	0.08	0.42
100	0.03	0.25
100	0.05	0.43
100	0.08	0.56
90	0.03	0.40
90	0.05	0.44
90	0.08	0.35
80	0.03	0.22
80	0.05	0.28
80	0.08	0.33
70	0.03	0.25
70	0.05	0.23
100	0.03	0.19
100	0.05	0.36
100	0.08	0.55
90	0.03	0.35
90	0.05	0.15
90	0.08	0.21
80	0.03	0.27
80	0.05	0.25
80	0.08	0.45
70	0.03	0.28
	Average (n=22)	0.33
	Standard Deviation	0.11

4.7 References

1. Mollan, M. J. & Lodaya, M. Continuous processing in pharmaceutical manufacturing: Where we have been and where we are going. *American Pharmaceutical Review* vol. 7 70–75 (2004).

2. Mascia, S. *et al.* End-to-end continuous manufacturing of pharmaceuticals: Integrated synthesis, purification, and final dosage formation. *Angew. Chemie - Int. Ed.* **52**, 12359–12363 (2013).

3. Yu, L. X. *et al.* Understanding pharmaceutical quality by design. *AAPS J.* **16**, 771–783 (2014).

4. Brown, C. J. *et al.* Enabling precision manufacturing of active pharmaceutical ingredients: workflow for seeded cooling continuous crystallisations. *Mol. Syst. Des. Eng.* **3**, 518–549 (2018).

5. Wang, T. *et al.* Recent progress of continuous crystallization. *J. Ind. Eng. Chem.* **54**, 14–29 (2017).

6. Poechlauer, P., Manley, J., Broxterman, R., Gregertsen, B. & Ridemark, M. Continuous processing in the manufacture of active pharmaceutical ingredients and finished dosage forms: An industry perspective. *Org. Process Res. Dev.* **16**, 1586–1590 (2012).

7. Acevedo, D., Yang, Y., Warnke, D. J. & Nagy, Z. K. Model-based evaluation of direct nucleation control approaches for the continuous cooling crystallization of paracetamol in a mixed suspension mixed product removal system. *Cryst. Growth Des.* **17**, 5377–5383 (2017).

8. Jiang, M. *et al.* Towards achieving a flattop crystal size distribution by continuous seeding and controlled growth. *Chem. Eng. Sci.* **77**, 2–9 (2012).

9. Dizaj, S. M., Vazifehasl, Z., Salatin, S., Adibkia, K. & Javadzadeh, Y. Nanosizing of drugs: Effect on dissolution rate. *Res. Pharm. Sci.* **10**, 95–108 (2015).

10. Sigfridsson, K., Lundqvist, A. J. & Strimfors, M. Particle size reduction and pharmacokinetic evaluation of a poorly soluble acid and a poorly soluble base during early development. *Drug Dev. Ind. Pharm.* **37**, 243–251 (2011).

11. Chatterjee, A., Gupta, M. & Srivastava, B. Spherical crystallization: A technique use to reform solubility and flow property of active pharmaceutical ingredients. *Int. J. Pharm. Investig.* **7**, 4–9 (2017).

12. Moura, C., Casimiro, T., Costa, E. & Aguiar-Ricardo, A. Optimization of supercritical CO2-assisted spray drying technology for the production of inhalable composite particles using quality-by-design principles. *Powder Technol.* **357**, 387–397 (2019).

13. Long, B., Ryan, K. M. & Padrela, L. Investigating Process Variables and Additive Selection to Optimize Polymorphic Control of Carbamazepine in a CO2Antisolvent Crystallization Process. *Org. Process Res. Dev.* **24**, 1006–1017 (2020).

14. Kumar, S., Shen, J., Zolnik, B., Sadrieh, N. & Burgess, D. J. Optimization and dissolution performance of spray-dried naproxen nano-crystals. *Int. J. Pharm.* **486**, 159–166 (2015).

15. Lu, Z. *et al.* Meniscus-guided coating of organic crystalline thin films for high-performance

organic field-effect transistors. *J. Mater. Chem. C* **8**, 9133–9146 (2020).

16. Le Berre, M., Chen, Y. & Baigl, D. From convective assembly to Landau - Levich deposition of multilayered phospholipid films of controlled thickness. *Langmuir* **25**, 2554–2557 (2009).

17. Giri, G. *et al.* Tuning charge transport in solution-sheared organic semiconductors using lattice strain. *Nature* **480**, 504 (2011).

18. Giri, G. *et al.* Effect of solution shearing method on packing and disorder of organic semiconductor polymers. *Chem. Mater.* **27**, 2350–2359 (2015).

19. Pascoe, A. R. *et al.* Directing nucleation and growth kinetics in solution-processed hybrid perovskite thin-films. *Sci. China Mater.* 617–628 (2017) doi:10.1007/s40843-017-9043-y.

20. Guthrie, S. M., Smilgies, D.-M. & Giri, G. Controlling Polymorphism in Pharmaceutical Compounds Using Solution Shearing. *Cryst. Growth Des.* **18**, (2018).

21. Horstman, E. M. *et al.* Solution Coating of Pharmaceutical Nanothin Films and Multilayer Nanocomposites with Controlled Morphology and Polymorphism. *ACS Appl. Mater. Interfaces* **10**, 10480–10489 (2018).

22. Diao, Y., Shaw, L., Bao, Z. & Mannsfeld, S. C. B. Morphology control strategies for solution-processed organic semiconductor thin films. *Energy Environ. Sci.* **7**, 2145–2159 (2014).

23. Karki, S. *et al.* Thin films as an emerging platform for drug delivery. *Asian J. Pharm. Sci.* **11**, 559–574 (2016).

24. Clayton, K. N., Salameh, J. W., Wereley, S. T. & Kinzer-Ursem, T. L. Physical characterization of nanoparticle size and surface modification using particle scattering diffusometry. *Biomicrofluidics* **10**, 054107 (2016).

25. Danaei, M. *et al.* Impact of particle size and polydispersity index on the clinical applications of lipidic nanocarrier systems. *Pharmaceutics* **10**, 57 (2018).

26. Smilgies, D. M. & Blasini, D. R. Indexation scheme for oriented molecular thin films studied with grazing-incidence reciprocal-space mapping. *J. Appl. Crystallogr.* **40**, 716–718 (2007).

27. Nelyubina, Y. V., Glukhov, I. V., Antipin, M. Y. & Lyssenko, K. A. 'higher density does not mean higher stability' mystery of paracetamol finally unraveled. *Chem. Commun.* **46**, 3469–3471 (2010).

28. Nichols, G. & Frampton, C. S. Physicochemical Characterization of the Orthorhombic Polymorph of Paracetamol Crystallized from Solution. *J. Pharm. Sci.* **87**, 684–693 (1998).

29. Abo Jabal, M., Egbaria, A., Zigelman, A., Thiele, U. & Manor, O. Connecting Monotonic and Oscillatory Motions of the Meniscus of a Volatile Polymer Solution to the Transport of Polymer Coils and Deposit Morphology. *Langmuir* **34**, 11784–11794 (2018).

30. Gu, X., Shaw, L., Gu, K., Toney, M. F. & Bao, Z. The meniscus-guided deposition of semiconducting polymers. *Nat. Commun.* **9**, 534 (2018).

31. Park, S. *et al.* Large-area formation of self-aligned crystalline domains of organic semiconductors on transistor channels using CONNECT. *Proc. Natl. Acad. Sci. U. S. A.* **112**, 2–7 (2015).

32. Janneck, R., Vercesi, F., Heremans, P., Genoe, J. & Rolin, C. Predictive Model for the Meniscus-Guided Coating of High-Quality Organic Single-Crystalline Thin Films. *Adv. Mater.* **28**, 8007–8013 (2016).

33. Granberg, R. A. & Rasmuson, Å. C. Solubility of paracetamol in pure solvents. *J. Chem. Eng. Data* **46**, 1391–1395 (1999).

34. Michels, J. J. *et al.* Predictive modelling of structure formation in semiconductor films produced by meniscus-guided coating. *Nat. Mater.* 1–8 (2020) doi:10.1038/s41563-020-0760-2.

35. Zhang, K. *et al.* Key role of the meniscus shape in crystallization of organic semiconductors during meniscus-guided coating. *Mater. Horizons* **7**, 1631–1640 (2020).

36. Hughes, J. M. *et al.* Highly monodisperse, lanthanide-containing polystyrene nanoparticles as potential standard reference materials for environmental 'nano' fate analysis. *J. Appl. Polym. Sci.* **132**, 42061 (2015).

37. Yıldız, Ö. Combined precipitation and spray drying for the synthesis of hydroxyapatite nanopowders as soft spherical granules. *Ceram. Int.* **44**, 19809–19817 (2018).

38. Widjonarko, N. Introduction to Advanced X-ray Diffraction Techniques for Polymeric Thin Films. *Coatings* **6**, 54 (2016).

39. Foley, B. J. *et al.* Impact of Crystallographic Orientation Disorders on Electronic Heterogeneities in Metal Halide Perovskite Thin Films. *Nano Lett.* **18**, 6271–6278 (2018).

40. Chen, A. Z. *et al.* Origin of vertical orientation in two-dimensional metal halide perovskites and its effect on photovoltaic performance. *Nat. Commun.* **9**, 1–7 (2018).

41. Zhang, L., Chen, L., Zhou, X. & Liu, Z. Morphology-Dependent Electrochemical Performance of Zinc Hexacyanoferrate Cathode for Zinc-Ion Battery. *Sci. Rep.* **5**, (2015).

42. Quilaqueo, M., Duizer, L. & Aguilera, J. M. The morphology of salt crystals affects the perception of saltiness. *Food Res. Int.* **76**, 675–681 (2015).

Chapter 5. Metal organic frameworks as a host for small molecules: a platform for studying diffusion and molecular uptake

5.1 Abstract

Metal organic frameworks (MOFs) have been proposed to be used as a drug delivery vehicle for small pharmaceutical molecules and protein therapeutics. For this to be achievable, it is essential to understand how small moelcules are incorporated within MOFs. In this work, we develop a platform for crystallization of high aspect ratio MOFs and demonstrate loading the MOF with small molecules. Crystallization of a MOF, HKUST-1, is carried out in nanofluidic channels, where small volumes allow for the formation of high aspect ratio large-crystalline domains of HKUST-1. HKUST-1 crystalline domains with aspect ratios greater than 2500, and lengths up to 144 μm are obtained. We study the ability to load HKUST-1 with flouorescent small molecules, to develop a means to study molecular diffusion in MOFs. We achieved inclusion of the small molecules, anthracene and methylene blue within the HKUST-1 framework, and exclusion of rhodamine B and riboflavin, characterized using confocal fluorescence microscopy. We attribute this selectivity to the analyte size and electrostatic characteristics between the MOF and small molecules. Prior to implementation of MOFs as a feasible platform for drug loading, storage and delivery, the field must develop comprehensive understanding of transport that occurs in MOFs-small molecule systems. This work provides a means to perform such fundamental studies.

5.2 Introduction

Prior to delivery to a biological target in the body, drug materials are assembled as a formulation, designed to keep the drug stable prior to delivery, and to release the drug at the desired time with controlled release kinetics.[1] Polymer or lipid nanocarriers are often selected to store drug compounds and control drug release.[2] Sophisticated designs, such as changing the number of polymer layers (as in core-shell particles) or the thickness of the layers, can be used

Parts of this work are published as:

Guthrie, Stephanie, Luke Huelsenbeck, Armita Salahi, Walter Varhue, Natalie Smith, Xiaohan Yu, Lucy U. Yoon, Joshua J. Choi, Nathan Swami, and Gaurav Giri. Crystallization of high aspect ratio HKUST-1 thin films in nanoconfined channels for selective small molecule uptake. Nanoscale Advances, 1(8), 2946-2952. Some figures reproduced, under CC3.0 License.

to change the relase kinetics.[2] However, each formulation must be carefully designed for the application, with special attention to the timescale of drug release.[3]

Depending on the treatment, the desired timescale of drug delivery is widely variable, from rapid release to sustained release, as long as years (year-long release).[4,5] To account for these drastic differences in timescale, there is a desire to increase the drug loading compacity and have a greater ability to extend release kinetics through novel formulation design. Recently, there has been interest in employing MOFs as a vehicle for drug delivery.[6] Metal-organic frameworks (MOFs) are composed of metal ions or oxo-metallic clusters coordinated with organic linkers. Highly porous, crystalline structures can be created with readily controlled pore geometry and chemistry by changing the metallic cluster or the organic linker.[7,8] Due to their structural and chemical tunability, MOFs are useful for chemical storage, separations, electronic and photonic devices, and catalysis.[9–13]

Drug storage and delivery have emerged as additional applications, where MOF porosity and chemical tunability could increase the functionality of a formulation.[14] The porous nature of the material makes it feasible for high drug loading capacity.[15] The diverse chemical functionality of MOFs can allow for enrichment of molecular entities, such as small molecules and proteins.[16] Chemical interactions between a MOF and a guest molecule in the framework can result in slow diffusion timescales for prolonged drug release.[16] Many MOFs have also shown promising biocompatibility.[17,18] However, the MOF field does not have comprehensive understanding of how molecular transport occurs in the porous network, which presents challenges for rationally designing MOF based drug carrier systems.[19,20]

Similar to drug delivery, where a small molecule would be stored within MOF pores, MOF-based sensors often require a small molecule to functionalize the MOF.[21] Previous studies in sensor development have demonstrated selectivity and enrichment of small molecules with in MOFs.[22] For example, the adsorption capacity of the MOF MIL-101 for methyl orange, an anionic dye, was found to be enhanced by increasing the positive charge present on the MOF.[23] MOF

shape and aspect ratio was shown to be important for separation capability.[20] However, most of the work and fundamental relationships we have regarding transport in MOFs comes from bulk measurement, where transport is occurring on multiple length scales.[20] In order to apply MOFs for drug storage and delivery, it is necessary to develop fundamental understanding of diffusion and transport.[20,24]

One strategy to provide such insight is utilizing a platform to observe and quantify molecular transport directly. To obtain true understanding of transport within a MOF, high quality single crystals should be used, as defects and grain boundaries can impact transport characteristics.[24,25] Therefore, the platform should achieve crystallization of single crystal MOFs, while allowing for observation of molecular transport, using techniques such as fluorescence imaging.

Several groups have utilized confined crystallization to control nucleation and growth of multiple material systems (including small organic molecules, perovskites and MOFs).[26–28] The reduced volumes and small working dimensions in confined systems allow for precise regulation of heat and mass transport to modulate conditions during MOF formation.[26] Recent approaches to confined crystallization in MOFs include interfacial synthesis and diffusion-mediated growth, providing control over MOF aspect ratio and creating oriented MOF thin films.[27–29] Microstamping was used by Ameloot et al. to create nano-sized HKUST-1 single crystals in controlled patterns.[30] Previous work has achieved MOF synthesis (ZIF-8, with aspect ratio 60) by growing nano-confined crystals inside anodized aluminum oxide or track etched polycarbonate membranes.[31] Additionally, MOF nanosheets with aspect ratios of 1000 were formed using a biphasic synthesis method.[32] A technique termed solution shearing can promote self-confined thin film growth in numerous organic molecules.[33–35] Confinement based growth was also achieved by altering the wetting properties of a substrate to grow oriented, single crystals of an organic semiconductor, C8-BTBT.[36]

Building from previous confinement techniques and applying nanofluidic crystallization technology to MOFs, the work presented here demonstrates the utility of nanochannel confinement-based crystallization to create high aspect ratio MOF crystals. In addition to improving MOF morphology control during synthesis, this study aims to lay the groundwork for studying nanofluidic small molecule transport in MOFs.

In this work, a nanofluidic platform was employed to create confinement conditions during MOF crystal nucleation and growth. We show that nano-confinement can aid in producing high aspect ratio, crystalline domains of a prototypical MOF, HKUST-1. Using an evaporation driven synthesis, HKUST-1 nucleation and growth occurs along the nanochannel length to yield high aspect ratio crystals. We observed crystal formation with aspect ratios up to 2500, exceeding that of any other previously reported MOFs.[37,38] The capacity for selective molecular uptake and exclusion in high aspect ratio HKUST-1 crystals is demonstrated using anthracene, methylene blue, rhodamine B and riboflavin. The optically transparent nanofluidic device provides the ability to observe small molecule loading within the MOF, enabling future studies on transport of small molecules within MOFs.

5.3 Materials and Methods

Materials

MOF precursor, fluorophores, and other chemicals. MOF precursor was composed of dimethyl sulfoxide (DMSO, 99.9%), copper (II) nitrate hemi(pentahydrate) ($Cu_2(NO_3)\cdot 2.5H_2O$, 98%) and trimesic acid (H_3btc, 95%), sourced from Sigma Aldrich. Fluorophores were dissolved in pure ethanol (Koptek, 100%). Fluorescent molecules used in this work include methylene blue (certified by the Biological Stain Commission, Sigma Aldrich), rhodamine B (suitable for fluorescence, Sigma Aldrich), anthracene (analytical standard, Sigma Aldrich), and riboflavin (>98%, Sigma Aldrich). All chemicals were used as received.

Nanochannel fabrication and materials. Nanofluidic devices were provided by the Swami group at UVA. Fabrication methods are described in the published article.[39]

Methods

HKUST-1 crystallization. Precursor solution was prepared with $Cu(NO_3)_2$•2.5 H_2O, trimesic acid and DMSO following the general procedure outlined by Ameloot et al.[30] A typical precursor was made by completely dissolving 1.22 g $Cu(NO_3)_2$•2.5 H_2O in 5 mL of DMSO, then dissolving 0.58 g of trimesic acid in the same solution. The final solution volume was 5.625 mL, yielding metal and linker concentrations of 0.93 M and 0.49 M, respectively. Channels were loaded by placing a small quantity (5 µL) of the precursor solution on the channel ports. Capillary action was observed to wick precursor into the nanochannels immediately after placement. Excess fluid at channel ports was gently removed using a Kimwipe. Channels were imaged after loading to determine initial loading efficiency. HKUST-1 crystallization was induced by evaporating solvent from the channels. A vacuum oven could be used to control the pressure to increase evaporation rate and enhance crystallization.

Fluorescent molecule loading. To study molecular uptake in the HKUST-1 crystals, nanochannels containing crystals were immersed in a solution of pure ethanol and a fluorophore (either anthracene, methylene blue, rhodamine b or riboflavin). These solutions were prepared at saturation concentration. The channels with crystals soaked in this solution for 24 hours. To allow sufficient time for the molecule to penetrate the MOF framework and fill the pores. The channels were briefly rinsed with ethanol, dried in ambient conditions, and imaged using a confocal microscope.

Crystal Characterization. A Zeiss Scope A.1 optical microscope with an Axiocam 503 Color camera was used to image crystals within the nanochannels. A Zeiss 780 NLO confocal laser scanning microscope was used for fluorescence imaging of crystals after soaking with the fluorescent molecules. The fluorescence was measured using an external transmission NDD PMT detector.

A Quanta 650 scanning electron microscope (SEM) (5 KV, spot size 4, Everhart-Thornley detector) was used to collect morphological data from crystals in the nanochannels. Energy

dispersive X-ray spectroscopy (EDS) (18 kV beam, Oxford Instruments, X-Max^N 80) was used analyze elemental composition of crystals in delaminated channels. Channels were prepared for SEM imaging by sputter coating them with a protective layer (~20 nm thick) of gold-palladium using a Precision Etching and Coating System (Model 682 PECS).

5.4 Results and discussion

Closed nanochannel arrays are created by the hot embossed bonding of two cyclic olefin copolymer (COC) substrates. The bottom substrate is patterned with nanochannel features that are transferred from a soft stamp embossing process (fabrication is described in the full article,

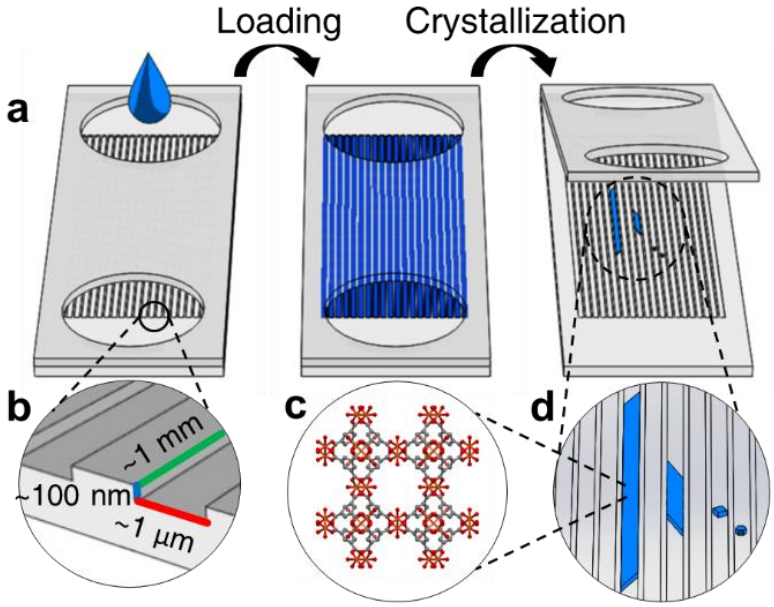

Figure 5.1 a) Schematic of nanochannel loading through ports, followed by evaporation driven crystallization to obtain high aspect ratio MOF crystals b) typical dimensions of fabricated nanochannels c) molecular structure of HKUST-1 and d) high aspect ratio HKUST-1 crystals grown in nanochannels.

and was performed by the Swami Lab in the University of Virginia Department of Electrical Engineering).[39] The top COC plate contains microfluidic through-holes to serve as fluid inlet and outlets surrounding the enclosed channels (**Figure 5.1**).

Each nanochannel array contains a potential loading volume on the order of picoliters per nanochannel, and each array contains 50-100 channels. After fabrication, nanochannel arrays were characterized using interferometry to determine the depth and scanning electron microscopy

to determine the width (**Table A5.1**). Channels with widths 0.5-5 μm, depths 60-350 nm, and lengths 2-5 mm were used in this study (**Table 5.1**).

Table 5.1: Nanochannel specifications for each of the 10 channels in the array

Channel	Width (μm)	Target width during fabrication (μm)	Depth (nm)
1	5	5	285
2	0.72	0.75	100
3	0.5	0.500	<60
4	2	2	325
5	0.76	0.75	60
6	0.43	0.460	<30
7	5	5	325
8	1	1	100
9	10	10	325
10	18.25	20	Not Measured

The nanochannels were loaded (**Figure A5.1, A5.2**) by placing a small volume of HKUST-1 precursor solution (5 μL) in the channel ports. Capillary action wicked solution from the inlets, filling the void space in the empty channels. Crystallization in the nanochannels was induced via solvent evaporation through a combination of vacuum application and heating.

As solvent evaporates from the channels, the solution front recedes at a rate of roughly 0.5 μm hr^{-1}, measured by observing the moving air-liquid interface from optical micrographs. The evaporation rate of solvent is slower than the diffusion rate of the precursors, therefore the spatial concentration of MOF precursor materials can be approximated to be uniform throughout the length of the channel.[40] We hypothesize that during crystallization the concentration increase of the metal ion and the organic linker in the solution is uniform throughout the channel length, and heterogeneous HKUST-1 nucleation occurs throughout the length of the channel, rather than preferentially at the air-liquid interface. However, crystallization also occurs in clusters spanning several channels, suggesting that defects or localized surface properties of the nanochannels may promote nucleation.

Nanofluidic crystallization is able to reduce the occurrence of multiple nucleation events compared to bulk synthetic techniques, due to the reduced volumes available per nanochannel

for crystallization.[41] The decreased number of nucleation events, coupled with slow growth of the MOF crystal, produces large, high aspect ratio crystals that are shaped by the channel dimensions over the course of several days. Crystallization of a MOF includes local densification of precursor materials and assembly into ordered structures.

Bulk HKUST-1, like many other MOFs, is known to have faceted crystal shapes under ideal growth conditions.[42] As the crystals grow, surface energy minimization causes the crystal to exhibit different morphologies. Smaller crystals with square faces (associated with the {100} crystal plane) eventually grow into more stable structures with different faceting (e.g. the hexagonal or triangular {111} planes).[43]

In confined nanofluidic growth, similar faceting is observed and diverse morphologies of crystals in the nanofluidic channels are observed during the growth process (**Figure 5.2**). Observing the population of HKUST-1 crystals that did not grow to fill the channel width, both hexagonal and square prism shaped crystals nucleate in the nanochannels (**Figure A5.3**).

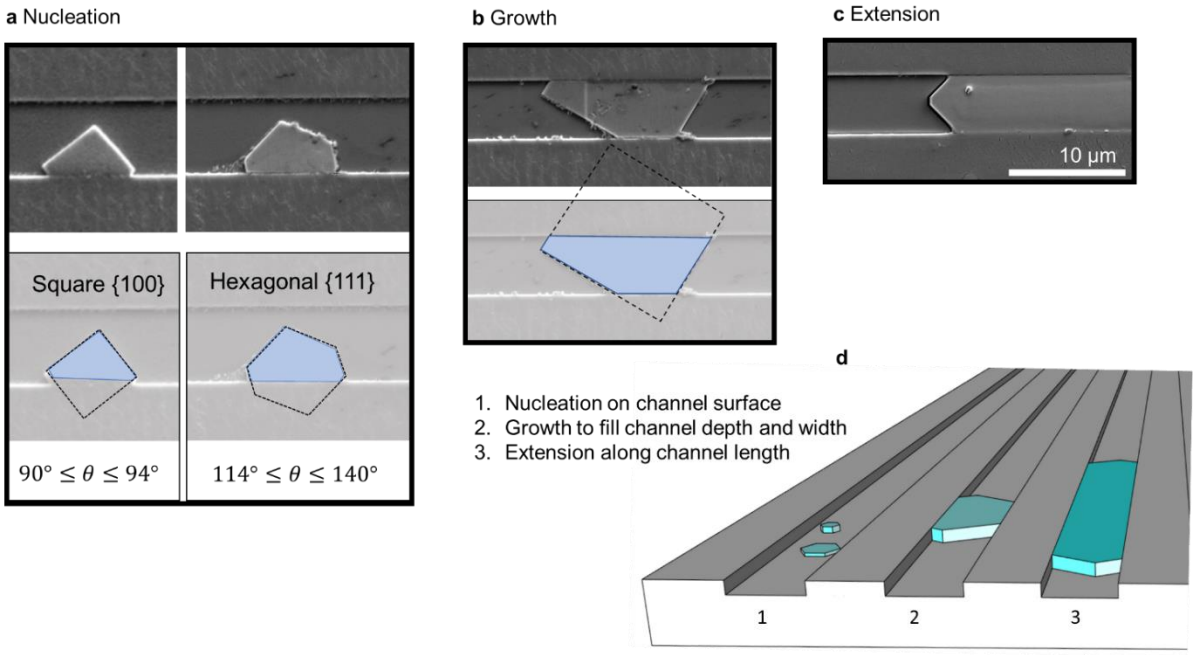

Figure 5.2 a) SEM micrographs demonstrating nucleation of square {100} and hexagonal {111} crystal morphology. b) Growth of a square crystal occurs until inhibited by the channel width and finally c) crystal growth progresses along the channel length to create high aspect ratio MOF crystals of HKUST-1 in nanochannels. d) schematic demonstrating nucleation, growth and extension within nanochannels. Scalebar is 10 µm.

HKUST-1 crystals that grow in the hexagonal shape indicate that the {111} plane is oriented parallel to the nanochannel width, while the square prism shape indicates that the {100} plane is oriented parallel to the nanochannel width. This result agrees with other reported equilibrium morphologies found in thin film and confined HKUST-1, where channel surface chemistry and facet-channel interaction can influence the orientation and morphology of crystals [30,42,44] Faceting is observed on the crystal edges, and we hypothesize that facets correspond to the slow-growing planes associated with the equilibrium HKUST-1 crystal morphology.[42]

As growth proceeds, we hypothesize that the crystal growth is first confined by the nanochannel height (60-350 nm) and then confined by the nanochannel width (0.5-5 μm), depending on the geometry of each channel (**Figure 5.2a,b**). Following these confinement events, crystal growth occurs along the length of the channel (**Figure 5.2c**). This mode of crystalline growth allows HKUST-1 crystal length to greatly exceed the depth.

Assessing the aspect ratio, defined as the ratio of crystal length to depth, we observe that the channels with the shallowest depths (30 nm) produce the largest aspect ratio (**Table 5.2**). The highest aspect ratio observed in this study was approximately 2500 (**Figure A5.4**), an improvement on previously reported results.[38,45] Conversely, the larger depth channels (~300 nm) produce aspect ratios on the order of 200. This finding suggests that depth confinement was significant to producing the highest aspect ratio MOF crystals. The role of channel width on crystallization warrants additional study. However, results suggest that the width dimension does not need to be confined to the same degree as depth (100 nm or less), as widths in the 0.5-1 μm range yield aspect ratios greater than 1000. This is significant, as making and filling channels becomes more difficult as both the depth and width become smaller; hence wider channels that are easier to load with fluid and with nanoconfinement in depth alone are sufficient to form high aspect ratio crystals.

Table 5.2: Channels have depth (~100-350 nm) and width (~1-5 μm) differences to demonstrate the ability to influence aspect ratio. Aspect ratio is defined as the ratio of the longest and shortest dimensions. Table is sorted by increasing depth.

Channel Depth (μm)	Channel Width (μm)	Max Crystal Length (μm)	Aspect Ratio
0.03	0.425	75	2500
0.06	0.5	111	1850
0.06	0.765	132	2200
0.1	0.715	144	1440
0.1	1	108	1080
0.285	5	52	182
0.325	2	143	440
0.325	5	103	316

The material properties of the obtained crystals are also consistent with the expected properties of HKUST-1, characterized by EDS (**Figure A5.5**). The final crystallized material is insoluble in ethanol, while the starting materials, trimesic acid and copper nitrate, are soluble. Hence, upon washing the nanochannels after crystallization, the remaining crystal has a thin film morphology and solvent compatibility consistent with that of HKUST-1. Therefore, nanofluidic channels were utilized to achieve synthesis of large single crystal metal organic frameworks. After removing the top layer of COC to expose the crystals and nanochannels, pure ethanol was used to wash away unreacted material and debris loosely present on the surface.

The functional utility of the porous MOF is demonstrated through the capacity of the crystals to uptake and exclude different molecular species. Four different fluorescently active molecules were selected as candidate guest molecules to demonstrate the loading capacity of a MOF. These molecules were selected because they have similar conjugated cores, with anthracene being the simplest, containing three aromatic rings. The other molecules have larger molecular size and greater chemical complexity due to the introduction of additional functional groups or charges (**Figure 5.3**).

To determine if the small molecules can enter HKUST-1 selectively, anthracene, methylene blue, riboflavin or rhodamine B were dissolved in ethanol at their saturation

concentration at room temperature. The nanochannels were then immersed in the prepared solution and left overnight to allow sufficient time for diffusion to occur before imaging, although diffusion in MOFs has been shown to occur within minutes.[46] **Figure 5.3** summarizes the results of molecular inclusion of methylene blue and anthracene, with the exclusion of rhodamine B and riboflavin.

Previous studies have shown that the MOF ZIF-8 can be loaded with anthracene while still preserving the characteristic fluorescent emission of anthracene.[47] We observed that anthracene can also penetrate the framework of HKUST-1 (**Figure 5.3a**). The presence of anthracene seems to have little effect on the appearance of the HKUST-1 crystal; the brightfield image of the anthracene loaded HKUST-1 does not show any significant change. The methylene

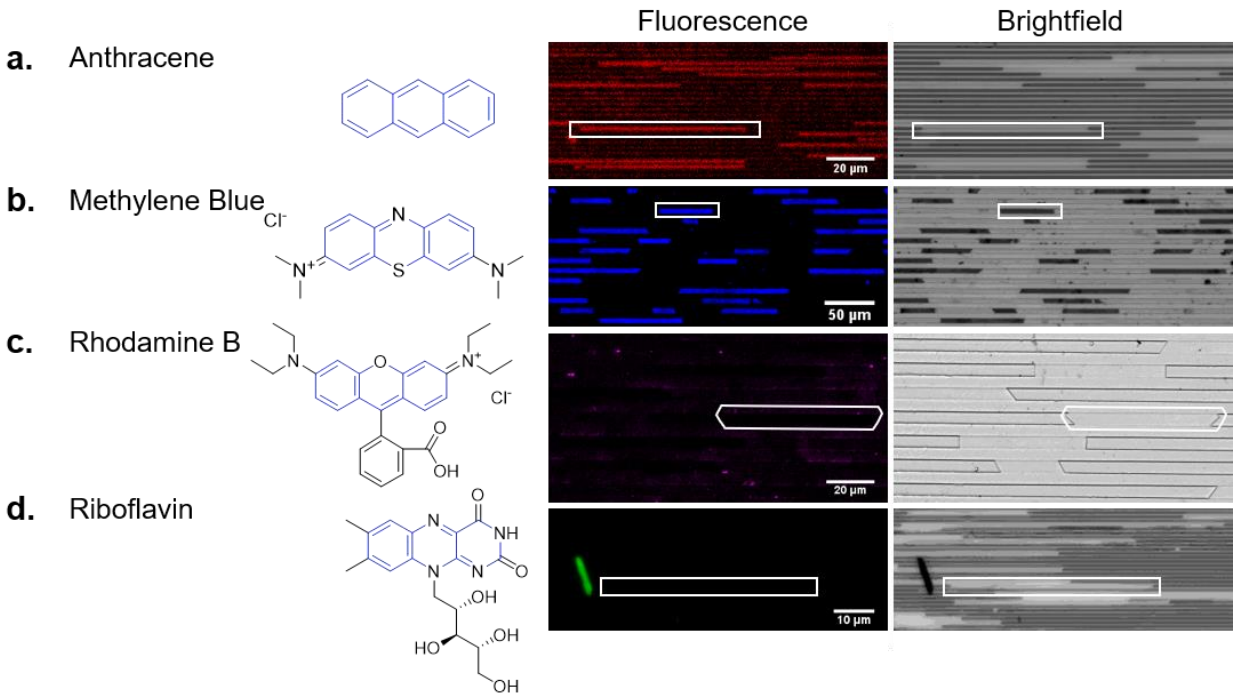

Figure 5.3 a) Anthracene is included within the MOF structure, shown by the co-location of fluorescence signals and the transmission brightfield crystal location. b) methylene blue, is larger than anthracene and is a charged molecule. Fluorescence and brightfield images show that methylene blue is present in the crystal, and is present in a quantity to make the crystal appear darker in the brightfield image. C) Rhodamine B, does not appear to enter the MOF. d) Riboflavin is also excluded from the MOF, with no fluorescence signal detected in regions where HKUST-1 crystals are present in the nanochannels.

blue loaded HKUST-1 (**Figure 5.3b**) appears much darker in the brightfield image, showing that

there is decreased light transmission through the methylene blue loaded HKUST-1 crystals. An optical brightfield image of HKUST-1 as synthesized and loaded with methylene blues shows that in addition to fluorescence imaging, brightfield imaging could be used to easily characterize loading of within the framework. **Figure 5.3c** shows that rhodamine B did not enter the MOF at a detectable concentration. The signal in the image is from small crystallites of rhodamine B deposited on the channel surface, or is noise during the imaging. Finally, riboflavin is not detected within the HKUST-1 crystals either. The images in **Figure 5.3d** show a large crystal, which is hypothesized to be riboflavin that was deposited as ethanol evaporated during the drying process, causing riboflavin to precipitate out of solution.

The advantage of nanoconfined MOF crystallization is the ability to visualize the localization of molecules within the crystal. This is easily seen when contrasting small molecule loading in nanofluidic MOF crystals and bulk MOF crystals. Images of bulk HKUST-1 crystals (those that were formed outside of the confinement region of nanochannels, such as the fluid inlet and outlet) are shown in **Figure 5.4**. These crystals demonstrate the same loading behavior as the confined high aspect ratio crystals, however with weaker signal compared to the nanoconfined crystals. The nanoconfined diffusion path length from the top to the bottom of the channel allows for rapid equilibration of the analytes with minimal concentration gradient across the channel depth. The thin film allows for clear optical or fluorescent detection of analytes due to the uniform optical path length.

Of the small molecules screened for molecular loading, methylene blue demonstrated the most promise for use in characterizing transport within a MOF. The molecule showed strong brightfield and fluorescence signals. The dark blue color of methylene blue could allow for bright-field optical characterization (**Figure A5.6**). However, fluorescence allows for sensitive measurements to be made while minimizing signal from the COC and HKUST-1. Further, fluorescence imaging can provide spatial information about the distribution of a small molecule within the MOF framework (**Figure 5.5**). Therefore, ongoing studies are utilizing methylene blue

loading in HKUST-1 as an ideal model system to understand molecular uptake and loading in MOFs. Through observing the average fluorescence intensity across loaded crystals in the channel, we aim to develop an understanding of loading capacity of small molecules within a MOF.

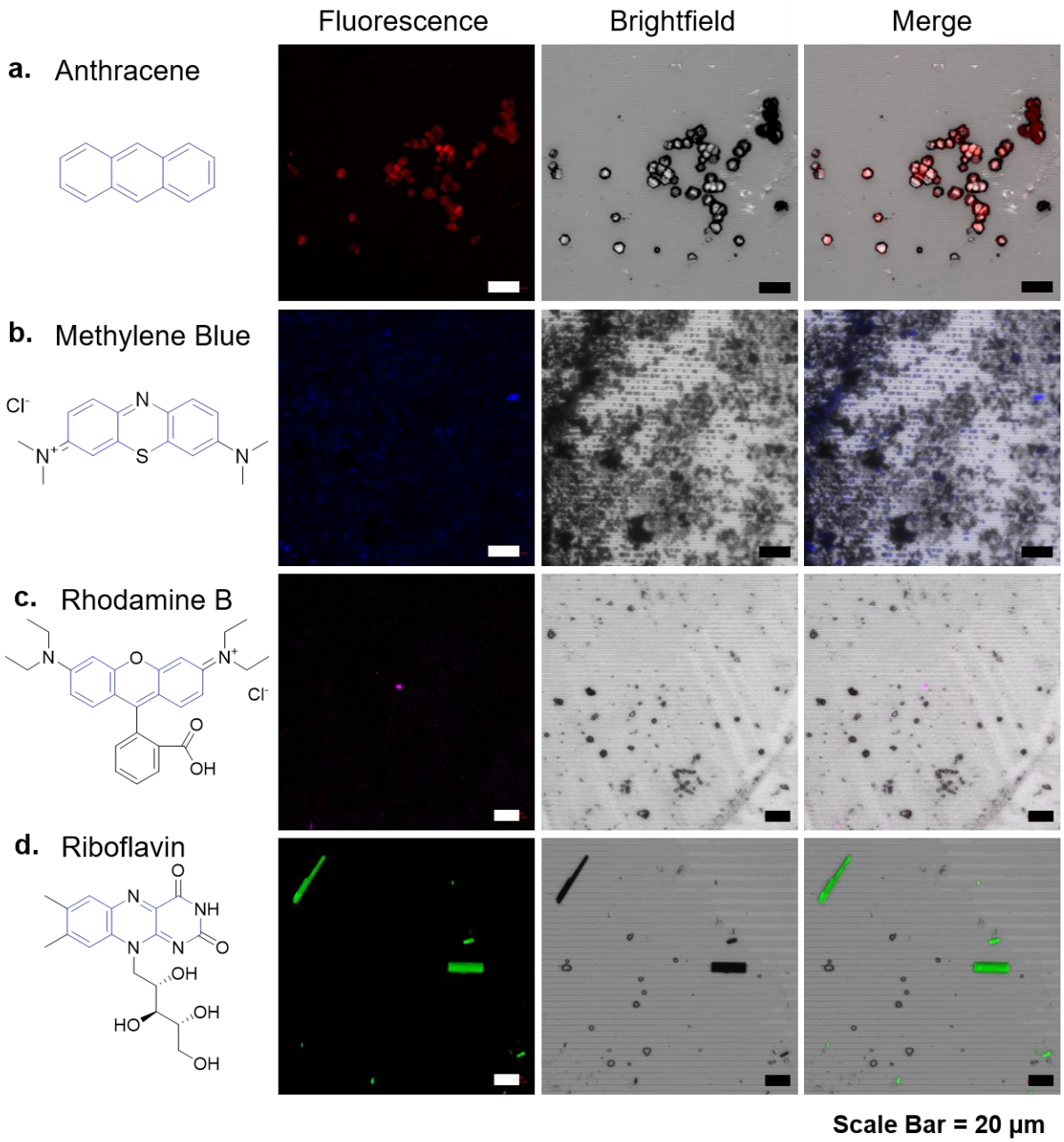

Figure 5.4 Crystals formed on the channels, that can be considered as bulk HKUST-1. a) anthracene, b) methylene blue c) rhodamine B and d) riboflavin. The fluorescence is not located within the HKUST-1 crystals for riboflavin and rhodamine B. Anthracene and methylene blue demonstrate capacity for molecular uptake, with fluorescence appearing in the bulk crystals.

During MOF loading, the bulk solution concentration of the small molecule is important, as it can dictate the partitioning of the small molecule in the MOF. This changes the observed fluorescence intensity. This work has informed the experimental design for additional ongoing studies on small molecule and protein diffusion in MOFs.

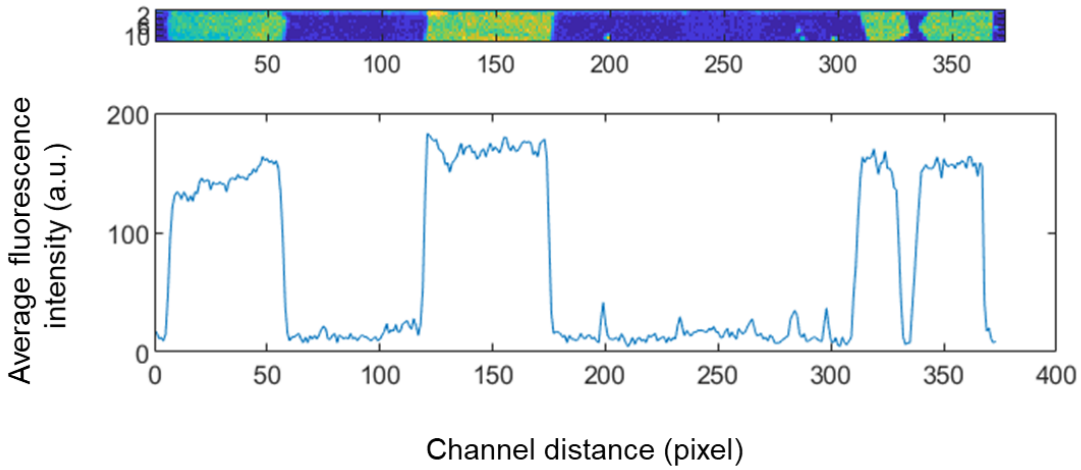

Figure 5.5 Image analysis can provide a means to understand MOF loading capacity. Fluorescence intensity in the MOF can be correlated with bulk solution concentrations, to understand partitioning of small molecules within the framework. This work is towards the effort to develop fundamental understanding small molecule transport in a MOF.

Currently, we are exploring the how changing bulk concentration and loading time impact the MOF loading capacity. We are developing models that can relate these parameters to diffusion coefficients, informed by previous studies.[24] Preliminary results from our work suggest that small molecule diffusion in MOFs is comparable to solid state diffusion timescales, which would allow for longer drug release timescales. Preliminary studies of protein loading and release were performed, where the work showed that lysozyme can be stored inside a MOF (NU-1000), and upon release, it retains biological efficacy as measured by an assay (**Figure A5.7**).

Through this, the utility of high aspect ratio nanochannel crystallization of a MOF is made clear. It can serve as a platform for loading and enrichment of small molecules, while facilitating characterization with high quality visualization of loading.

5.5 Conclusion

We present the first report on crystallization of HKUST-1 in parallel arrays of nanoconfined channels for studying crystal morphology and characterizing selective uptake of small organic molecules. Crystal morphology, porosity, and fluorescence microscopy techniques indicate that oriented, high aspect ratio, crystalline domains of HKUST-1 were formed in nanochannels. This work provides the foundation for a range of fundamental studies involving MOFs with applications in understanding thin film growth, nucleation and growth, as well as diffusion kinetics of guest molecules in MOFs.

With a well-defined and optically accessible growth region, we are able to observe molecular uptake in MOF crystals using fluorescence microscopy. The nanofluidic device studied here can be further developed with patterning and dynamic flow control for increased control over crystal growth direction and morphology. In future work, fluid flow can also be introduced into the nanochannels after the creation of high aspect ratio MOF crystals to achieve spatial and temporal control control over the introduction of guest molecules, such as small molecules and proteins.

The work also demonstrates that MOFs are not universally compatible for storage of all small molecules. For drug delivery, a small molecule-MOF combination would need to be carefully designed such that 1) the small molecule can enter the MOF 2) it can load at a minimum capacity to achieve a therapeutic dose and 3) release on a controlled timescale. There is a rich field of future work possible with this technology, as the platform is ideal for integration with many applications (including sensing, separations and drug delivery). We intend to study the diffusion of small fluorescent molecules out of the HKUST-1 crystal in the nanochannels. This is important for understaning mechanisms of diffusion in MOFs, which can verify the feasibility of using MOFs as drug delivery vehicles.

5.6 Chapter 5 Appendix

The fabricated channels are located on a COC wafer, 4” in diameter. This contains multiple arrays, for higher throughput experimentation (Figure S1). The arrays were characterized for controlled length, width and depth.

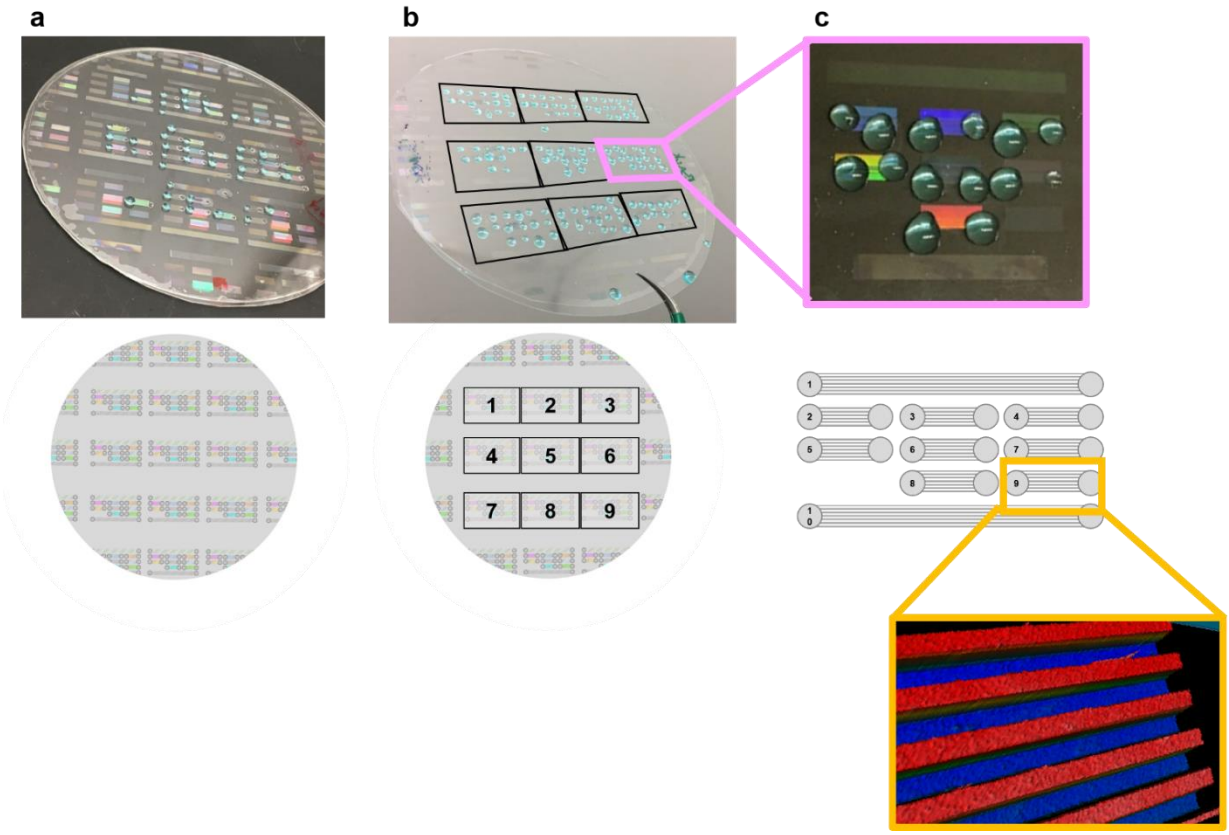

Figure A5.1 a) Overview of the fabricated nanofluidic device b) The device contains nine complete sets of nanochannels, with each set containing c) 10 channels, each with a specified length, depth and width.

Nanofluidic channel depth and width characterization

Channel depth was measured using a Zygo white light interferometer, while channel width was measured using SEM. **Table A5.1** outlines the two examples of the measurements and recorded channel depth.

Table A5.1: Width and depth measurements taken from SEM and a white light interferometer. This demonstrates the capability creating crystals with highly controlled width and depth through nanofluidic confinement. SEM images show the sharp edge features for high quality control over morphology.

Channel Type	Depth Measurements (Zygo interferometer measurements)	Width (from SEM) characterization
Narrow	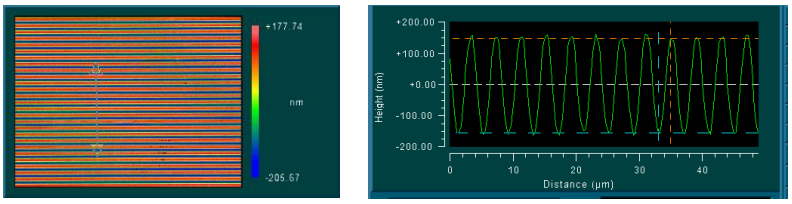	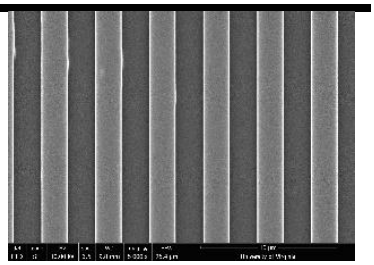
	325 nm	2 µm
Wide	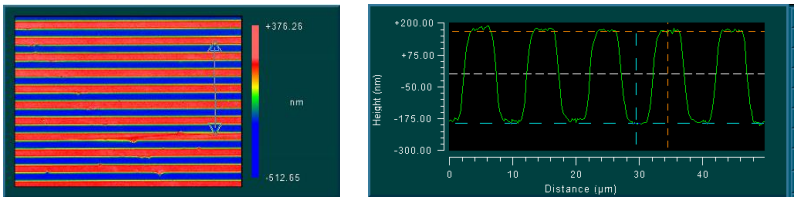	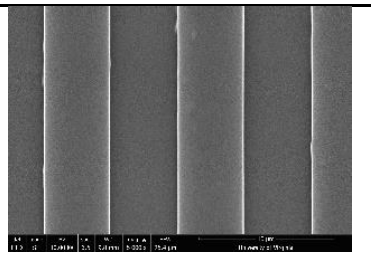
	325 nm	5 µm

Channel Loading

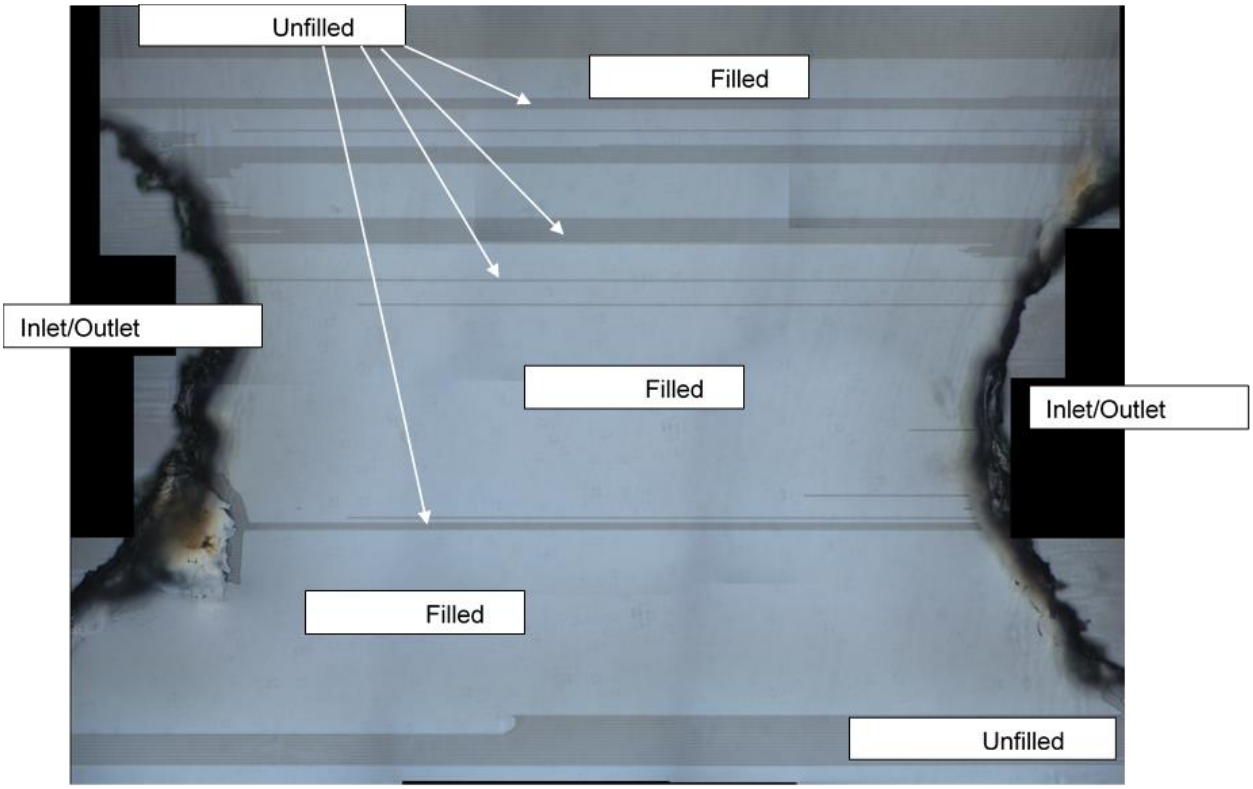

Figure A5.2 Optical brightfield stitched image of nanochannel with channel ports shown on either end. Light color are channels loaded with HKUST-1 precursor solution; dark channels are unloaded. 20X microscope images are stitched together using imageJ stitching tools. This allows for observation of the whole nanochannel region where crystallization can occur.

Calculating Maximum Theoretical Yield of Crystal for a Nanochannel

Reaction Scheme for HKUST-1 Formation (ACS sustainable chem, 2017, 5, 7887-7893)

$$3\ Cu(NO_3)_2 + 2\ BTC \rightarrow 1\ HKUST + 6\ HNO_3$$

HKUST-1 molecular weight: $604.87 \frac{g}{mol}$

HKUST-1 Density $0.35 \frac{g}{cm^3}$

Precursor solution (0.49 M BTC, 0.93 M $Cu(NO_3)_2$

BTC (linker) is the limiting reactant.

The maximum theoretical volume yield of HKUST-1 is calculated as follows:

$$0.49 \left[\frac{mol\ linker\ consumed}{L\ precursor}\right] * \frac{1}{2} \left[\frac{mol\ HKUST1\ formed}{mol\ linker\ consumed}\right] = 0.245 \left[\frac{mol\ HKUST1\ formed}{L\ precursor}\right]$$

$$0.245 \left[\frac{mol\ HKUST1\ formed}{L\ precursor}\right] * 604.87\ \left[\frac{g\ HKUST1}{mol\ HKUST1}\right] = 148.19 \left[\frac{g\ HKUST1}{L\ precursor}\right]$$

$$148.19 \left[\frac{g\ HKUST1}{L\ precursor}\right] * \frac{1}{10^{12}} \left[\frac{L}{picoliter}\right] = 1.48 * 10^{-10}\ \left[\frac{g\ HKUST1}{picoliter\ precursor}\right]$$

$$1.48 * 10^{-10}\ \left[\frac{g\ HKUST1}{picoliter\ precursor}\right] * \frac{1}{0.35} \left[\frac{cm^3 HKUST1}{g\ HKUST1}\right] = 4.22 * 10^{-10}\ \left[\frac{cm^3\ HKUST1}{picoliter\ precursor}\right]$$

$$0.422\ \frac{picoliters\ HKUST1}{picoliter\ precursor}$$

If the precursor solution completely fills the channel, then 100% channel loading efficiency is achieved. After crystallization occurs, if the reaction yield is 100%, then only 42% of the channels will be filled with crystal volume (0.42 pL HKUST-1 per pL of precursor). Therefore, complete channel loading will not achieve complete crystallization fill in the nano confined channels.

HKUST-1 Crystal Morphology

Representative SEM images of small, low aspect ratio crystals with hexagonal and square faceting.

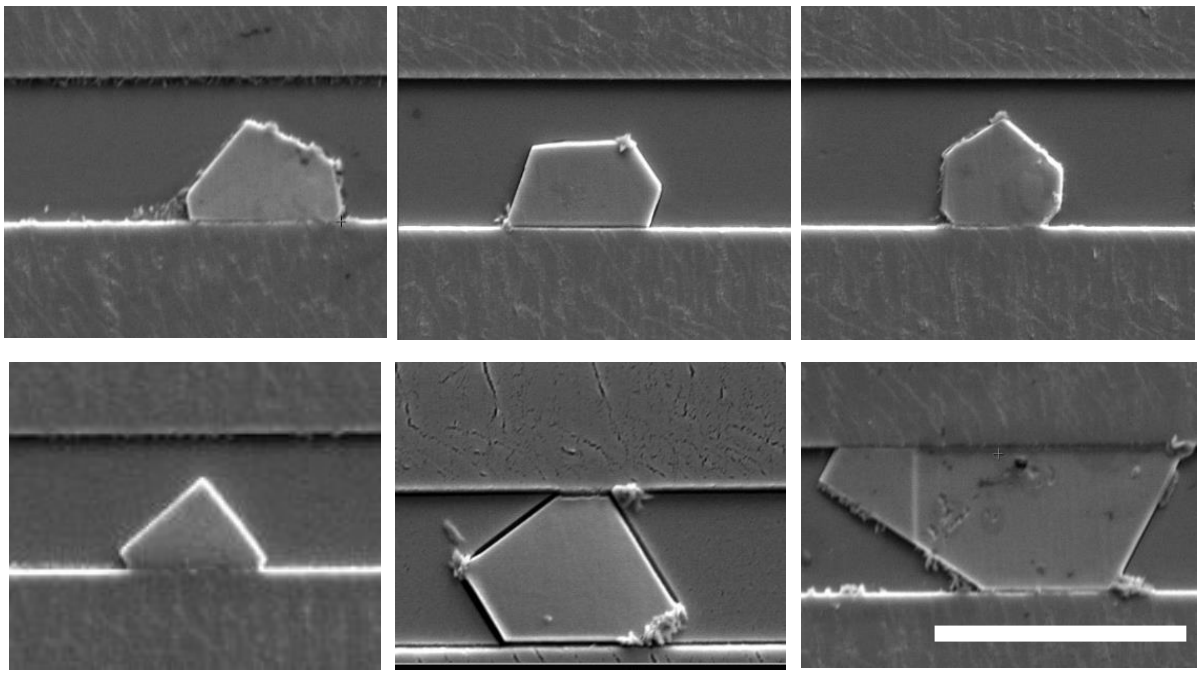

Figure A5.3 Hexagonal and square crystal morphology demonstrating crystal orientation relative to the channel bottom. Crystals do not appear to exhibit orientation effects with respet to the channel walls. Scale bar is 10 μm.

High Aspect Ratio Crystals in Nanochannels:

Aspect Ratio Calculation

The aspect ratio determined here and throughout the publication is defined as ratio of the largest dimension to the smallest dimension. With the crystal filling being space filling, the crystal depth is the same as the channel depth.

$$Aspect\ Ratio = \frac{Crystal\ Length}{Crystal\ Depth}$$

Images for aspect ratio calculations were captured using a brightfield view on the Zeiss Axio A1 Scope, as discussed in materials and methods.

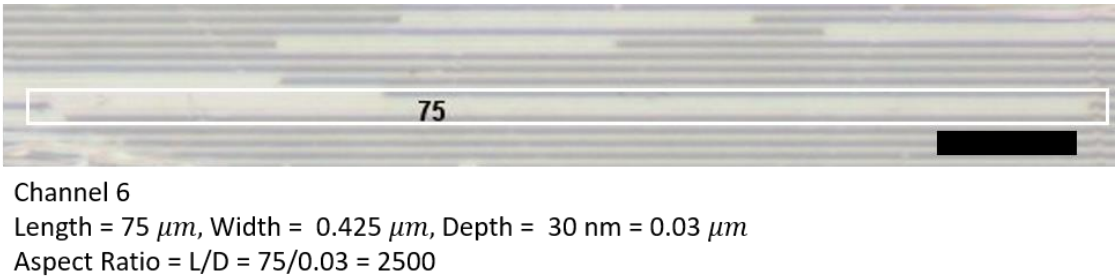

Figure A5.4 Example of a high aspect ratio crystal, formed in channel 6. The crystal length was measured to be 75 µm, and the depth 0.03 µm, L/D = 2500. Scale bar = 10 µm

Energy Dispersive X-ray Spectroscopy

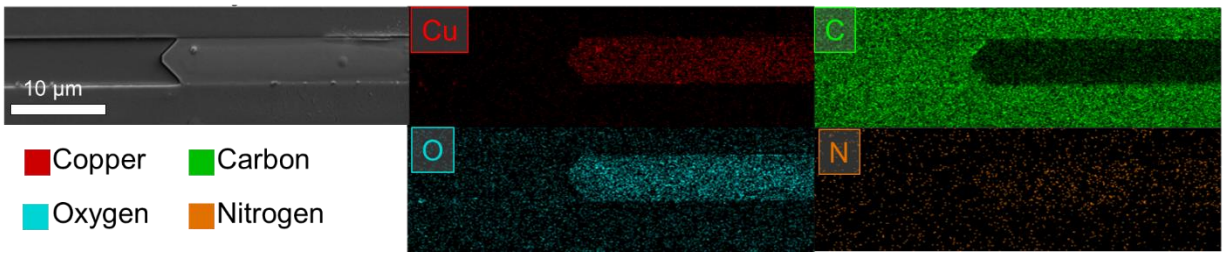

Figure A5.5 Scanning electron microscopy shows a faceted crystal in a nanofluidic channel. Energy dispersive X-ray spectroscopy of a HKUST-1 crystal shows the colocalization of copper and oxygen, both in the final MOF product. The reduced carbon signal in the crystal region is attributed to the strong carbon signal from the cyclic-olefin copolymer nanofluidic device (which is purely carbon).

Optical Images before and after methylene blue loading

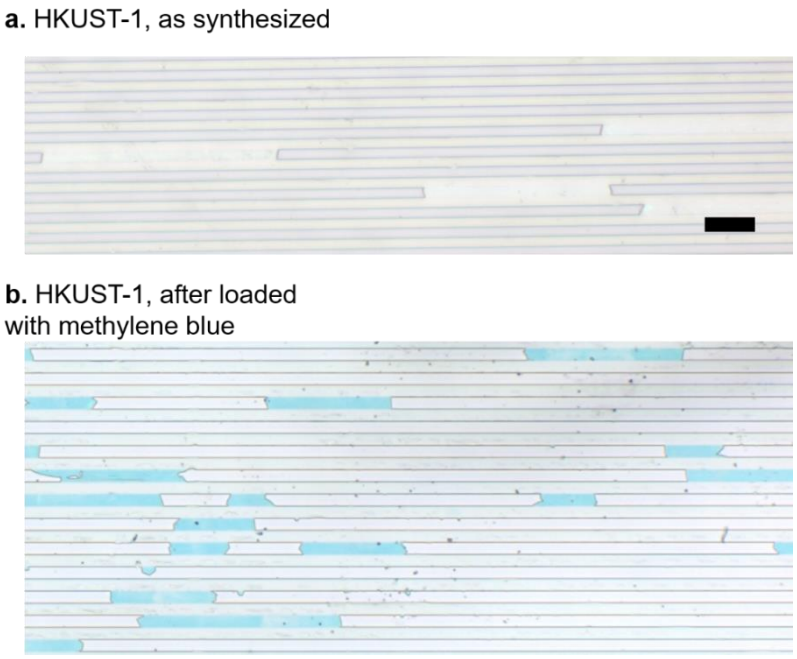

Figure A5.6 a) HKUST-1 crystals in nano-confined channels and b) crystals after being loaded with methylene blue. The crystals are visibly blue using brightfield imaging. Scale bar is 10 µm

Lysozyme loading and release from bulk NU-1000, with assessment of retained activity.

MOFs can be used for storage of proteins and biologics, in addition to small molecules as shown in this work. Lysozyme is a model protein that was used to demonstrate material compatibility between a MOF (NU-1000) and biologically active molecules like lysozyme. Lysozyme was dissolved in water at two concentrations (10 and 100 mg mL^{-1}). MOF was added to the lysozyme/water mixtures to allow for lysozyme to enter the MOF framework. After 24 hours, the MOF was isolated from the bulk solution using centrifugation.

Lysozyme release studies were carried out by resuspending the MOF in water and taking samples of the suspension fluid at designated timepoints. The amount of active lysozyme in free solution (released from the MOF) was characterized using a lysozyme activity assay (Sigma Aldrich, LY0100-1KT) using the manufacturer protocol. This assay provides the activity of lysozyme through measuring the degradation of Micrococcus lysodeikicus cells.

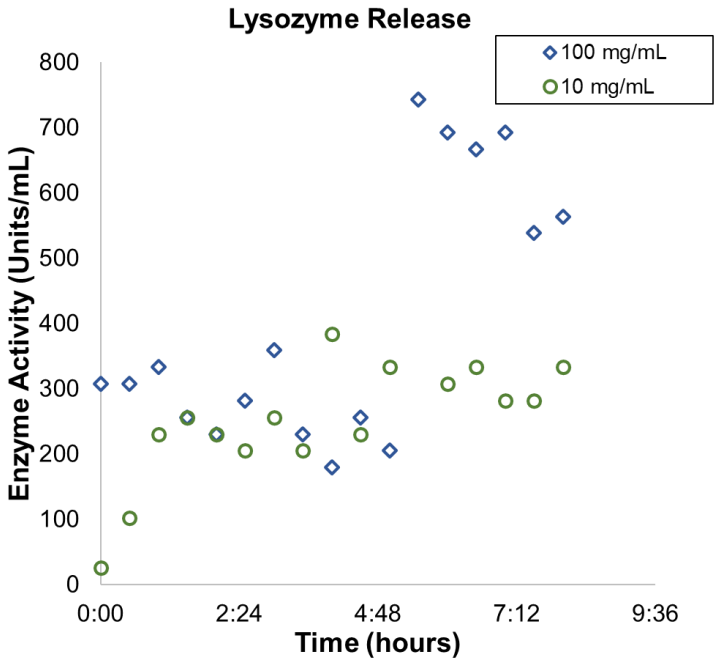

Figure A5. 7 Lysozyme released from NU-1000 after loading at two concentrations. The enzyme retains activity after storage within the MOF.

5.7 References

1. Breitkreutz, J. & Boos, J. Drug delivery and formulations. *Handb. Exp. Pharmacol.* **205**, 91–107 (2011).

2. Mishra, B., Patel, B. B. & Tiwari, S. Colloidal nanocarriers: a review on formulation technology, types and applications toward targeted drug delivery. *Nanomedicine Nanotechnology, Biol. Med.* **6**, 9–24 (2010).

3. Mukherjee, B., Santra, K., Pattnaik, G. & Ghosh, S. Preparation, characterization and in-vitro evaluation of sustained release protein-loaded nanoparticles based on biodegradable polymers. *Int. J. Nanomedicine* **3**, 487–496 (2008).

4. Kulkarni, T. A. *et al.* A year-long extended release nanoformulated cabotegravir prodrug. *Nat. Mater.* **19**, 910–920 (2020).

5. Yasmin, F., Chen, X. & Eames, B. F. Effect of process parameters on the initial burst release of protein-loaded alginate nanospheres. *J. Funct. Biomater.* **10**, (2019).

6. Zhuang, J. *et al.* Optimized metal-organic-framework nanospheres for drug delivery: Evaluation of small-molecule encapsulation. *ACS Nano* **8**, 2812–2819 (2014).

7. Furukawa, H., Cordova, K. E., O'Keeffe, M. & Yaghi, O. M. The chemistry and applications of metal-organic frameworks. *Science (80-.).* **341**, 1230444 (2013).

8. Tranchemontagne, D. J., Mendoza-Cortés, J. L., O'Keeffe, M. & Yaghi, O. M. Secondary building units, nets and bonding in the chemistry of metal-organic frameworks. *Chem. Soc. Rev.* **38**, 1257–1283 (2009).

9. Tian, T. *et al.* A sol-gel monolithic metal-organic framework with enhanced methane uptake. *Nat. Mater.* **17**, 174–179 (2018).

10. Li, J., Sculley, J. & Zhou, H. 2-33 Metal À Organic Frameworks for Separations. *Chem. Rev.* **112**, 869–932 (2012).

11. Stavila, V., Talin, A. A. & Allendorf, M. D. MOF-based electronic and opto-electronic devices. *Chem. Soc. Rev.* **43**, 5994–6010 (2014).

12. Lustig, W. P. *et al.* Metal-organic frameworks: Functional luminescent and photonic materials for sensing applications. *Chem. Soc. Rev.* **46**, 3242–3285 (2017).

13. Hu, P. *et al.* Preparation of highly-hydrophobic novel N-coordinated UiO-66(Zr) with dopamine via fast mechano-chemical method for (CHO-/Cl-)-VOCs competitive adsorption in humid environment. *Chem. Eng. J.* (2018) doi:10.1016/j.cej.2017.09.115.

14. Wu, M. X. & Yang, Y. W. Metal–Organic Framework (MOF)-Based Drug/Cargo Delivery and Cancer Therapy. *Adv. Mater.* **29**, 1606134 (2017).

15. Bag, P. P., Wang, D., Chen, Z. & Cao, R. Outstanding drug loading capacity by water stable microporous MOF: A potential drug carrier. *Chem. Commun.* **52**, 3669–3672 (2016).

16. Li, H. *et al.* Composite CD-MOF nanocrystals-containing microspheres for sustained drug delivery. *Nanoscale* **9**, 7454–7463 (2017).

17. Grall, R. *et al.* In vitro biocompatibility of mesoporous metal (III; Fe, Al, Cr) trimesate MOF nanocarriers. *J. Mater. Chem. B* **3**, 8279–8292 (2015).

18. Lin, W., Cui, Y., Yang, Y., Hu, Q. & Qian, G. A biocompatible metal-organic framework as a pH and temperature dual-responsive drug carrier. *Dalt. Trans.* **47**, 15882–15887 (2018).

19. Zybaylo, O. *et al.* A novel method to measure diffusion coefficients in porous metal-organic frameworks. *Phys. Chem. Chem. Phys.* **12**, 8093–8098 (2010).

20. Huelsenbeck, L. *et al.* Modulating and orienting an anisotropic zn-based metal organic framework for selective CH4/CO2 gas separation. *Crystals* (2019) doi:10.3390/cryst9010020.

21. Shiozawa, H. *et al.* Doping of metal-organic frameworks towards resistive sensing. *Sci. Rep.* **7**, 1–8 (2017).

22. Vikrant, K. *et al.* Potential Utility of Metal-Organic Framework-Based Platform for Sensing Pesticides. *ACS Appl. Mater. Interfaces* **10**, 8797–8817 (2018).

23. Haque, E. *et al.* Adsorptive removal of methyl orange from aqueous solution with metal-organic frameworks, porous chromium-benzenedicarboxylates. *J. Hazard. Mater.* **181**, 535–542 (2010).

24. Heinke, L., Gu, Z. & Wöll, C. The surface barrier phenomenon at the loading of metal-organic frameworks. *Nat. Commun.* **5**, 4562 (2014).

25. Sholl, D. S. & Lively, R. P. Defects in Metal-Organic Frameworks: Challenge or Opportunity? *J. Phys. Chem. Lett.* **6**, 3437–3444 (2015).

26. Li, C. *et al.* Engineered Transport in Microporous Materials and Membranes for Clean Energy Technologies. *Adv. Mater.* **30**, 1704953 (2018).

27. Zhang, S., Wang, Z., Ren, H., Zhang, F. & Jin, J. Nanoporous film-mediated growth of ultrathin and continuous metal-organic framework membranes for high-performance hydrogen separation. *J. Mater. Chem. A* **5**, 1962–1966 (2017).

28. Makiura, R. & Konovalov, O. Interfacial growth of large-area single-layer metal-organic framework nanosheets. *Scientific Reports* vol. 3 2506 (2013).

29. Brown, A. J. *et al.* Interfacial microfluidic processing of metal-organic framework hollow fiber membranes. *Science (80-.).* **345**, 72–75 (2014).

30. Ameloot, R. *et al.* Direct patterning of oriented metal-organic framework crystals via control over crystallization kinetics in clear precursor solutions. *Adv. Mater.* **22**, 2685–2688 (2010).

31. Arbulu, R. C., Jiang, Y. B., Peterson, E. J. & Qin, Y. Metal–Organic Framework (MOF)

Nanorods, Nanotubes, and Nanowires. *Angew. Chemie - Int. Ed.* **57**, 5813–5817 (2018).

32. Shen, Y. *et al.* Ultimate Control over Hydrogen Bond Formation and Reaction Rates for Scalable Synthesis of Highly Crystalline vdW MOF Nanosheets with Large Aspect Ratio. *Adv. Mater.* 1802497 (2018) doi:10.1002/adma.201802497.

33. Giri, G. *et al.* One-dimensional self-confinement promotes polymorph selection in large-area organic semiconductor thin films. *Nat. Commun.* **5**, 3573 (2014).

34. Guthrie, S. M., Smilgies, D. M. & Giri, G. Controlling Polymorphism in Pharmaceutical Compounds Using Solution Shearing. *Cryst. Growth Des.* **18**, 602–606 (2018).

35. Diao, Y. *et al.* Solution coating of large-area organic semiconductor thin films with aligned single-crystalline domains. *Nat. Mater.* **12**, 665–671 (2013).

36. Kumatani, A. *et al. Solution-processed, self-organized organic single crystal arrays with controlled crystal orientation*. *Scientific Reports* vol. 2 (2012).

37. Shete, M. *et al.* On the direct synthesis of Cu(BDC) MOF nanosheets and their performance in mixed matrix membranes. *J. Memb. Sci.* (2018) doi:10.1016/j.memsci.2017.12.002.

38. Zha, J. & Zhang, X. Room-Temperature Synthesis of Two-Dimensional Metal-Organic Frameworks with Controllable Size and Functionality for Enhanced CO2Sorption. *Cryst. Growth Des.* (2018) doi:10.1021/acs.cgd.8b00349.

39. Guthrie, S. *et al.* Crystallization of high aspect ratio HKUST-1 thin films in nanoconfined channels for selective small molecule uptake. *Nanoscale Adv.* **1**, 2946–2952 (2019).

40. Evans, R. *et al.* Quantitative interpretation of diffusion-ordered NMR spectra: Can we rationalize small molecule diffusion coefficients? *Angew. Chemie - Int. Ed.* **52**, 3199–3202 (2013).

41. Pound, G. M. & Mer, V. K. L. Kinetics of Crystalline Nucleus Formation in Supercooled Liquid Tin. *J. Am. Chem. Soc.* **74**, 2323–2332 (1952).

42. Mao, Y. *et al.* Room temperature synthesis of free-standing HKUST-1 membranes from copper hydroxide nanostrands for gas separation. *Chem. Commun.* **49**, 5666–5668 (2013).

43. Liu, Q., Yang, J.-M., Jin, L.-N. & Sun, W.-Y. Metal ion induced porous HKUST-1 nano/microcrystals with controllable morphology and size. *CrystEngComm* **18**, 4127–4132 (2016).

44. Biemmi, E., Scherb, C. & Bein, T. Oriented growth of the metal organic framework Cu3(BTC) 2(H2O)3·xH2O tunable with functionalized self-assembled monolayers. *J. Am. Chem. Soc.* (2007) doi:10.1021/ja0701208.

45. Shete, M. *et al.* On the direct synthesis of Cu(BDC) MOF nanosheets and their performance in mixed matrix membranes. *J. Memb. Sci.* **549**, 312–320 (2018).

46. Li, T., Kozlowski, M. T., Doud, E. A., Blakely, M. N. & Rosi, N. L. Stepwise Ligand Exchange for the Preparation of a Family of Mesoporous MOFs. *J. Am. Chem. Soc.* **135**, 11688–11691 (2013).

47. Tu, M. *et al.* Reversible Optical Writing and Data Storage in an Anthracene-Loaded Metal–Organic Framework. *Angew. Chemie Int. Ed.* **58**, 2423–2427 (2019).

Chapter 6. Development of a printable pharmaceutical gel and 3D printing for personalized dosing

6.1 Abstract

Additive manufacturing is an attractive technique that can make personalized drug design feasible. However, there are challenges associated with formulating the printable materials, as well as validating that the printing process itself can produce viable drug products. This chapter presents strides towards designing 3D printed polymer/drug composites, with controllable dosage through changing the size of the printed object. Multilayer drug tablets are formulated from a poly (vinyl alcohol)/glycine gel. The 3D printed tablets were characterized using infrared spectroscopy and X-ray diffraction, showing that the composite tablets preserve the chemical identity of the PVA and glycine. Further, the tablets are composed of only one crystal form (α glycine). Drug release timescale for multilayer tablets is assessed, identifying the opportunity to direct future work towards modulating drug release.

6.2 Introduction

Additive manufacturing (AM), commonly referred to as 3D printing, is the process of manufacturing an object by depositing material layer by layer based on a computer-aided designed (CAD) model.[1] Early applications of additive manufacturing, known as rapid prototyping (RP), utilized the process to quickly construct a model using CAD.[1,2] RP provided a way to test and evaluate a design from which a final product could be derived.[1,2] According to *Gibson et al*, RP terminology "does not effectively describe more recent applications of the technology" in which the printed model is of higher quality comparable to the final product.[1] Several industries are already taking advantage of AM as a means to directly manufacture goods. For example, Airbus, Boeing, NASA and Lockheed Martin have utilized additive manufacturing to fabricate parts for

This work will be submitted for publication:

Stephanie Guthrie, Elizabeth Tonneslan, Craig Doody, Gaurav Giri. Development of a printable pharmaceutical gel and 3D printing for personalized dosing (*in preparation*).

aircrafts.[3] Ford, which has experience with RP since the 1980's, is now attempting to make the transition to 3D printing car parts.[4]

The pharmaceutical industry is also exploring the potential of additive manufacturing, with significant interest in drug delivery.[5] Manufacturing of today's pharmaceutical products currently relies on large-scale batch processing.[6] Related to the scale of its production methods, pharmaceuticals are designed for the "average patient," discounting the differing treatment needs of individuals .[7,8] Prior research has demonstrated the utilization of 3D printing techniques as a viable means for developing customizable drug delivery systems.[5,9]

One advantage of AM is its potential to customize drug release profiles. Roberts et al. employed 3D printing to develop a "five-in-one dose combination polypill" with the intention of creating well-defined drug release profiles for specific active ingredients.[7] Designed with compartments to separate the active pharmaceutical ingredients (APIs), different drug release profiles were achieved by manipulating the material surrounding the compartments and excipients to control drug solubility.[7] A hydrophobic cellulose acetate shell divided the sustained released drugs pravastatin, atenolol, and Ramipril, which were mixed with a hydrophilic polymer matrix (HPMC).[7] A disintegrate was combined with aspirin and hydrochlorothiazide to achieve an immediate release profile.[7] Gaisford et al. took a different approach and used 3D printing to easily change tablet geometry and control the rate of drug release.[10] Five shapes were printed – cube, cylinder, sphere, pyramid, and torus – with constant surface area, volume, and mass.[10] Results indicated drug release kinetics were dependent on surface area to volume ratio, with the largest ratio corresponding to the fastest release time.[10]

In the pharmaceutical industry, significant resources are dedicated to validating processes and quality control.[11] While exploring AM for custom formulations, crystallization needs to remain a central product attribute that is considered and characterized. Various studies have discussed the impact of extrusion and temperature on polymer crystallization during 3D printing, however there is not an understanding of how crystallization of an API occurs alongside the polymer

binder.[12–14] In traditional tablet formulations, the API and polymer binder are combined using processes like milling, granulation and compaction.[15,16] When developing a new technology, such as 3D printing for pharmaceutical manufacturing, it is important to assess how the new processing conditions may affect the final product. 3D printing may change pharmaceutical performance, through changing on crystallization of the API or interaction of the API with the polymer matrix, impacting physiochemical properties.[17,18] It is therefore critical to understand how the polymer and API interact in a 3D printed drug composite.[19]

Even traditional formulation approaches present challenges associated with crystallization. Ritonavir, a HIV anti-viral medication, is a prime example of the importance of controlling drug crystallization and understanding the potential for different polymorphs to exist.[18,20] After two years on the market, Ritonavir was recalled due to a polymorphic change.[18,20] A problem was noticed when a majority of the finished product lots failed the dissolution test due to a change in the solubility of the drug.[18,20] During production, the desired polymorph (Form I) transformed into a "thermodynamically more stable and much less soluble crystalline form," known as Form II.[20] As a result, a majority of the drug substance was precipitating out, thereby reducing Ritonavir's bioavailability to less than 5%.[18] To quickly address this problem, scientists at Abbott Laboratories began investigating a means to accurately and reliably produce Form.[20]

To avoid problems like Ritonavir's, the FDA has strict guidelines and testing requirements to ensure the safety and efficacy of a product is preserved throughout the manufacturing process.[21] It is important that the drug formulation preserves the API, and stabilizes the desired polymorph, preventing phase transformation.[22] Often, this is accomplished by selecting a combination of inert polymers, binders and excipients that can be used to package the API in an easy to use form, such as a tablet.[19]

This work investigates additive manufacturing to produce different doses of an API by changing the number of 3D printed layers, while considering the importance of pharmaceutical solid state in the final formulation. A polymer/API gel composed of poly(vinyl alcohol) and glycine

was designed and optimized alongside printing parameters. Modifying the 3D printer bed to enhance heating capabilities allowed us to print up to 50 layers of gel sequentially. The interaction between PVA and glycine was characterized using IR spectroscopy, with slight shifts in peak location showing that the two materials minimally interact, preserving the chemical identity of the two species. X-ray diffraction shows that glycine crystallized in the PVA matrix as the α glycine polymorph. Finally, personalized dosing potential was demonstrated through dissolution studies of multilayer tablets, where each of the doses (ranging from 1 to 50 layers) dissolved within 10 minutes. This work demonstrates the ability to change API dose through 3D printing a polymer/API composite material.

6.3 Materials and Methods

Materials

Partially hydrolyzed polyvinyl alcohol (PVA) was purchased from as an extruded filament, suitable for 3D printing (Makerbot Inc., Brooklyn, NY). Glycine (>98.5% purity) was obtained from Thermo Fisher Scientific (Waltham, MA). Ultrapure water was used for all experiments.

Methods

Preparation of drug-loaded gel

A drug-loaded gel was prepared using PVA filament and glycine. 15 g of commercial PVA filament and 2 g of glycine were added to 100 mL of ultrapure water. The solution was covered to avoid evaporation of the water and positioned on an IKA RCT basic hot plate at 95°C and 300 rpm stirring speed until complete dissolution of the polymer and drug (approximately 2.5 hours). The solution was then uncovered and subjected to the same conditions required for dissolution (95°C and 300 rpm stirring speed) until the desired drug-loading percentage was achieved (~18 to 20 hours). The drug-loading percentage of the gel as shown in Equation 1.

$$drug\ loading\ \% = \frac{mass\ of\ glycine}{mass\ of\ solution} \qquad (Eqn. 1)$$

Conducting this process in a sealable container allowed for the evaporation of water to be interrupted and the solution to be stored without inducing any noticeable changes. The gel was loaded in to a BD 10 ml Luer-Lok Syringe with a Kimble 22 gauge blunt needle. The syringe was then inserted in to the Hyrel SDS-5 Extruder (Norcross, GA).

Tablet Design

Glycine-loaded PVA tablets were designed in a rectangular prism shape using SolidWorks 2016 and saved in STL format. The selected size for the tablet was X = 25 mm, Y = 25 mm with the Z dimension being controlled through the number of printed layers. The STL was converted to G-code using Hyrel's proprietary Repetrel software.

Printer settings and modifications

Because the 3D printer could not reach appropriate temperatures, modifications were made to the printer set-up. An All Flex (Northfield, MN) flexible heater was secured to the print bed and the temperature was controlled using a Staco Energy Products Co. Variac, Model 3PN1010B (Miamisburg, OH). The temperature was set to 100 °C to control the evaporation of water from the gel. Multiple layers of gel were printed sequentially.

A Hyrel Engine SR 3D Printer (Norcross, GA) was utilized to print glycine-loaded PVA tablets. Print settings that were found to produce the best tablets were a print speed of 0 mm s^{-1}, a travel speed of 10 mm s^{-1}, a layer height of 0.2 mm, and a rectilinear fill pattern with 100% infill. The print settings used to control the amount of material extruding form the syringe were set at a motor speed of 100 and material flow rate multiplier of 0.25.

Characterization

Fourier Transform Infrared spectroscopy (IR)

IR spectra were collected using a Perkin Elmer Frontier Infrared Spectrometer (Waltham, MA) with an attenuated total reflectance accessory. Spectra are the accumulation of four scans, with a collection wavelength of 4000 - 350 cm^{-1}. Peak positions were determined using Spectrum Software (Perkin Elmer, Waltham MA).

X-ray diffraction

Grazing incidence X-ray diffraction was carried out at the Cornell High Energy Synchrotron Source at the D1 beamline. The sample to detector distance was 176 mm, and X-ray wavelength was 0.1162 nm. A Pilatus 200K (Dectris) area detector with pixel size 172 x 172 µm was used to collect and record diffraction data. GIXSGUI was used to analyze data and produce 1-dimensional line scans.[23]

Dissolution

PVA/glycine tablets were dissolved in 100 mL ultrapure water at 37 °C with a stir bar at 100 RPM. 100 µL of the bulk solution was taken at designated time points. At the completion of dissolution experiments, samples were placed in a 96 well plate and absorbance spectra were measured on a BioTek Synergy 4 microplate reader (Thermo Fisher Scientific, Waltham, MA). The absorbance at 340 nm was used to determine the extent of dissolution. Glycine release was assumed to correlate directly to the amount of PVA released.

6.4 Results and Discussion

Designing a drug product formulation requires finding compatible materials, such as a polymer and active pharmaceutical ingredient (API), where the polymer is able to stabilize the API for storage and release the product when ingested. A personalized medicine drug product which can be fabricated using 3D printing begins with the development of a printable material. We explored several approaches to designing a printable material that includes a polymer binder and an API, shown in **Table 6.1**.

A drug loaded filament would utilize passive diffusion of the API into the filament, followed by traditional extrusion based printing from a heated nozzle head.[24,25] A printable gel or paste was selected instead of a drug loaded filament, because these approaches allow for a greater drug loading efficiency, with less material waste. A paste consists of a suspension of polymer and API that is not homogeneous. Compared to a paste, a gel is uniform in consistency and has preferable

viscosity to provide control over extrusion of the gel and formation a stable structure that holds a shape during drying.[26,27]

Table 6.1: Three polymer/API systems explored for development, including drug loaded filament, drug loaded paste and drug loaded gel.

Printing formulation	Pros	Cons
Drug loaded filament	• Easy to interface with traditional 3D printer nozzles	• Low drug loading efficiency
Polymer/drug paste	• High drug loading efficiency	• Texture not amenable to controlled extrusion • Requires printer modification to control drying • Heterogeneous material texture
Polymer/drug gel	• Desirable viscosity for printing • High drug loading efficiency	• Requires printer modification to control drying

An optimized glycine/PVA gel synthesis was designed, and is described in **Figure 6.1a**. Glycine, PVA and water were covered on a hot plate and heated to 95 °C. Heat input is required to enable dissolution of PVA, and create a homogeneous mixture. After the mixture is homogeneous, evaporation of excess water increases the concentration of PVA/glycine in the final formulation. For a drug delivery application, it is desirable to achieve a high load of API relative to binder, in order to minimize the size of the final printed product. Therefore, we varied the amount of glycine during gel synthesis. We found that it was possible to achieve a 4.2 wt% glycine formulation (**Figure 6.1b**) but that higher loading resulted in phase separation in the gel; the three-phase system is unstable, and oiling out occurs under a 10.4 wt% glycine formulation (**Figure 6.1c**). **Figure 6.1c** shows the separation of a liquid phase from the PVA gel.

The 4.2 wt% gel formulation was viscous enough to print layer-by-layer gel tablets. The Hyrel 3D printer has a heated bed (maximum temperature of 70 °C), to control drying through evaporation of water from the gel during printing. After printing one layer of gel at 40 °C, 45 minutes were required to dry the layer. Printing a second layer on top of the first at 40 °C required

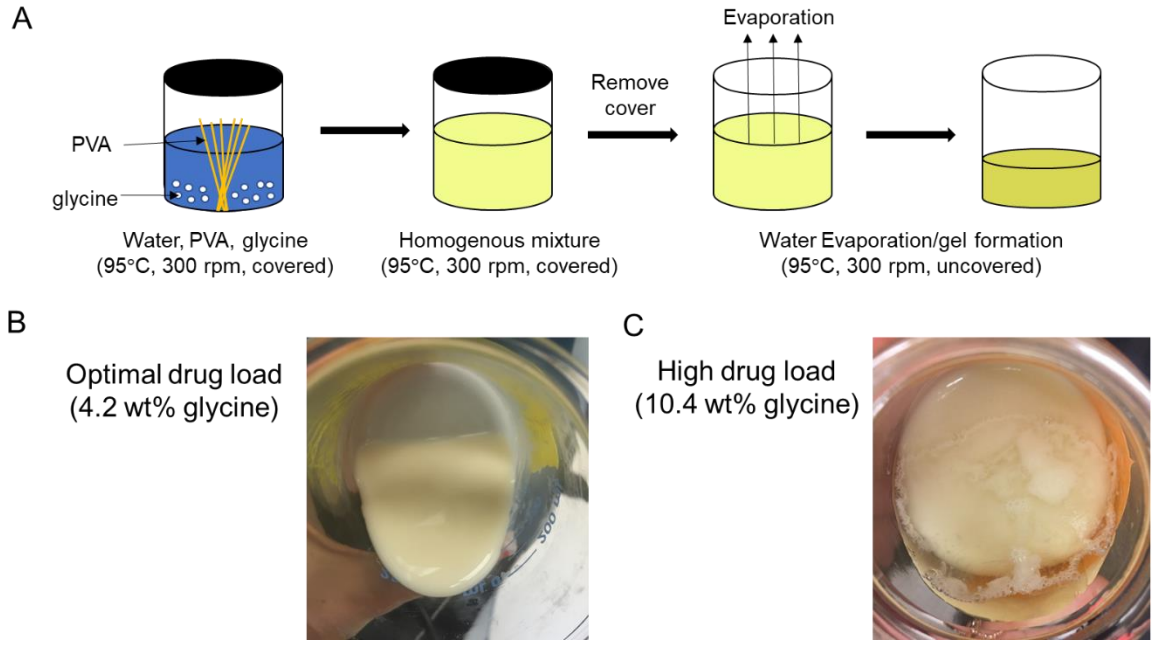

Figure 6.1 a) Schematic of process to create glycine/PVA gel for 3D printing. b) a 4.2 wt% glycine gel formulation is homogeneous while c) a 10.4 wt% glycine gel exhibits phase separation.

60 minutes to dry. To improve drying time, we increased the printing bed temperature to 70 °C, and found that drying time for the first and second layers was 15 minutes, an improvement but still not ideal for printing multilayer tablets efficiently. Therefore, we modified the printer hot bed with a heating element to allow us to use higher temperatures (discussed in materials and methods). Using a temperature of 100 °C effectively coupled the printing and drying processes, such that subsequent layers could be printed immediately after the previous layer.

The optimized gel was viscous, providing a means to control the amount of material deposited in each layer through changing printer conditions (e.g. flow rate multiplier and rate of extrusion) (**Figure 6.2a, b**). A rectilinear infill pattern (**Figure 6.2c**) was selected as opposed concentric infill, to produce a fully filled tablet. The tablets could be removed from the print bed as free standing and uniform object (**Figure 6.2d**). Further, after optimizing the print temperature, multiple layers were printed sequentially, achieving up to 50 layers (**Figure 6.2e**). This demonstrates the advantage of using additive manufacturing for personalized drug formulation

design – the approach allows for control over the total amount of drug by changing the size of the tablet or the number of layers printed.

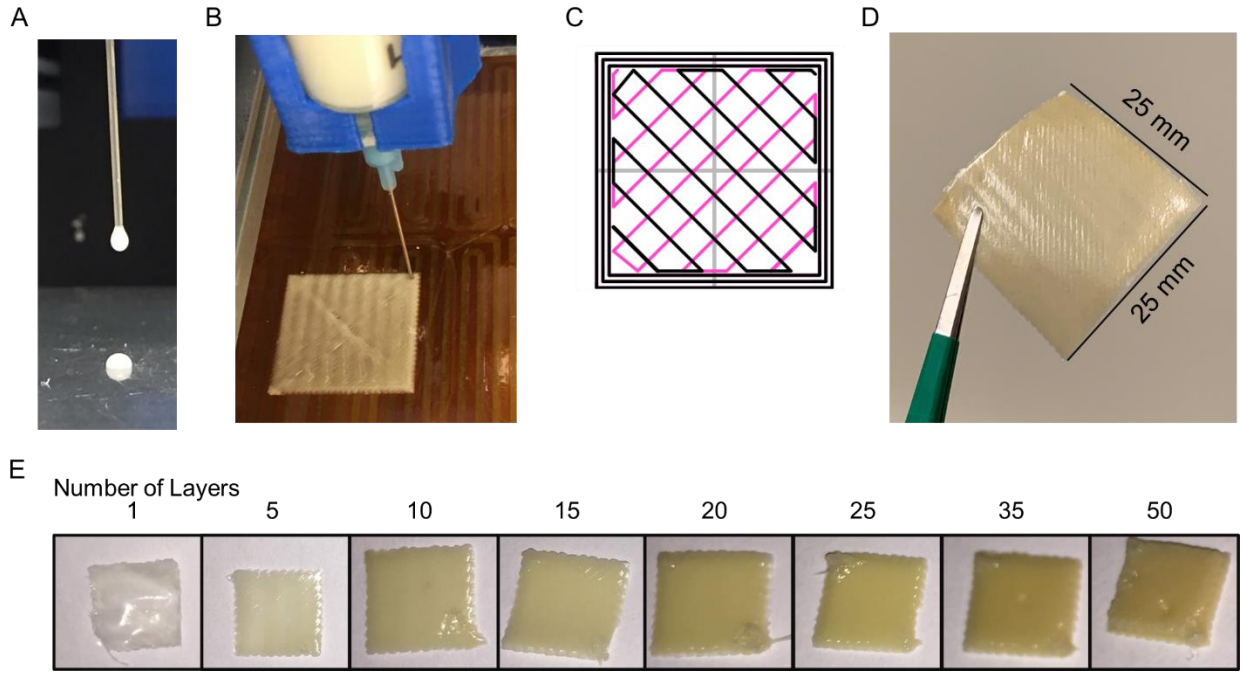

Figure 6.2 a) droplets of gel on a syringe top demonstrate the surface tension and viscosity of the gel. b) Printing a layered glycine/PVA tablet using c) a rectilinear print pattern. d) a free standing 5 layered tablet. e) Samples were printed with variable thickness by controlling the number of layers. 1-50 layers were printed using optimized printer settings.

During development of a drug delivery system, it is important to ensure that the API is unchanged in chemical form. IR was used to characterize the bonding and to ensure that new chemical entities were not produced during gel synthesis or printing (**Figure 6.3a**). Notable features and functional groups from the IR spectra are described in **Figure 6.3b**. Looking at the high wavenumber region of the IR spectra (4000 - 3000), Glycine exhibits an IR peak at 3154 cm^{-1}, attributed to N-H asymmetric stretching in the NH_3^+ group, matching the IR signature of α glycine.[28] This indicates that glycine is in the charged, zwitterionic form (**Figure 6.3c**). The raw PVA material (labeled “PVA filament”) has a broad peak centered at 3295 cm^{-1}, which can be attributed to O-H stretching, due to intermolecular and intramolecular hydrogen bonding of PVA.[29] In the composite material, the broad O-H stretching bond is centered at 3279 cm^{-1}. The NH_3^+ peak

A

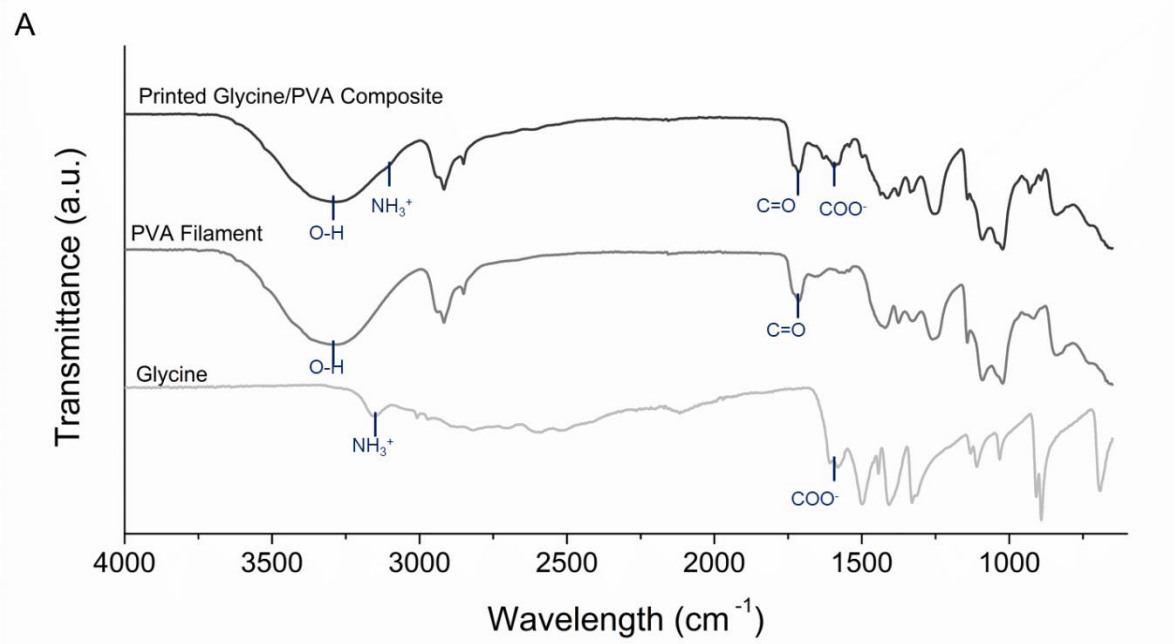

B

	Glycine	PVA filament	Glycine/PVA composite
NH_3^+ Asymmetric stretch	3154 cm^{-1}	-	3100 cm^{-1}
O-H Stretch	-	3295 cm^{-1}	3279 cm^{-1}
C=O Stretch	-	1713 cm^{-1}	1715 cm^{-1}
COO^- Asymmetric stretch	1580 cm^{-1}	-	1594 cm^{-1}

C

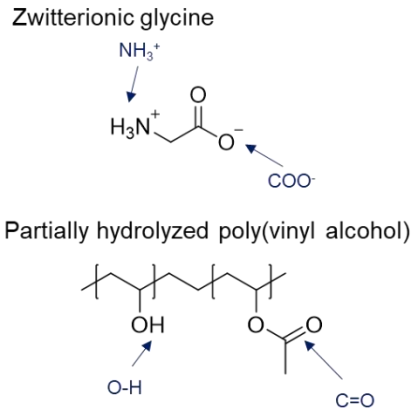

Figure 6.3 a) IR spectra of glycine and PVA filament, as received from vendors and IR of the 3D printed glycine/PVA composite tablet. b) Table with important features from IR spectra and c) chemical structures of glycine and poly vinyl alcohol with relevant functional groups identified.

is present as a shoulder on the O-H stretch, and is shifted to a lower wavenumber position compared the glycine control (**Figure 6.3b**). This indicates that some interactions may be occurring in the composite material, affecting the NH_3^+ and O-H bonding modes in the pure materials. However, no new features are observed after printing in high wavenumber regions of the IR spectra.

At lower wavenumbers, PVA exhibits a C=O bonding stretch at 1713 cm^{-1}. The presence of a C=O stretch is associated with acetate groups in PVA, indicating that PVA is only partially

hydrolyzed.[30] Glycine has a COO^- asymmetric stretch at 1580 cm^{-1}.[28] The printed glycine/PVA composites retain the IR features observed in the unprocessed materials and there is no evidence that suggests the formation of new functional groups.

X-ray diffraction was conducted to study crystallization of glycine in the 3D printed gel tablet (**Figure 6.4**). Glycine, as received, is found as the α polymorph. The PVA filament has a broad amorphous peak from 1-2 $Å^{-1}$ as well as sharper diffraction peaks, indicating that there is some degree of crystalline order alongside the amorphous polymer. This can be attributed to heterogeneity in the polymer structure, which inhibits total crystallinity.[31] We see the amorphous and crystalline PVA diffraction features present in the composite material as well as peaks associated with α glycine. IR and XRD together suggest that glycine is stabilized as a crystalline material in the PVA matrix. The two materials are minimally interacting, as only slight shifts in IR peaks were observed. This is desirable for drug storage, as the components of a drug formulation should not chemically change the API but instead be used to enhance drug stability and modify drug release characteristics.[22,32]

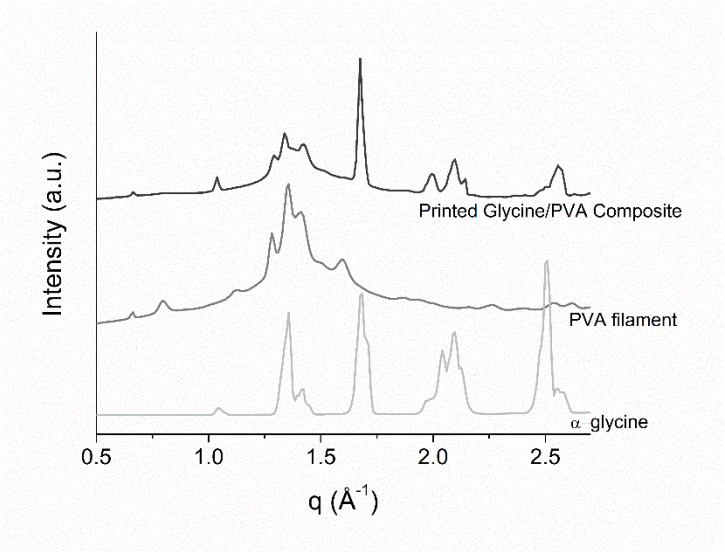

Figure 6.4 XRD spectra of glycine, PVA and 3D printed glycine/PVA tablet.

Finally, multilayer tablets were dissolved in water at 37 °C with moderate stirring (**Figure 6.5**). Each tablet achieved essentially full dissolution in 10 minutes. Tablets tended to fall apart into multiple pieces in the dissolution media and these smaller pieces continued to fully dissolve. This can contribute to error in the measurement method, as small pieces of undissolved material could be collected in the sample, dissolving later and increasing the measured extent of dissolution. This is likely the cause of peak at early times, as with the 50 layer sample where it appears that more material was dissolved at early times compared to the final time point. Future studies can incorporate a more sophisticated dissolution setup, such as a two-compartment

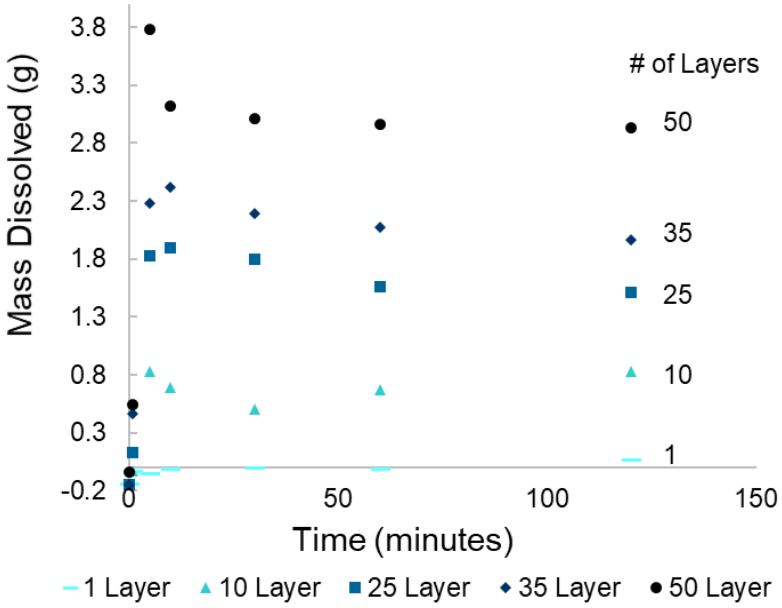

Figure 6.5 Multilayer (1,10, 25, 35, 50 layers) 3D printed tablets were dissolved to demonstrate drug release potential. Each material achieved dissolution within 10 minutes. Cumulative release quantified using absorbance (A_{340}).

filtered reservoir and continuous UV/vis monitoring of the bulk solution. Improved experimental design could also include pH control to simulate biological conditions.

Further, during dissolution studies, it was necessary to assume that glycine release is directly correlated to PVA release. UV-vis/absorbance is an imperfect technique for quantifying glycine concentration in solution, as there are not absorbance peaks for glycine in the UV-vis

range. Therefore, future studies of drug release should select an API system with more ease of characterization, such as phenytoin. The development of a phenytoin/PLGA system is discussed in Appendix 6 (**Figures A6.1, A6.2, A6.3**). Alternatively, an assay can be developed, such as the ninhydrin assay, for detection of glycine in bulk solution.[33,34] However, this assay would need to be validated for use in with PVA and glycine to ensure that PVA does not interfere with the mechanism of the assay's functionality.

6.5 Conclusion

This study provides proof of concept that 3D printing is a valid approach to creating composite polymer/API formulations, with printing multiple layers being an effective strategy to change dose. 3D printing was utilized to create a free-standing drug object, through using a novel gel formulation. The work presented here shows that there is not a significant change in release kinetics for the 3D printed glycine/PVA composites. Future work could focus on the design of novel polymers to modulate drug release timescales. For example, developing polymer networks with variable degrees of crosslinking could change the release kinetics, for tunable release alongside the tunable dosing demonstrated here.

While considering the utility of 3D printing for personalized medicine, quality control must remain central. Every FDA approved therapy must undergo validation to ensure that the drug product is safe for consumer use. Characterizing chemical changes and crystalline phases are important parts of this process, and could become nontrivial tasks as new technologies enable a growing suite of polymer/drug formulations. Therefore, understanding how 3D printing process could impact product quality is an emerging challenge related to 3D printed pharmaceutical products.

6.6 Chapter 6 Appendix

Solution Shearing Phenytoin/PLGA thin films: morphology, dissolution and binding

Thin films of phenytoin and phenytoin/PLGA were fabricated using solution shearing. A 10 mg phenytoin in 1 mL acetone solution was created for film deposition. Polymer was incorporated by adding poly(lactic-co-glycolic acid) (PLGA) to achieve 1 wt% PLGA. The films were deposited using 35 µL of solution, and a coating speed of 0.5 mm s^{-1} and temperature 50 °C. Films contained approximately 350 µg of phenytoin.

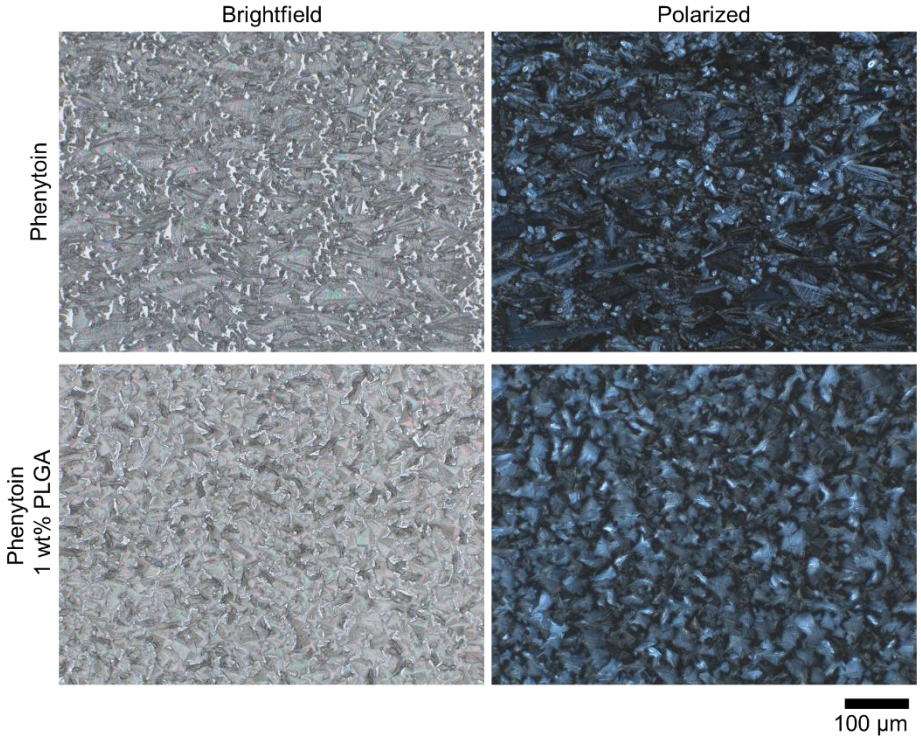

Figure A6.1 Brightfield and polarized optical microscopy images of phenytoin and phenytoin/PLGA films. Incorporation of PLGA affected the morphology of crystals in films.

Phenytoin release was assessed by submerging films in water, and determining the amount of phenytoin in bulk solution at designated time points. Two bulk solution volumes (10 mL and 100 mL) were assessed and10 µL of solution was required for sample measurement. Absorbance was measured (n=3 samples) at 220 nm, the lower limit of detection on the Nanodrop ND-1000 Spectrophotometer (Thermo Scientific, Waltham, MA). Absorbance was correlated to the amount of phenytoin released.

A large volume (100 mL) of water for dissolution studies decreased the time required to achieve full release, as it achieved a sink condition. The 10 mL volume required longer time for full phenytoin dissolution to occur (**Figure A6.2**)

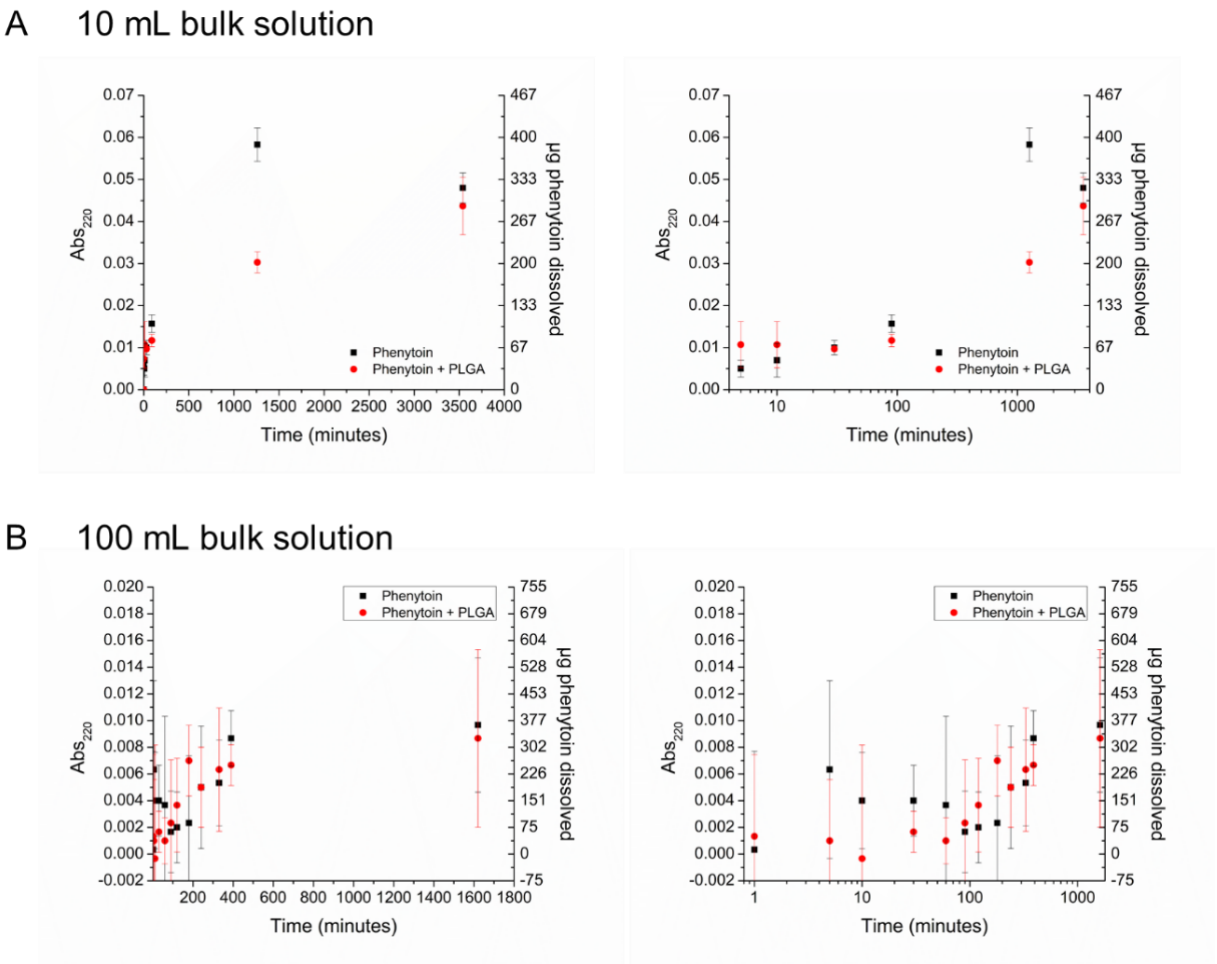

Figure A6. 2 Solution sheared phenytoin thin films dissolved in a) 10 mL of water and b) 100 mL of water.

When dissolution was carried out in 10 mL of water, there is less error associated with the measurement, because the range of fluid concentrations allows for more accurate absorbance readings. Absorbance readings in 100 mL bulk solution volumes were an order of magnitude lower, with greater error.

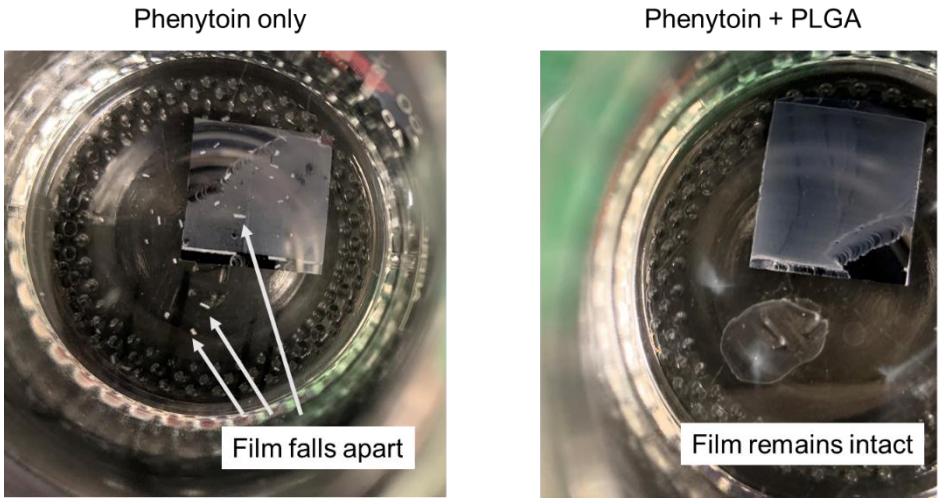

Figure A6. 3 Phenytoin films break apart during dissolution studies while phenytoin/PLGA composite films stick together, demonstrating the utility of polymer binders in formulations.

During dissolution, the films composed of only phenytoin had the tendency to fall apart, as flakes of phenytoin were visible in the bulk solution. Incorporation of PLGA in the thin film formulation created a film which remained intact.

Frequently in pharmaceutical formulations, polymers are used to bind the drug product and stabilize the drug product. Incorporating a polymer in the thin film facilitates binding, however it is important to recall that PLGA also affected the morphology of the crystals. Therefore, further characterization is required to ensure that the crystal polymorph is not changed between the two formulations.

6.7 References

1. Gibson, I., Rosen, D. & Stucker, B. *Additive manufacturing technologies: 3D printing, rapid prototyping, and direct digital manufacturing, second edition*. *Additive Manufacturing Technologies: 3D Printing, Rapid Prototyping, and Direct Digital Manufacturing, Second Edition* (2015). doi:10.1007/978-1-4939-2113-3.

2. Ahmad, A., Darmoul, S., Ameen, W., Abidi, M. H. & Al-Ahmari, A. M. Rapid prototyping for assembly training and validation. in *IFAC-PapersOnLine* (2015). doi:10.1016/j.ifacol.2015.06.116.

3. Gisario, A., Kazarian, M., Martina, F. & Mehrpouya, M. Metal additive manufacturing in the commercial aviation industry: A review. *J. Manuf. Syst.* **53**, 124–149 (2019).

4. Mearian, L. Inside Ford's 3D Printing Lab, where thousands of parts are made. *Computer World* (2014).

5. Jamróz, W., Szafraniec, J., Kurek, M. & Jachowicz, R. 3D Printing in Pharmaceutical and Medical Applications – Recent Achievements and Challenges. *Pharm. Res.* **35**, 176 (2018).

6. Içten, E., Giridhar, A., Nagy, Z. K. & Reklaitis, G. V. Drop-on-Demand System for Manufacturing of Melt-based Solid Oral Dosage: Effect of Critical Process Parameters on Product Quality. *AAPS PharmSciTech* (2015) doi:10.1208/s12249-015-0348-3.

7. Khaled, S. A., Burley, J. C., Alexander, M. R., Yang, J. & Roberts, C. J. 3D printing of five-in-one dose combination polypill with defined immediate and sustained release profiles. *J. Control. Release* **217**, 308–314 (2015).

8. Blau, G. E. *et al.* Validation of a novel approach for dose individualization in pharmacotherapy using gabapentin in a proof of principles study. *Pharmacotherapy* **33**, 727–735 (2013).

9. Park, B. J. *et al.* Pharmaceutical applications of 3D printing technology: current understanding and future perspectives. *J. Pharm. Investig.* **49**, (2019).

10. Goyanes, A., Robles Martinez, P., Buanz, A., Basit, A. W. & Gaisford, S. Effect of geometry on drug release from 3D printed tablets. *Int. J. Pharm.* **494**, 657–663 (2015).

11. U.S. Food and Drug Administration. Guidance for Industry: ICH Q8(R2) Pharmaceutical Development. *Work. Qual. by Des. Pharm.* (2009).

12. Yuan, Y. *et al.* Prediction of temperature and crystal growth evolution during 3D printing of polymeric materials via extrusion. *Mater. Des.* **196**, 109121 (2020).

13. Spoerk, M. *et al.* Polypropylene Filled With Glass Spheres in Extrusion-Based Additive Manufacturing: Effect of Filler Size and Printing Chamber Temperature. *Macromol. Mater. Eng.* **303**, 1800179 (2018).

14. Yang, C. *et al.* Influence of thermal processing conditions in 3D printing on the crystallinity and mechanical properties of PEEK material. *J. Mater. Process. Technol.* **248**, 1–7 (2017).

15. Loh, Z. H., Samanta, A. K. & Sia Heng, P. W. Overview of milling techniques for improving the solubility of poorly water-soluble drugs. *Asian J. Pharm. Sci.* **10**, 255–274 (2014).

16. Rogers, A. J., Hashemi, A. & Ierapetritou, M. G. Modeling of particulate processes for the continuous manufacture of solid-based pharmaceutical dosage forms. *Processes* **1**, 67–127 (2013).

17. Raza, K. Polymorphism: The Phenomenon Affecting the Performance of Drugs. *SOJ Pharm. Pharm. Sci.* **1**, 10 (2014).

18. Bauer, J. F. Polymorphism—A Critical Consideration in Pharmaceutical Development, Manufacturing, and Stability. *J. Valid. Technol.* **14**, 15–24 (2008).

19. Yang, F. *et al.* Probing the Molecular-Level Interactions in an Active Pharmaceutical Ingredient (API) - Polymer Dispersion and the Resulting Impact on Drug Product Formulation. *Pharm. Res.* **37**, (2020).

20. Chemburkar, S. R. *et al.* Dealing with the Impact of Ritonavir Polymorphs on the Late Stages of Bulk Drug Process Development. *Org. Process Res. Dev.* **4**, 413–417 (2000).

21. Center of Drug Evaluation and Research. Regulatory classification of pharmaceutical co-crystals, guidance for industry. *Food Drug Adm. U.S. Dep. Heal. Hum. Serv.* (2018).

22. Khandare, J. & Haag, R. Pharmaceutically used polymers: Principles, structures, and applications of pharmaceutical delivery systems. *Handbook of Experimental Pharmacology* (2010) doi:10.1007/978-3-642-00477-3_8.

23. Jiang, Z. GIXSGUI : a MATLAB toolbox for grazing-incidence X-ray scattering data visualization and reduction, and indexing of buried three-dimensional periodic nanostructured films. *J. Appl. Crystallogr.* **48**, 917–926 (2015).

24. Tagami, T., Kuwata, E., Sakai, N. & Ozeki, T. Drug incorporation into polymer filament using simple soaking method for tablet preparation using fused deposition modeling. *Biol. Pharm. Bull.* **42**, 1753–1760 (2019).

25. Tagami, T., Fukushige, K., Ogawa, E., Hayashi, N. & Ozeki, T. 3D printing factors important for the fabrication of polyvinylalcohol filament-based tablets. *Biol. Pharm. Bull.* **40**, 357–364 (2017).

26. Azad, M. A. *et al.* Polymers for extrusion-based 3D printing of pharmaceuticals: A holistic materials–process perspective. *Pharmaceutics* **12**, 124 (2020).

27. Jiang, Z. *et al.* Extrusion 3D Printing of Polymeric Materials with Advanced Properties. *Adv. Sci.* **7**, 2001379 (2020).

28. Pilling, S. *et al.* The influence of crystallinity degree on the glycine decomposition induced by 1 MeV proton bombardment in space analog conditions. *Astrobiology* **13**, 79–91 (2013).

29. Mansur, H. S., Sadahira, C. M., Souza, A. N. & Mansur, A. A. P. FTIR spectroscopy

characterization of poly (vinyl alcohol) hydrogel with different hydrolysis degree and chemically crosslinked with glutaraldehyde. *Mater. Sci. Eng. C* **28**, 539–548 (2008).

30. Duncan, T. T., Berrie, B. H. & Weiss, R. G. Soft, Peelable Organogels from Partially Hydrolyzed Poly(vinyl acetate) and Benzene-1,4-diboronic Acid: Applications to Clean Works of Art. *ACS Appl. Mater. Interfaces* **60**, 227–244 (2017).

31. Assender, H. E. & Windle, A. H. Crystallinity in poly(vinyl alcohol). 1. An X-ray diffraction study of atactic PVOH. *Polymer (Guildf).* **39**, 4295–4302 (1998).

32. Karki, S. *et al.* Thin films as an emerging platform for drug delivery. *Asian J. Pharm. Sci.* **11**, 559–574 (2016).

33. Friedman, M. Applications of the Ninhydrin Reaction for Analysis of Amino Acids, Peptides, and Proteins to Agricultural and Biomedical Sciences. *J. Agric. Food Chem.* **52**, 385–406 (2004).

34. Pal, K., Banthia, A. K. & Majumdar, D. K. Polyvinyl alcohol-glycine composite membranes: Preparation, characterization, drug release and cytocompatibility studies. *Biomed. Mater.* **1**, 49–55 (2006).

Chapter 7. Conclusions and Future work

During pharmaceutical development, crystallization plays several important roles. Crystallization is used to isolate and purify drug molecules after synthesis. Screening for polymorphs is carried out in early drug discovery and the form with optimal solubility and stability is selected for development. Crystal morphology (size and shape) must be controlled to provide the correct dissolution rate and to be incorporated with tablet formulations. Formulation design is an advancing field, with new technologies being explored to prolong drug release and increase drug loading.

7.1 Meniscus guided coating

In chapter 2, a meniscus guided coating (MGC) method, solution shearing, was used as a platform to screen for polymorphs of glycine and acetaminophen. The effect of film thickness on polymorph outcome was discussed; confinement conditions in the thinnest films are hypothesized to contribute to isolation of metastable polymorphs. Polymorphs are one type of crystal with relevance to pharmaceutical formulations. However, other solid forms are also interesting to evaluate using MGC. Future work could explore the utility of MGC for creating pharmaceutical cocrystals (two molecular compounds in an ordered lattice) and salts (two charged species in an ordered lattice).[1]

In chapter 3, in situ grazing incidence X-ray diffraction was used to observe MGC and glycine crystallization in real time during film formation. We gained spatial and temporal resolution of film heterogeneities due to either multiple crystal orientations in the thin film or the coexistence of multiple polymorphs. Full structural refinement in thin films can provide more conclusive information regarding the existence of different crystal structures in the films. Future work could also be directed towards increasing the in situ sample size and applying the technique to pharmaceutical molecules that are less sensitive to ambient moisture conditions.

In chapter 4, acetaminophen thin films were created using solution shearing with an expanded parameter space, including increased temperature and decreased coating speed. These conditions provided access to a unique flow coating regime. Three film morphologies are described, with particular focus on microcrystals as a desirable size and shape for pharmaceutical manufacturing. Future work can enable further exploration through modifying the MGC device to incorporate continuous solvent feed. Continuous solvent feed will allow for fabrication of larger films, producing more material to allow for additional characterizations.

7.2 New formulation approaches

In chapter 5, a nanofluidic device was used to crystallize a metal organic framework (MOF), HKUST-1. High aspect ratio MOF crystals were shown to have the capacity for the uptake of small molecules including methylene blue and anthracene. MOF biocompatibility and high storage capacity motivates their application for drug storage and delivery.[2] Ongoing and future work is directed towards developing new device geometry and utilizing fluid flow to load small molecules in the MOF. Kinetic studies can provide diffusion coefficients and describe small molecule transport within MOF materials. These studies are necessary to inform the design of MOF drug carriers.

In chapter 6, additive manufacturing through 3D printing is explored to design personalized medicine doses. Poly(vinyl alcohol) (PVA) and glycine were formulated as a gel for 3D printed; up to 50 gel layers were printed sequentially in this work. Drug release was assessed, with full dissolution of the tablets achieved on similar timescales regardless of the dose (number of layers). Opportunities for formulation innovation are clear with 3D printing and designing printable materials. New polymers can be synthesized and crosslinking can be incorporated as a method to control the timescale of drug release. Developing different polymer/molecule combinations can demonstrate the generalizable nature of 3D printing for pharmaceutical design. Finally, additional characterizations can be selected based on different interesting directions. The impact of processing on the formulation components can be probed using HPLC-MS[3] (to identify chemical

changes) or nuclear magnetic resonance (NMR) to assess polymer modifications throughout processing. Alternative, the material properties of synthesized tablets can be assessed using rheology or the stability of tablet formulations could be assessed.

This dissertation presents one of the earliest applications of MGC for pharmaceutical processing. Continuous and scalable technologies, such as MGC, can increase the efficiency and quality of pharmaceutical production. Formulations with improved functionality like prolonged release, enhanced loading, and personalized dosing have the potential to expand therapeutic options and improve patient care. With continued development of the technologies presented herein, there is an opportunity to transform pharmaceutical manufacturing, from crystallization to formulation.

7.3 References

1. Newman, A. W., Childs, S. L. & Cowans, B. A. Salt and Cocrystal Form Selection. in *Preclinical Development Handbook: ADME and Biopharmaceutical Properties* (2008). doi:10.1002/9780470249031.ch14.

2. Fernández-Paz, C. *et al.* Metal-Organic Framework Microsphere Formulation for Pulmonary Administration. *ACS Appl. Mater. Interfaces* **12**, 25676–25682 (2020).

3. Pitt, J. J. Principles and applications of liquid chromatography-mass spectrometry in clinical biochemistry. *Clin. Biochem. Rev.* **30**, 19–34 (2009).